School of Geography and Earth Sciences
McMaster University
Hamilton, Ontario, Canada

STABLE CARBON AND OXYGEN ISOTOPES IN BONE

-

TRACING DROUGHTS DURING THE MAYA ERA USING ARCHAEOLOGICAL DEER REMAINS

By
Antoine Repussard

Supervised by
Pr. Henry P. Schwarcz

A thesis submitted to the faculty of Mc Master University
In partial fulfilment of the degree of
Master of Science

August 2009

"True science teaches, above all, to doubt and to be ignorant"

Miguel de Unamuno

Del sentimiento trágico de la vida (1913)

Abstract

In this study, the potential of using white-tailed deer archaeological bones as an additional climatic proxy to track droughts in the Maya area at a very local scale is assessed.

The oxygen and carbon isotopic compositions ($\delta^{18}O$ and $\delta^{13}C$) on chronological series of numerous white-tailed deer bones, excavated from three Maya archaeological sites (Piedras Negras and Motul de San José, Petén region, Guatemala, and Lamanai, Orange Walk district, Belize) have been measured.

It is considered that the isotopic composition of deer bones reflects a multi-year average of relative humidity and local precipitation amounts ($\delta^{18}O$) as well as environmental conditions such as the type of food ingested by the animal ($\delta^{13}C$). The aim of the present work was principally to delineate the conceptual background needed to replace the obtained isotopic values in their context and understand their signification.

The results of geochemical analyses of deer bones are considered as reliable, in accordance with predicted values. However, the number of analyzed bones must be sufficient to accurately describe the variations of past climate variations. The major findings of this study are: (1) the use of Fourier Transform Infra Red spectroscopy is not a reliable way to detect diagenetically altered samples, (2) the climate during the apogee of the Classic Maya period was more variable than today, with more extremes pluri-annual wet and dry conditions, (3) no significantly dry climatic conditions occurred at the time the city of Piedras Negras started to decline and (4) dry conditions were probably responsible of the final abandonment of the site.

Acknowledgements

I would like to acknowledge first and foremost my supervisor, Pr. Henry P. Schwarcz for his generous support, his invaluable academic guidance and his constant willingness to encourage and trust me during those two years.

This work would not have been possible without the friendship and savoir-faire of Martin Knyf.

I would also like to thank Dr. Kitty Emery and Erin Thornton, for providing me with the material and for their support before and during the SAA conference, Steven Farber for his expertise in statistics, Gloria Lopez, my lab fellows, Duncan, Nurit and the "battalion" of undergraduate students working on Henry's innumerable projects, as well as Steven Kornic for training me on the FTIR spectrometer.

List of content

List of figures

List of tables

Introduction

With their magnificent architecture, their sophisticated knowledge in mathematics and astronomy, the complexity and subtlety of their cultural practices, the Maya civilization is considered as one of the most fascinating people of the New World. Since the rediscovery of monumental ruins, buried beneath the tangles of deep and dense jungle vegetation of Guatemala in the middle of the 19th century, hundreds (if not thousands) of archaeological campaigns have been conducted, that have permitted to progressively improve our knowledge about this pre-Columbian civilization. Those campaigns were greatly stimulated by one of the greatest anthropological mysteries of modern times: why and how, all of a sudden, several densely populated urban centres (some of them hosting probably more than 50,000 people; Becker, 1973) were abandoned and left to become ruins?

The territory of the Maya extended throughout the entire Yucatán peninsula in Central America, including the south-east of present Mexico (states of Tabasco, Chiapas, Campeche, Quintana Roo and Yucatán), Guatemala, Belize, and the western parts of Honduras and El Salvador. The Maya region actually comprises an important variety of landscapes, from the mountainous regions of the Sierra Madre de Chiapas Cordillera, to the semi-arid plains of northern Yucatán. These distinctive habitats, along with other archaeological criteria (duration of sites occupation, changes in ceramics style, zones of influence of the most important cities, etc.), lead to the demarcation of three major sub-areas among the Maya region: the Lowlands (itself divided into northern, central and southern Lowlands), the Highlands (northern and southern Highlands), and the Pacific coastal plain (see figure below). This distinction between the sub-regions emphasizes the fact that the Maya civilization has to be seen as a mosaic of co-existing city-states with proper characteristics and history, rather than a single uniform people.

Nevertheless, the history of Maya as a whole can be divided into three major periods with rough time boundaries: the Pre-Classic period (~2000 BC to ~ 200 AD), the Classic period (~200 AD to ~900 AD) and the Post-Classic period (~900 AD to ~ 1500 AD). During the transitions between each period, archaeologists have highlighted a distinct cessation of monumental inscriptions and large-scale architectural construction in many sites, along with a dramatic decrease in population (Lowe, 1985). It is during the Classic period that the Maya civilization reached its apogee, with a total population estimated to have topped at ~13 million at its peak, around 750 AD (Gill *et al.*, 2007).

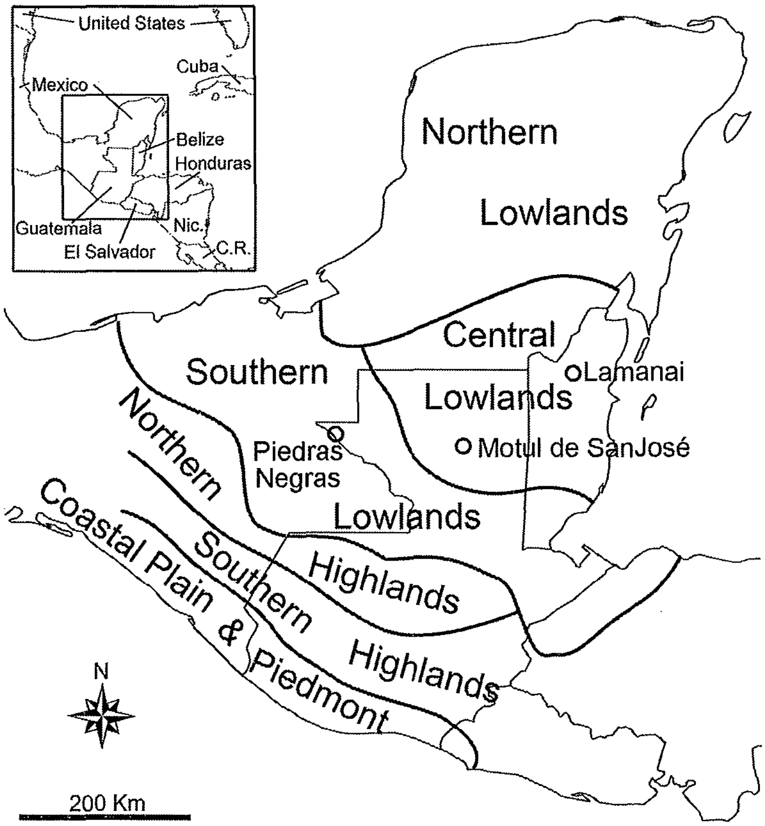

The sub-regions of the Maya territory in Central America (Nic.: Nicaragua; C.R.: Costa Rica).
The three sites studied in the present work are shown (Lamanai, Motul de San José and Piedras Negras)

The Terminal Classic, spreading roughly from 750 to 1050 AD marks the end of this flourishing period, and is referred by scholars as the "Maya collapse". Actually, the Maya collapse is also sometimes called "decline", "transition", "transformation", or "crumble" to emphasize on the complexity of the process: several archaeological studies have shown that the Maya collapse should be considered as a stage that various sites (or zones) faced at different times and at different rhythms (Aimers, 2007). For example, archaeological data highlights a fast and distinct population decline in certain areas (e.g. western Petén, Copán), whereas in other areas (e.g. north of Belize), the transition between the two periods (Terminal Classic and Post-

Classic) is more difficult to detect, because these sites have been continuously occupied, and no break in style of handcrafted goods (e.g. ceramics) is observed in the archaeological record. Actually the "Maya collapse" must be seen as a series of transformations, which began in the southern part of the Maya empire, as early as the end of the 8th century, and that was followed by a similar decline in the north through the 10th century (Haug *et al.*, 2003 ; Hodell *et al.*, 2007).

The material analyzed in this study has been excavated from three sites in the Central (Lamanai and Motul de San José) and Southern Lowlands (Piedras Negras; see figure above), each having distinct trajectory. The majority of the material is coming from the site of Piedras Negras, known to have been a powerful and influent regional centre in the Lowlands. The archaeological evidence show that the site has been constantly occupied from ~500 BC (Middle Pre-Classic) to ~AD 900 (Terminal Classic), a time at which the city has been completely abandoned (Muñoz, 2004). Motul de San José was first occupied during late Middle Pre-Classic (600-300 BC) and thrived during the Late Preclassic (300 BC – AD 300) and Early Classic (AD 300-600), reaching its apogee during the Late Classic (AD 600-830), and declined during the Terminal Classic (AD 830-950) and Postclassic (AD 950-1200; Foias, 2004). Unlike Piedras Negras, Motul de San José was a secondary city that flourished and perished in the shadow of its powerful neighbour city of Tikal (see also figure 2-1, Chapter 2). The site of Lamanai has a long, uninterrupted stratified sequence of occupation spanning the Middle Preclassic (900-300 BC) period through the Historic (17th Century) period. While many of the neighboring Mayan cities proceeded through a period of decay to final collapse, Lamanai survived this time of upheaval and continued to be a powerful regional centre, trading with sites in the northern part of the Yucatan Peninsula on into the Post-Classic Period (Pendergast, 1981).

Many assumptions were put forward to explain the complex pattern of abrupt decline of some of the classic Maya sites during the Terminal Classic. Mayanists have been debating for decades on the causes of such a radical upheaval: ecological causes, wars, disasters, famines or a combination of these factors were the reasons generally proposed to explain this decline (reviewed in Gill, 2000). However, an increasing amount of recent sedimentological studies involving geochemistry makes the concordance between dry episodes in the circum-Caribbean basin and the Terminal Classic Collapse less and less questionable (e.g. Haug *et al.*, 2003; Neff *et al.*, 2006; Hodell *et al.*, 2007; see Chapter 1)

The central role of climate change in the Maya collapse sheds a new light, helping to solve the mystery of its complex pattern. For example, it has been shown that the cities the most affected by a rapid population decline (in the southern and western Lowlands) were highly dependent on rainwater for human needs and agriculture, due to a limited access to fresh water (DeMonecal, 2001). Although the northern Lowlands are characterized by weaker precipitations (see Chapter 1), the numerous *cenotes* (natural wells) allowed an easier access to fresh, ground water (Haug *et al.*, 2003). The differences between land use and settlement histories can also have an impact on how dry climate can affect some populations more than others (Emery & Kennedy Thornton, 2008).

Lastly, like many other scholars (e.g.: Vargas-Pacheco, 2002), Aimers (2007) is convinced that droughts played a major factor in certain zones but he doubts that the direct effects of the dryness can be generalized to all the Maya Lowlands. According to these researchers, the dryness must be seen as a worsening factor that have hastened the fall of an empire that was already fading.

In this context, sedimentological studies are helpful to describe global climatic variations on the whole Maya territory at certain periods of time, but their low spatial resolution prevents a precise comprehension of drought impacts at the scale of a city, making difficult to replace archaeological findings in the perspective of climate change.

The aim of this study is thus to examine the potential of using white-tailed deer (*Odocoileus virginianus*) archaeological bones as an additional climatic proxy to track droughts in the Maya area. Those remains are especially promising for this purpose because: (1) they are relatively abundant in the Maya archaeological record, (2) they are associated with cultural remains, allowing them to be easily and accurately dated, and (3) most importantly, they are considered as very local recorder of past climatic and environmental conditions.

This thesis is divided into six chapters. The first chapter summarizes the characteristics of current and past Central American climate. In Chapter 2, the material is described, and a summary of bone structure, mechanisms of formation and mineralogical aspects is then presented. Chapter 3 details extensively the conceptual framework of deer bone isotopic analyses as a climatic proxy, and more specifically as an aridity indicator. Chapter 4 presents the methods used to analyze deer bone oxygen and carbon isotopic compositions, and those used to quantify the *post-mortem* chemical alterations they could have been subjected to. In Chapter 5, the results are presented and then finally discussed in Chapter 6.

References

Aimers J.J. (2007) - What Maya collapse ? Terminal Classic variation in the Maya Lowlands. *Journal of Archaeological Research* 15,(4): 329-377.

Becker M.J. (1973) - Archaeological evidence for occupational specialization among Classic Maya at Tikal, Guatemala. *American Antiquity* 38:396-406.

DeMonecal P.B. (2001) - Cultural responses to climate change during the late Holocene. *Science* 292, 667-673.

Emery K.F. & E. Kennedy Thornton (2008) - A regional perspective on biotic change during the Classic Maya occupation using zooarchaeological isotopic chemistry. *Quaternary International* 191, 131, 143.

Foias A.E. (2004) – Politics and Economics: Motul de San José, Petén. *Foundation for the Advancement of Mesoamerican Studies, Inc.* Accessed online <www.famsi.org>, June 2008.

Gill R.B. (2000) – The Great Maya droughts, Water, Life, and Death. University of New Mexico Press. Albuquerque.

Gill R.B., P.A. Mayewski, J. Nyberg, G.H. Haug, L.C. Peterson (2007) – Drought and the Maya Collapse. *Ancient Mesoamerica* 18, 283–302.

Haug G.H., D. Günther, L.C. Peterson, D.M. Sigman, K.A. Hughen, B. Aeschliman (2003) - Climate and the collapse of Maya civilization. *Science* 299, 1731-1735.

Hodell D.A., M. Brenner, J.H. Curtis (2007) - Climate and cultural history of the Northeastern Yucatan Peninsula, Quintana Roo, Mexico. *Climatic Change* 83, 215-240.

Lowe J.W.G. (1985) - The Dynamics of Apocalypse: A Systems Simulation of the Classic Maya Collapse. University of New Mexico Press, Albuquerque.

Muñoz A.R. (2004) – The Ceramic Sequence of Piedras Negras, Guatemala: type and varieties. *Foundation for the Advancement of Mesoamerican Studies, Inc.* Accessed online <www.famsi.org>, June 2008.

Neff H., D.M. Pearsall, J.G. Jones, B. Arroyo De Pieters, D.E. Freidel (2006) - Climate change and population history in the Pacific Lowlands of Southern Mesoamerica. *Quaternary Research* 65, 390-400.

Pendergast D.M. (1981) - Lamanai, Belize: Summary of Excavation Results, 1974-1980. *Journal of Field Archaeology* 8, 29-53.

Vargas-Pacheco E. (2002) - El impacto del cambio climático en la región del río candelaria, Campechen, México. *Ancient Mesoamerica* 13, 317-326.

Chapter 1 - Climatological framework

The central theme of this study is related to the reconstruction of past climate, thus this chapter summarizes the characteristics of current and past Central American climate. The general atmospheric circulation patterns are first briefly presented, followed by a focus on climatic features of Central America, and the drought definition is then presented. The final part recapitulates the occurrences of droughts in the historical record, as well as recent palaeoclimatic reconstructions in the maya area.

1.1) General patterns of atmospheric circulation

For a better understanding of the complex climatic processes taking place in Central America, a brief review of Earth's general patterns of atmospheric circulation is presented.

1.1.1) Latitudinal division of Earth's climate

On a first approximation, Earth's climate system can be divided, in each hemisphere, into three thermodynamically-driven convection cells, each of them covering roughly 30° of latitude (figure 1-1).

(1) *The Hadley Cell.* At the equator, where average solar radiation is greatest, air is heated, rises and diverges aloft through the troposphere. At the boundary between the troposphere and stratosphere (the tropopause, at an altitude of ~15 Km at the equator, lower at higher latitudes), the warm air cannot rise further, and flows poleward in both hemispheres. At a latitude of around 30°, the air has cooled sufficiently to begin sinking. This colder air forms zones of high pressure at the surface known as Subtropical Highs. As the cooled air reaches the surface, it spreads out such that the flow returns to the equatorial zone.

(2) *The Ferrel Cell.* Between 30° and 60° latitudes, the Ferrel Cell experiences a reversed flow pattern. Warm, moist air around 60° latitude rises and draws in the cooler 30° latitude air to

replace it. The warm air reaching altitude moves towards the equator, cooling as it goes, and then sinks where it encounters air masses from the Hadley Cell. There, air masses from both cells move downward but split (diverge) at the surface, maintaining each cell's circulation.

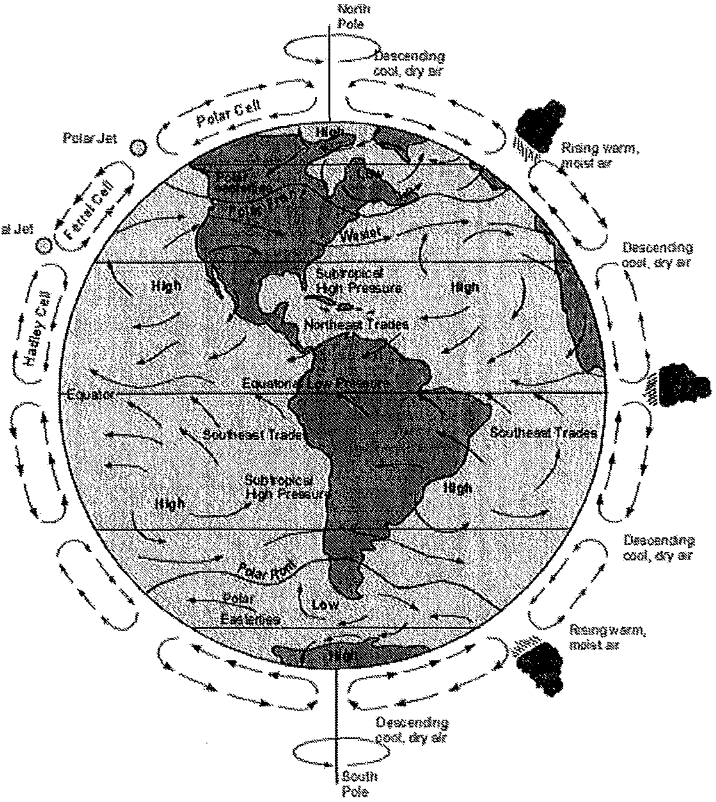

Figure 1-1. Schematic representation of the general patterns of atmospheric circulation on Earth, showing the three main convection cells, the zones of high and low pressure and general wind patterns at the surface, as well as zones of high and low precipitation and the location of the jet streams. From Murck *et al.* (1997).

(3) *The Polar Cell.* A similar cell-like fashion is observed between 60° and the poles. The 60° latitude zone is known as the Subpolar Low, since the converging surface air from both cells is warm and hence expanded to be in the low pressure state. At this polar front, air moves northward at altitude and cools progressively. It sinks around the poles, forming a Surface High of much colder air, flowing back near the surface to the 60° zone.

1.1.2) Surface movements of air masses

The convergence (convection) of air masses between northern and southern Hadley Cells at the equator creates a band of low pressure, known as the Inter-Tropical Convergence Zone (ITCZ). In the ITCZ, the ascending air cools, and the water vapour it carries condenses, forming clouds and thus very active thunderstorms. The ITCZ, also known as the meteorological equator, is then the area of constant tropical rainfall.

At higher latitudes (~30°), the descending air from Hadley and Ferrel Cells (at the Subtropical Highs) is very dry, having lost its moisture on the way up. It is precisely on the areas of Earth under the descending branches of Hadley Cells that most of the deserts are found (e.g.: Mojave, Sahara, Arabia, Atacama, and Australian Great Sandy Desert).

Surface winds are generated between the Subtropical highs and the ITCZ as air moves from high surface pressure toward low surface pressure. Because of Coriolis effect, due to Earth's rotation, these descending zones of high pressure veer in a clockwise direction in the northern hemisphere around the Subtropical Highs, giving rise to winds (known as Trade Winds or Tropical Easterlies), blowing from the northeast back towards the equator.

As Ferrel Cell surface air flows poleward, the deflection is counter-clockwise, so that air masses at latitudes between 30° and 60° are deflected to the East (northern hemisphere) and West (southern hemisphere). These winds are known as the Westerlies and Easterlies, respectively. Surface air of Polar Cells, as in the case of Hadley Cells, is deflected clockwise, creating Polar Easterlies at highest latitudes.

Lastly, at high altitudes in the atmosphere, just below the tropopause, narrow bands of high velocity winds (Jet Streams) flowing from west to east meander. The subtropical jet occurs above the descending air between the Ferrel Cells and the Hadley Cells. The polar jet occurs above the rising air between the Polar Cells and the Ferrel Cells.

1.2) Features of present climate in Central America

The geographical position of the Maya region in Central America, at the interface of several wind systems, between two oceans, in addition to its particular topography (figure 1-2), implies a very distinctive nature of its climate (Hunt & Elliot, 2005). Actually the Maya territory encompassed several varied climatic zones and landscapes, from the Guatemalan wet and dense tropical forest of Petén, to the Mexican semi-arid plains of northern Yucatán (Aimers, 2007). Those aspects are addressed in this part.

1.2.1) A marked wet/dry seasonality

The annual cycle in the climate of the Northern Hemisphere tropical Americas is characterized by minor fluctuations in surface temperature, but a well-defined rainy period exists from May through October (Hastenrath, 1976). Central American wet/dry seasonality is mainly determined by the position and strength of the Bermuda-Azores cell of the Subtropical High (Folan *et al.*, 1983) and by the annual migration of the ITCZ (Giannini *et al.*, 2000).

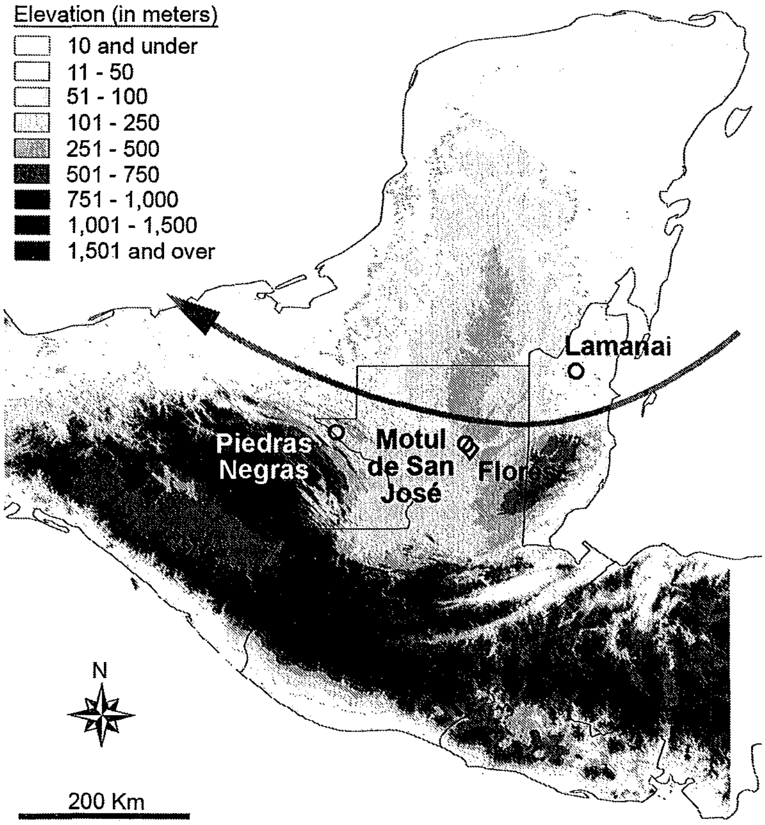

Figure 1-2. Topographical map of the Maya region, showing the southern cordillera of the Sierra Madre de Chiapas (corresponding to the Maya Highlands), the relatively flat Lowlands in the northern part of the peninsula and the low-altitude Maya Mountains of southern Belize. The location of the studied sites mentioned later in the text, as well as the direction of the prevailing easterly winds are shown. After Witschey & Brown (2009).

During winter (between January and March), the cross-equatorial Sea Surface Temperature (SST) gradient in the Atlantic is reduced, the tropical North Atlantic being cooler than the South Atlantic, resulting in increased surface pressure over the North Atlantic and a southward shift of the ITCZ, leading to drier conditions (figure 1-3; Black *et al.*, 1999). During these months, the high-pressure ridge of the Bermuda-Azores cell directly crosses the peninsula, precluding rain, since the dry subsiding air of the Subtropical High is targeted directly onto the zone (Dahlin, 2002). However, temperature and precipitation in the Yucatán region during winter can be modulated by outbreaks of polar air masses, sweeping southwards with strong northerly winds (e.g.: Schultz *et al.*, 1997). These air masses of polar origin with high winds across the Yucatán peninsula, as well as over the mountains of the Sierra Madre de Chiapas (figure 1-2), are a characteristic feature of the winter climate in the zone (Mendoza *et al.*, 2007).

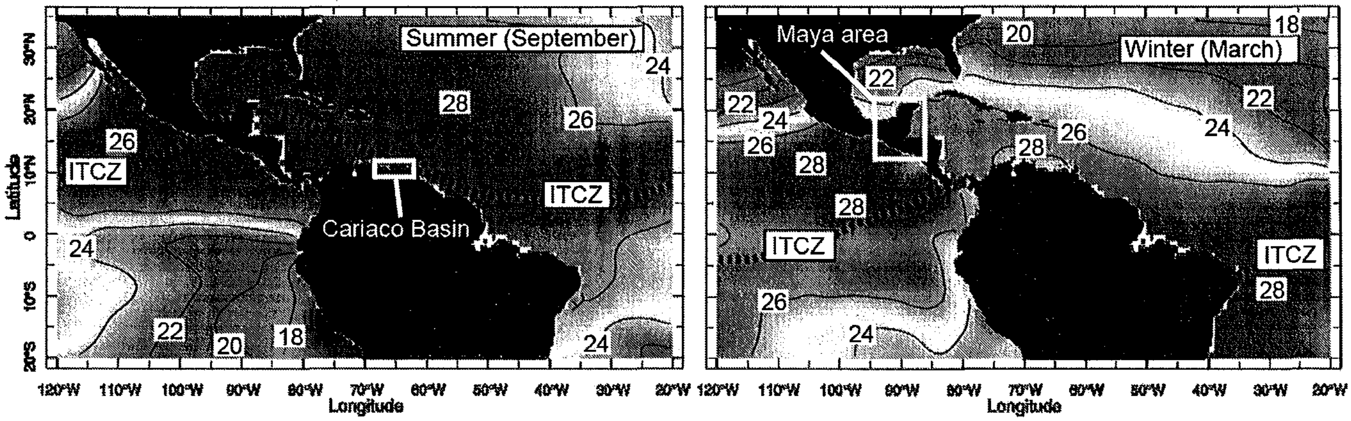

Figure 1-3. Seasonal variations in the mean position of the ITCZ over Mesoamerica and northern South America, illustrated for typical summer (left) and winter (right) conditions. These variations control the pattern and timing of regional rainfall. Numbers and grey scale reflect sea surface temperatures in degrees Celsius. Locations of the Cariaco Basin and the Maya area are indicated. Both regions are similarly affected by seasonal and longer term changes in the position of the ITCZ. From Haug *et al.* (2003).

The major part of precipitation usually falls in summer (from June to October), when the ITCZ is at its northernmost position (*i.e.* laying on Maya region; figure 1-3). The Maya region is then fed with moisture picked up by the prevailing easterly trade winds (northern branches of the low level Caribbean jet) over the Caribbean Sea (figure 1-2; Hodell *et al.*, 2007). Due to the direction of trade winds, as well as the presence of the Sierra Madre de Chiapas cordillera in the south, air masses carrying moisture from the eastern Pacific are blocked (figure 1-2). Rain falls as clouds blow and advect progressively along a northwesterly path (Williams, 1976). Those clouds rise higher over the Maya Mountains in the southeast and slightly less beyond the reach of the mountains in the central peninsula, and they maintain much lower levels of humidity over the extremely low and flat Northern Plains (Dahlin, 2002). Annual rainfall amounts range from close to 4,000 mm in the mountains of southern Belize, to about 2,000 mm at Flores in central Péten (Guatemala), to less than 500 mm at the north-western tip of the peninsula (figure 1-4; Dahlin, 2002; Hodell *et al.*, 2007).

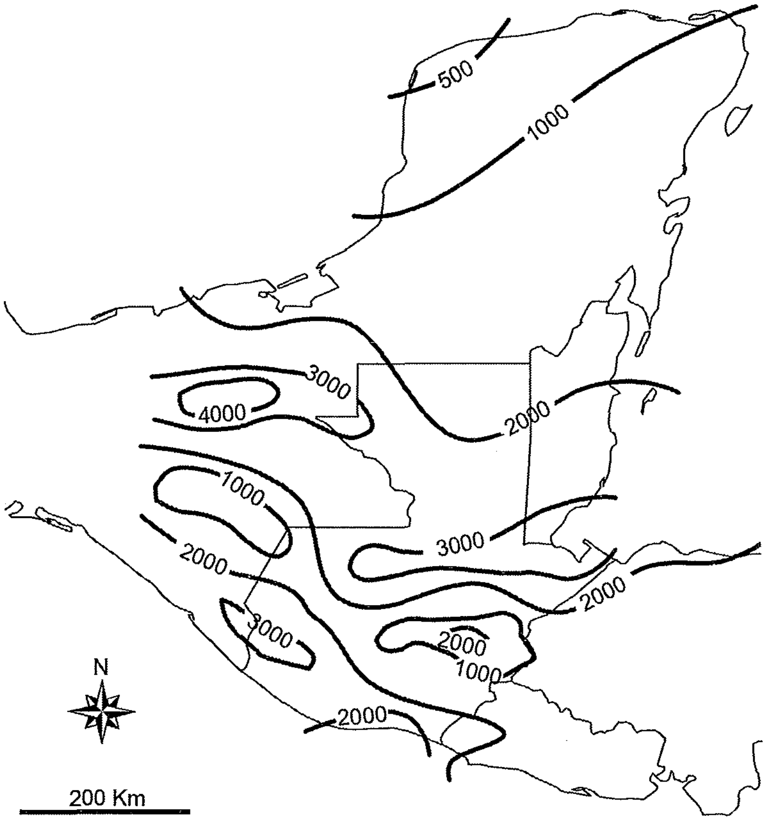

Figure 1-4. Isohyets on the Maya region, presenting the distribution of annual average precipitation (in $mm.yr^{-1}$). After CNA (2009) and INSIVUMEH (2009) databases.

1.2.2) The midsummer drought

As noticed by Hastenrath (1967), precipitation over Central America and the Caribbean basin occurring during the rainy season is characterized by a bimodal distribution with maxima in June and September–October, separated by a relative minimum during July–August, being drier and less cloudy (Magaña *et al.*, 1999). This relative decrease in rain amount during the rainy season is known as midsummer drought (MSD), and can result in a reduction up to 40% of rainfall from one month to the next one during the rainy season (Curtis & Gamble, 2008). The MSD does not correspond to an actual drought period but rather to a decrease in the amount of rain.

The origin of the MSD seems to be the result of local air-sea interactions, building up convective clouds at the beginning of the rainy season (June), leading to a slight cooling of the eastern Pacific due to the shadowing effect of clouds (Curtis & Gamble, 2008). The disturbance of SST produces anomalous anticyclonic circulation and divergence of low level winds (Magaña *et al.*, 1999), causing the precipitation decrease.

The MSD extends from northeastern Mexico to Central America, but is more clearly defined over southwestern Mexico, Central America, and the eastern Pacific warm pool, where the ITCZ is active during summer. Over northwestern Mexico, there is no indication of an MSD, showing that this phenomenon is dynamically independent of the Mexican monsoon (figure 1-5).

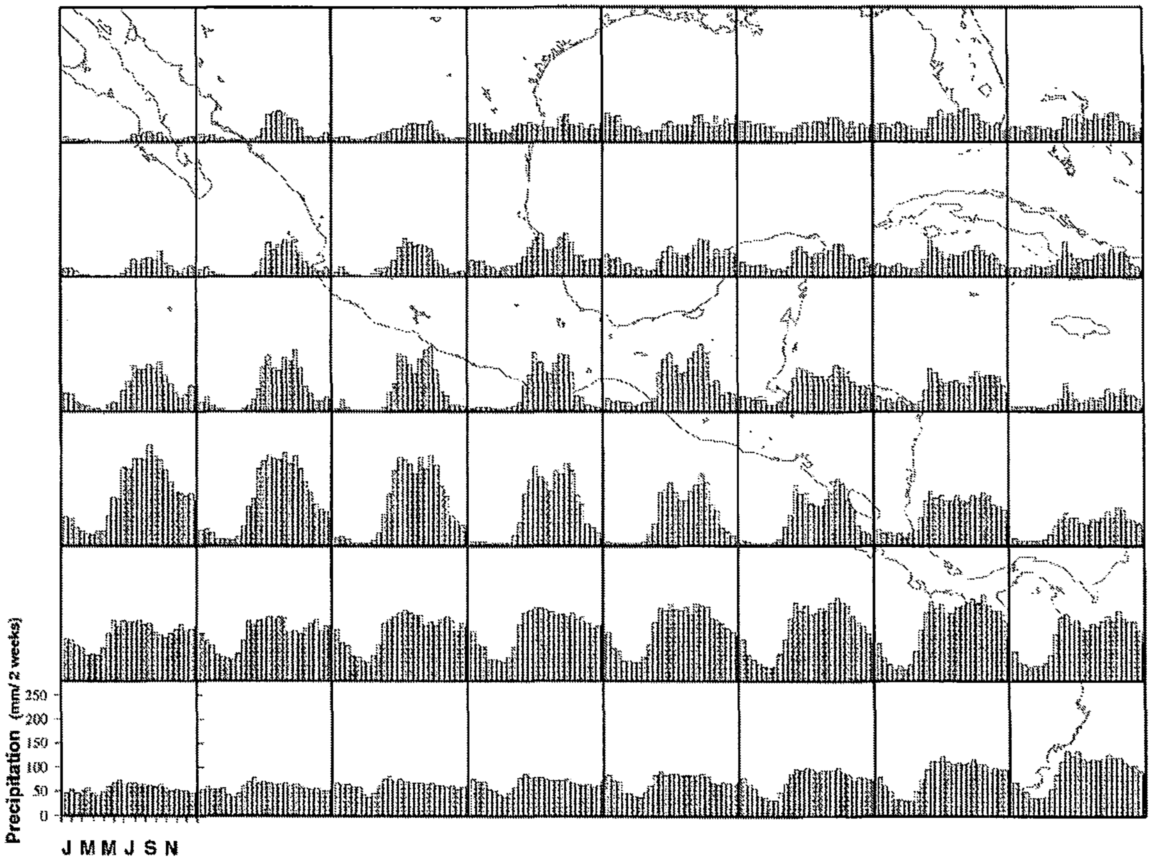

Figure 1-5. Climatological distribution of biweekly precipitation rates (in mm per 2 weeks) for contiguous 5°x5° area. From Magaña *et al.* (1999).

1.2.3) Frequent precipitation anomalies

Meteorological studies in the Central American/Caribbean region have revealed recurrent years of "abnormal" precipitation, related to the fluctuations in the intensity of the annual dry/wet seasonality cycle described in the last paragraph, that are a distinctive feature of the region (Curtis & Hodell, 1996).

It has been shown that unusually wet years are associated with: (1) anomalously low pressure occurring on the equatorward side of the North Atlantic high; (2) northward displacement of the North Atlantic high and trades winds; (3) convergence of the downstream portion of the Northeast Trades; (4) a warm band about 10°-20° N in the North Atlantic ocean extending from Africa all the way to the Americas; and (5) abundant atmospheric moisture due to enhanced convergence and cloudiness over the Caribbean and adjacent low-latitude Atlantic (Curtis & Hodell, 1996). In contrast, dry years are associated with inverse conditions.

The specific nature of Central American climate is also expressed in climatic simulations. Hunt & Elliot (2005) have used a computer-based climatic model (CSIRO Mark 2 coupled model) to generate a worldwide climatic database encompassing 10,000 years: they noticed that anomalies of weak (or heavy) precipitation are only localised on Central America, without relation with other parts of the world. They conclude, saying that these anomalies are due to local climatic disturbances, caused by stochastic perturbations in the topographically constrained wind distribution in the region, rather than general phenomena (like El Niño Southern Oscillation; Hunt & Elliot, 2005).

1.3) Drought definition

A drought can be defined as "a condition of moisture deficit sufficient to have an adverse effect on vegetation, animals, and man over a sizable area" (Warwick, 1975). Several derivatives exist, such as "Meteorological Drought", "Agricultural Drought" or "Hydrologic Drought" (USGS, 2009), with particular measured indices, each relating to different aspects of a drought, but the central theme in the definitions is the concept of water deficit.

The severity of a drought is however somehow complicated to define. Two main indices are used today to measure it in a given area: (1) the Palmer Drought Index (PDI; Palmer, 1965), relating to the humidity balance of the soil (difference between precipitation and evaporation, accounting also for absorption and runoff) compared to the average conditions, and (2) the Standardized Precipitation Index (SPI), measuring the deviation of the actual precipitation from the average conditions.

For clarity reasons, we will use in this paper the definition proposed by Me-Bar & Valdez (2003), presented in table 1-1, based on precipitation variations only. In this table, drought severity categories are cross-related to possible agricultural impacts, and corresponding PDI and SPI indexes are given. Drought definitions are concerned with drought duration of up to one year, but one must keep in mind that drought impacts on given populations are related to the severity of dry events, the occurrence of strings of dry years, their lengths, as well as the sensitivity of agricultural procedures (Me-Bar & Valdez, 2003). It is presumed that the ancient peasants in most areas of the world could sustain a single year of D3 or even a D4 drought (Me-Bar & Valdez, 2003).

Table 1-1. The definitions of the various categories of drought severity (Me-Bar & Valdez, 2003).

Category	Description	% of normal precipitation	Possible impacts	PDI	SPI
D0	Abnormally dry	Below 75% for 3 months	*Going into drought*: short-term dryness; slowing planting, growth of crops/pastures. *Coming out of drought*: some lingering water deficit; pastures/crops not fully recovered.	-1.0 to -1.9	-0.5 to -0.7
D1	Moderate drought	Below 70% for 3 months	Some damage to crops; streams, reservoirs or wells low; some water shortages developing or imminent; voluntary water use restrictions requested.	-2.0 to -2.9	-0.8 to -1.2
D2	Severe drought	Below 65% for 6 months	Crop/pasture losses likely; water shortages common; water restrictions imposed.	-3.0 to -3.9	-1.3 to -1.5
D3	Extreme drought	Below 60% for 6 months	Major crop/pasture loss; widespread water shortages or restrictions.	-4.0 to -4.9	-1.6 to -1.9
D4	Exceptional drought	Below 65% for 12 months	Exceptional and widespread crop/pasture losses; shortages of water in reservoirs, streams, and wells, creating water emergencies.	-5.0 and less	-2.0 and less

1.4) Climate at Flores

The best meteorological data for the region we are interested in comes from Flores (Petén, Guatemala). The location of this city, on the southern shore of Lake Petén-Itza is meaningful in this study because (1) it is a few kilometres away (~10 Km) from the archaeological site of Motul de San José, (2) it is situated between Lamanaï (~150 Km to the north-east) and Piedras Negras

(~150 Km to the west) and (3) the city lies on the path of southeasterly trade winds described in part 1.2.1, that are continuously blowing without being blocked by any orographic feature (see figure 1-2).

Detailed climatic records of monthly averages of temperature, vapour pressure and precipitation recorded at Flores from 1990 to 2006 and are presented in figures 1-6 and 1-7. The three variables exhibit the same annual fluctuation pattern (figure 1-6), but with a time-lag of approximately one month between them.

1.4.1) Temperatures

Minimum temperatures are observed in December and January (~23°C; figure 1-6). From January to May, temperatures are increasing to reach their maximum (~30°C), then a smooth decline is observed from May to September (to ~27°C), followed by an abrupt decrease from September to December.

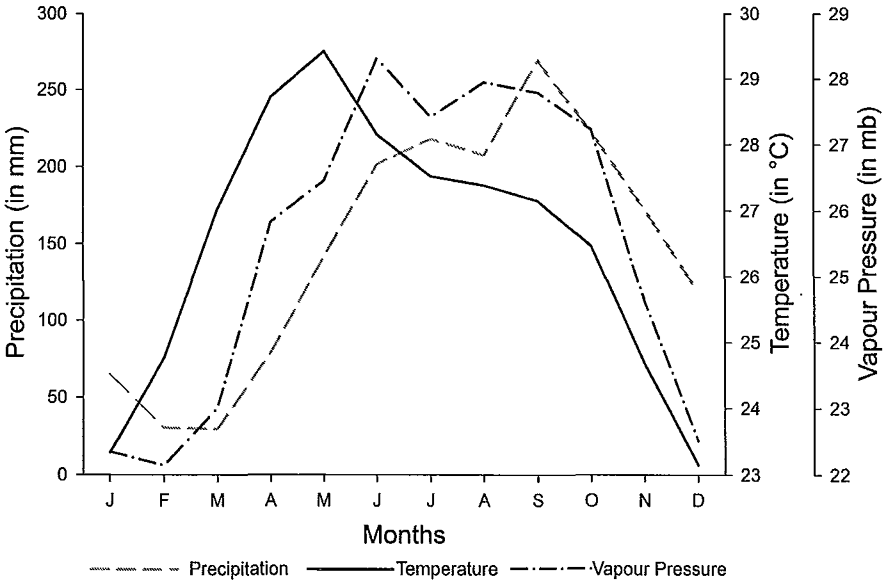

Figure 1-6. Monthly averages of precipitation, temperature and vapour pressure measured at Flores (Petén, Guatemala; 16° 55' 48" N - 89° 52' 59" W; 110 m above sea level) between 1990 and 2006. Data source: INSIVUMEH (2009).

In terms of inter-annual variations (figure 1-7), some years are well-described by the average conditions presented above (e.g.: 1992 and 1993), while others present unusual features such as multiple peaks of temperatures (e.g.: 1996) or large annual thermal amplitude (e.g.: 1999 and 2003).

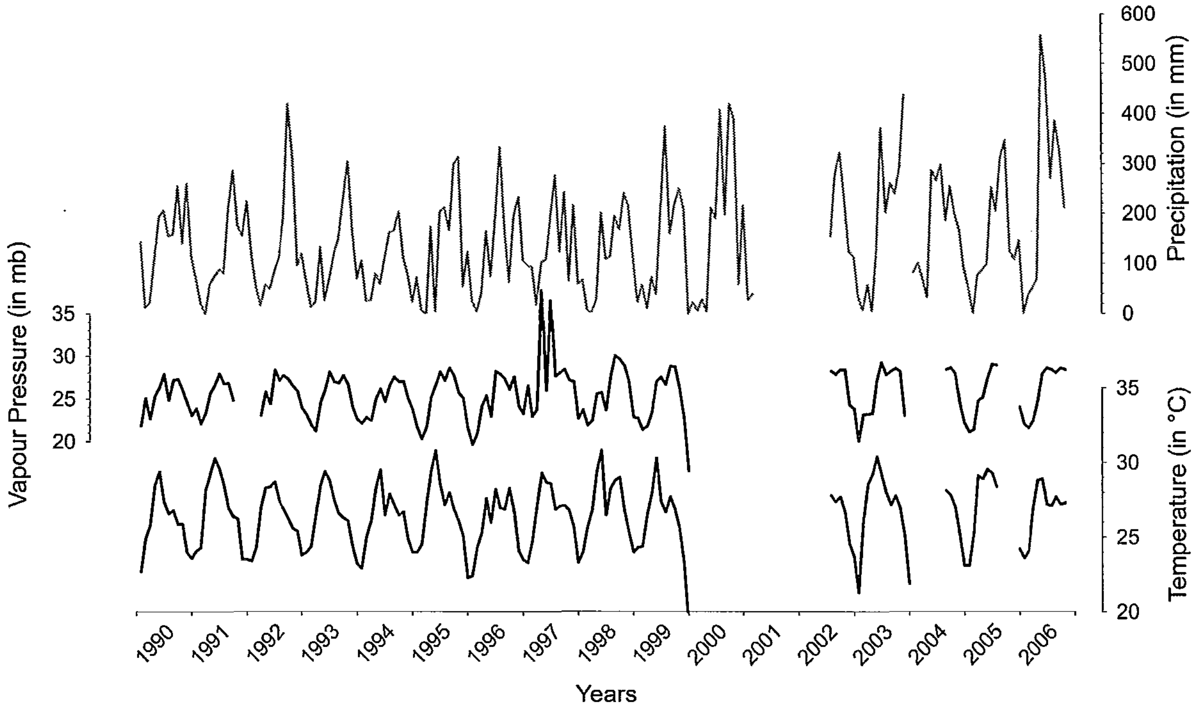

Figure 1-7. Same as in figure 1-6, but here the data is presented per year (monthly resolution).

1.4.2) Vapour pressure

Vapour pressure, the partial pressure of water vapour in moist air, has been calculated from temperature and relative humidity records. It is usually at its lowest value in February (~22 mb; figure 1-6), and starts to increase as temperature does, with a time-lag of one month, to reach its maximum value in June (~28.5 mb). A short and low decrease is observed in July, as the MSD takes place, then the vapour pressure drops sharply in October, still a month after the temperatures did. Again the range of values is similar to the one observed at Veracruz.

If the complete dataset from 1990 to 2006 is considered (figure 1-7), fluctuations of vapour pressure also exhibits a bimodal pattern (e.g.: 1993 and 1995), but sometimes, some "abnormal" features can be observed (e.g. 1997 and 1999), related to temperatures anomalies (like at the end of 1999) or precipitation anomalies (in 1997).

1.4.3) Precipitation

Monthly precipitation is at its lowest point during February and March (~25 mm per month) and reaches a first maximum in June (~220 mm; see figure 1-6). As the MSD takes places, a slight decrease is observed during August (~200 mm), and a second peak occurs in September (>250 mm), one month after the second peak of vapour pressure and three months after the temperature peak.

As expected for the reasons detailed in part 1.2.3, it can be seen that yearly average precipitation can be highly variable (from ~1,200 mm in 1994 to more than 2,400 mm in 2006, average 1990-2006 is ~1,700 mm.year^{-1}: 1994 is then considered as a "D4" drought; see table 1-1). The bimodal precipitation pattern characterized as the MSD is also clearly visible (e.g.: 1991 and 1999), and sometimes, even a three-mode pattern is observed (e.g.: 1990 and 1996).

The variability of yearly average precipitation on a decadal basis is also confirmed by an older climatic dataset from Flores available in Deevey & Rice (1980), presenting average monthly precipitation records for the periods 1934-1942 and 1971-1976. It shows that the period from 1934 to 1942 was relatively wet (average precipitation ~2,000 mm.yr^{-1}) compared with the period of the 1971-1976 (average precipitation ~1,400 mm.yr^{-1}).

Ultimately, no apparent correlation was found between occurrences of El-Niño Southern Oscillation (ENSO) happening in the Southern Pacific and abnormalities of temperature, vapour pressure nor precipitation recorded at Flores between 1990 and 2006.

1.5) Past climate in the Yucatán Peninsula

To emphasize the sensitivity of Yucatán peninsula to abnormalities in moisture balance, one can look to the existing records of past climate. Those records are of two kinds and are briefly presented hereafter: historical records of climatic conditions, as witnessed by the Spanish *conquistadores* and long-term palaeoclimatic reconstructions, recently published.

1.5.1) Historical records

After the invasion of the Yucatán peninsula by the Spanish at the beginning of the 16th century, the administration of the newly discovered territory kept track of famines and droughts in various registers or correspondence. Those records, available in the archives of religious authorities (e.g.: archbishopric registers of Mérida) or national archives (e.g.: Archivo General de la Nación, Mexico), have been studied by numerous historians. A summary of reported droughts and famine from these different archives is available in Gill (2000) and is presented in table 1-2, confirming that droughts were far from being uncommon in the recent history of the Maya region.

Table 1-2. Historical droughts in Yucatán (after Gill, 2000).

Year	Occurrence
1535-1541	Drought, Famine, Locust
1564	Drought
1575-1576	Drought, Famine, Epidemic
1648-1650	Drought, Famine, Epidemic
1650-1654 (*)	Drought, Famine, Epidemic
1669	Drought
1765-1768	Drought, Famine, Locusts, Hurricane
1769-1774 (*)	Drought, Famine, Locusts, Hurricane
1795	Drought
1800-1804 (*)	Drought, Famine, Locust
1805	Drought, Famine
1807	Drought, Famine
1817	Drought, Famine
1822-1823	Drought, Famine
1834-1836	Drought, Famine

(*) indicates a severe famine. See Gill (2000) for various references

1.5.2) Paleoclimatic recontructions

The specificity of Central American climate, along with the repeated historical records of droughts in the Maya region, stimulated the need of going more thoroughly into the study of long term climatic changes in the area. With the advent of new scientific methods of paleoclimatic reconstructions, a great interest rose among mayanists to search for possible evidence of droughts at the time of the Maya collapse(s). Some of those studies are briefly described below and/or presented in table 1-3.

Table 1-3. Collapse, abandonment and some evidence of droughts in the Yucatán. After Gill *et al.* (2007).

Demographic event	Climatic event	Source
Preclassic Abandonment A.D. 150–200	Drought at El Mirador and throughout most of the Yucatán Peninsula	Dahlin, 1983
	Drought at Lake Chichancanab	Hodell *et al.*, 2001
	Drought in Cariaco Basin	Haug *et al.*, 2003
	Drought in stalagmite at Macal Chasm	Webster *et al.*, 2007
	Probable drought at Lake Salpetén	Rosenmeier *et al.*, 2002
	SSS lower in northeastern Caribbean	Nyberg *et al.*, 2001, 2002
Hiatus A.D. 535–590	Drought at Punta Laguna	Curtis & Hodell, 1996
	Drought in stalagmite at Macal Chasm	Webster *et al.*, 2007
	Probable drought at Lake Salpetén	Rosenmeier *et al.*, 2002
	SSS lower in northeastern Caribbean	Nyberg *et al.*, 2001, 2002
Classic Collapse A.D. 760–930	Drought at Punta Laguna	Curtis & Hodell, 1996
	Drought at Lake Chichancanab	Hodell *et al.*, 1995
	Drought in Belizean wetlands	Pope & Jacob, 2002
	Drying at San José Chulchaca	Leyden *et al.*, 1996
	Drought in Cariaco Basin	Haug *et al.*, 2003
	Drought in stalagmite at Macal Chasm	Webster *et al.*, 2007
	Probable drought at Lake Salpetén	Rosenmeier *et al.*, 2002
	SSS lower in northeastern Caribbean	Nyberg *et al.*, 2001, 2002
Postclassic Abandonment A.D. 1450	Drought at Punta Laguna	Curtis & Hodell, 1996
	Drought at Lake Chichancanab	Hodell *et al.*, 2001
	Dry period at Coba	Leyden *et al.*, 1998
	Drought in stalagmite at Macal Chasm	Webster *et al.*, 2007
	Probable drought at Lake Salpetén	Rosenmeier *et al.*, 2002
	SSS lower in northeastern Caribbean	Nyberg *et al.*, 2001, 2002

SSS: Sea-Surface Salinity. Every severe population decline among the Maya is accompanied by drought in the lowlands and lowered SSS in the northeastern Caribbean. The four SSS lowerings are the only ones reported for A.D. 1–1500.

One of the most cited studies (Haug *et al.*, 2003) deals with the titanium content of a marine sediment core from the Cariaco basin, located on the northern coast of Venezuela (see figure 1-3). Titanium is not naturally found in marine environments, and has to be brought in the sediments by river discharge, thus giving information about rainfall over the corresponding drainage area. The position of the northern coast of Venezuela relatively to the movement of the ITCZ being similar to the Yucatán's (figure 1-3), climatic inferences are possible. Haug *et al.* (2003) found that the Classic collapse took place during a period of global dryness, punctuated with pluri-annual episodes of intense droughts, around years 810, 860 and 910 AD, with similar signals of drier climate at the time of Pre-Classic abandonment (~200 AD).

Other studies have been conducted on sediments from lakes located in the Yucatán peninsula. For example, Hodell *et al.* (2007) have analyzed the oxygen and carbon isotopic compositions and lithologic properties (organic matter and carbonate content) on a core from Lake Punta Laguna (northern Yucatán). They found evidence for lower lake levels (due to reduced water input, linked with reduced precipitation) at about the same time as each major discontinuity in the cultural history of the Mayas, the most important taking place between 830 and 890 AD (*i.e.* during the Classic collapse). In the same way, a multi-proxy study (pollen, stable isotopes, elemental composition and magnetic susceptibility) of a core from Lake Petén-Itza (near Flores and Motul de San José) covering the climatic history from the last 3,500 years (Curtis & Hodell, 1996) provides evidence of multi-decadal and millennial-scale changes of alternating wet/dry periods on the peninsula, the drier episodes being again concomitant with phases of cultural change among the Mayas.

Speleothems are also often exploited in climatic reconstructions because they incorporate rainfall derived oxygen into precipitated calcite ($CaCO_3$), and can be precisely dated by Uranium-series isotopes (Latham *et al.*, 1986). Analyzing a stalagmite from the Macal Chasm cave in the Vaca Plateau (northern Belize), Webster *et al.* (2007) were able to provide a reliable climatic record for the past 3,300 years. As in the case of sedimentological studies, the driest period of the record is seen between 700 and 1135 AD, coinciding with the Classic collapse. Dry periods at the time of the Pre-Classic Abandonment, the Maya Hiatus, as well as the Post-Classic Abandonment are also evident in their record.

Lastly, four broader-scale paleoclimatic records can also be mentioned:

(1) The first one concerns the conditions on the Pacific side of the Maya region. It is also a marine sediment core study, but this one comes from a mangrove located on the Pacific shoreline of Guatemala. Examining the chemical composition, pollen grains and phytoliths, Neff *et al.* (2006) have shown that drier conditions have also persisted on the Pacific coast during the Post-Classic period, at a time the area was uninhabited.

(2) The second set of studies (mentioned in table 1-3) was conducted on cores coming from the southern shore of Puerto Rico (northern Caribbean basin; Nyberg *et al.*, 2001, 2002). These works report four major periods of significant decrease of Sea-Surface Salinity (SSS), betraying modifications in thermo-haline circulation patterns in the northern Caribbean basin, at the same time as the Maya collapses and/or phases of abandonment.

(3) Some researchers found no correlation between droughts in the Yucatán and El-Niño Southern Oscillation in the Southern Pacific, as recorded by glacial ice-core data from Quelccaya in the Peruvian Andes (Messenger, 2002).

(4) Some researchers state that supra-regional climatology (linking California, Mesoamerica & South America) is driven by solar cycles with a ~200-year periodicity (Schimmelmann *et al.*, 2003).

The four examples presented above are mentioned because they tend to show that not only very local climatic perturbations could have been involved in the Maya collapses (see part 1.2 above), but some broader-scale mechanisms might have played a role, even if this assumption is still uncertain, and will not be approached further in the present study.

1.6) Conclusions

The isthmus linking southern and northern Americas, between the Pacific and Atlantic oceans is located in a zone where several climatic phenomena occur, giving unique climatic features to Central America. The Maya area is characterized by marked wet/dry seasonality, with a bimodal distribution of precipitation during the rainy season, and frequent precipitation anomalies, leading to recurrent droughts. Fortunately, present climatic databases are available in the zone the samples we are analyzing are coming from, confirming the repeated occurrence of droughts in the region.

The increasing amount of available paleoclimatic reconstructions appears to make the concordance between dry episodes in the circum-Caribbean basin and cultural transition phases in the Maya history less and less questionable. However, the main difficulty when assessing the impact of climate change on cultural transformations is the precise determination of the timing, magnitude and extent of the climate and cultural changes. Moreover, the effects of droughts cannot be generalized in all the Maya area, because of the high spatial variability of Yucatán's climate, as well as the differences between land use and settlement histories, that can also have an impact on how droughts can affect some populations more than others.

In this context, the use of deer bones to track droughts in the Maya area is of a great interest, because (1) they are relatively abundant in the Maya archaeological record, (2) they are associated with cultural remains, allowing them to be easily and accurately dated, and (3) most importantly, they specifically record relative humidity conditions at a very local scale like no other proxy (as will be expanded in Chapter 3).

References

Aimers J.J. (2007) - What Maya collapse ? Terminal Classic variation in the Maya Lowlands. *Journal of Archaeological Research* 15, (4):329-377.

Black D.E., L.C. Peterson, J.T. Overpeck, A. Kaplan, M.N. Evans, M. Kashgarian (1999) – Eight Centuries of North Atlantic Ocean Atomosphere Variability. *Science* 286, 1709-1713.

CNA (2009) - Comisión Nacional de Agua (Mexico). *Servicio Meteorológico Nacional.* Accessed online <http://smn.cna.gob.mx>, July 2009.

Curtis S. & D.A. Hodell (1996) - Climate Variability on the Yucatán Peninsula (Mexico) during the Past 3500 Years, and Implications for Maya Cultural Evolution. *Quaternary Research 46*, 37-47.

Curtis S. & D.W. Gamble (2008) - Regional variations of the Caribbean mid-summer drought. *Theoretical and Applied Climatology* 94, 25–34.

Dahlin B.H. (1983) - Climate and Prehistory on the Yucatán Peninsula. *Climate Change* 5, 245–263.

Dahlin B.H. (2002) – Climate Change and the end of the Classic period in Yucatán, resolving a paradox. *Ancient Mesoamerica* 13, 327–340

Deevey E.S. & D.S. Rice (1980) - Coluviacion y retencion de nutrientes en el distrito lacustre del Peten central, Guatemala. *Biotica* 5, 129-144.

Folan W.J., J. Gunn, J.D. Eaton, R.W. Patch (1983) - Paleoclimatological Patterning in Southern Mesoamerica. *Journal of Field Archaeology* 10, (4):453-468.

Giannini A., Y. Kushnir, M.A. Cane (2000) - Interannual variability of Caribbean rainfall, ENSO, and the Atlantic Ocean. *Journal of Climate* 13, 297–311.

Gill R.B (2000) – The Great Maya droughts, Water, Life, and Death. University of New Mexico Press. Albuquerque.

Gill R.B., P.A. Mayewski, J. Nyberg, G.H. Haug, L.C. Peterson (2007) – Drought and the Maya Collapse. *Ancient Mesoamerica* 18, 283–302.

Hastenrath S. (1967) - Rainfall distribution and regime in Central America. *Archiv für Meteorologie, Geophysik und Bioklimatologie* 15B, 201–241.

Hastenrath S. (1976) - Variations in low-latitude circulation and extreme climatic events in the tropical Americas. *Journal of the Atmospheric Sciences* **33,** 202–215.

Haug G.H., D. Günther, L.C. Peterson, D.M. Sigman, K.A. Hughen, B. Aeschliman (2003) - Climate and the collapse of Maya civilization. *Science* 299, 1731-1735.

Hodell D.A., M. Brenner, J.H. Curtis (1995) - Possible Role of Climate in the Collapse of Classic Maya Civilization. *Nature* 375, 391–394.

Hodell D.A., M. Brenner, J.H. Curtis, T. Guilderson (2001) - Solar Forcing of Drought Frequency in the Maya Lowlands. *Science* 292, 1367–1370.

Hodell D.A., M. Brenner, J.H. Curtis (2007) - Climate and cultural history of the Northeastern Yucatán Peninsula, Quintana Roo, Mexico. *Climatic Change* 83, 215-240.

Hunt B.G. & T.I. Elliot (2005) - A simulation of the climatic conditions associated with the collapse of the Maya civilization. *Climatic Change* 69, 393-407.

INSIVUMEH (2009) – Instituto Nacional de Sismologia, Vulcanologia, Meteorolgia e Hidrologia (Guatemala). *Estadísticas Climáticas.* Accessed online <http://www.insivumeh.gob.gt>, August 2008.

Latham A.G., H.P. Schwarcz, D.C. Ford (1986) - The paleomagnetism and U-Th dating of Mexican stalagmite, DAS2. *Earth & Planetary Science Letters* 79, (1-2):195-207.

Leyden B.W., M. Brenner, T. Whitmore, J.H. Curtis, D.R. Piperno, B.H. Dahlin (1996) - A Record of Long- and Short-Term Climatic Variation from Northwest Yucatán: Cenote San José Chulchaca. In The Managed Mosaic: Ancient Maya Agriculture and Resource Use, Scott L. Fedick (ed), University of Utah Press, Salt Lake City.

Magaña V., J.A. Amador, S. Medina (1999) - The midsummer drought over Mexico and Central America. *Journal of Climate* 12, 1577–1588.

Me-Bar Y., F. Valdez (2003) – Droughts as random events in the Maya lowlands. *Journal of Archaeological Science* 30, 1599-1606.

Mendoza B., V. García-Acosta, V. Velasco, E. Jáuregui, R. Díaz-Sandoval (2007) - Frequency and duration of historical droughts from the 16th to the 19th centuries in the Mexican Maya lands, Yucatán Peninsula. *Climatic Change 83*, 151-168.

Messenger L.C. (2002) - Los Mayas y el Niño - Paleoclimatic correlations, environmental dynamics, and cultural implications for the ancient Maya. *Ancient Mesoamerica* 13, 159-170.

Murck B.W., B.J. Skinner, S.C. Porter (1997). Dangerous Earth, An Introduction to Geologic Hazards. John Wiley & Sons (Eds), New York.

Neff H., D. M. Pearsall, J. G. Jones, B. Arroyo De Pieters, D. E. Freidel (2006) - Climate change and population history in the Pacific Lowlands of Southern Mesoamerica. *Quaternary Research* 65, 390-400.

Nyberg J., A. Kuijpers, B.A. Malmgren, H. Kunzendorf (2001) - Late Holocene Changes in Precipitation and Hydrology Recorded in Marine Sediments from the Northeastern Caribbean Sea. *Quaternary Research* 56, 87–102.

Nyberg J., B.A. Malmgren, A. Kuijpers, A. Winter (2002) - A Centennial-Scale Variability of Tropical North Atlantic Surface Hydrography during the Late Holocene. *Palaeogeography, Palaeoclimatology, Palaeoecology* 183, 25–41.

Palmer W.C. (1965) - Meteorological Drought. Research Paper No. 45. Department of Commerce, Washington D.C.

Pope K. & J. Jacob (2002) - The Maya Drought in Northern Belize: A New Look at Gypsum in Maya Wetlands. In *Abstracts of the 67th Annual Meeting of the Society for American Archaeology.* Society for American Archaeology, Washington DC.

Rosenmeier M.F., D.A. Hodell, M. Brenner, J.H. Curtis (2002) - A 4000-Year Lacustrine Record of Environmental Change in the Southern Maya Lowlands, Peten, Guatemala. *Quaternary Research* 57, 183–190.

Shimmelmann A., C.B. Lange, B.J. Meggers (2003) – Palaeoclimatic and archaeological evidence for a 200- yr recurrence of floods and droughts linking California, Mesoamerica and South America over the past 2000 years. *The Holocene* 13, (5):763-778.

Schultz D., E. Bracken, L. Bosart, G. Hakim, M. Bedrick, M. Dickinson, K. Tyle (1997) - The 1993 superstorm cold surge frontal structure and tropical impact. *Monthly Weather Review* 125, 5–39.

USGS (2009) – United States Geological Survey. *Droughts.* Accessed online <http://nd.water.usgs.gov/drought/faqs/faq1.html>, August 2008.

Warwick R.A. (1975) - Drought hazard in the United States: A research assessment. University of Colorado, Institute of Behavioral Science.

Webster J.W., G.A. Brook, L.B. Railsback, H. Cheng, R. Lawrence Edwards, C. Alexander, P.P. Roeder (2007) - Stalagmite Evidence from Belize Indicating Significant Droughts at the Time of the Preclassic Abandonment, the Maya Hiatus, and the Classic Maya Collapse. *Palaeogeography, Palaeoclimatology, Palaeoecology* 28,1–17.

Williams A. (1976) - The Interpretation of Rainfall Patterns in Northern Yucatán Utilizing Meteorological Satellite Imagery. *Proceedings of the Association of American Geographers* 8, 15–19.

Witschey W.R.T. & C.T. Brown (2009) - The Electronic Atlas of Ancient Maya Sites. Accessed online <http://mayagis.smv.org>, July 2009 (Copyright).

Chapter 2 - Sample Materials

In this chapter, the materials analysed in this study are first presented and described. I then present a summary of information about bone itself: structure, mechanisms of formation, and mineralogical aspects. These data will be needed for a precise comprehension of the methodology we will use (see Chapter 4), as well as the interpretation of the results (Chapters 5 and 6).

2.1) Deer bones

The studied material consists of a total of 98 bones of white-tailed deer (*Odocoileus virginianus* sp.) that have been excavated from the archaeological sites of Piedras Negras (PN; 71 bones), Motul de San José (MSJ; 12 bones), both located in the Departamento del Petén, Guatemala, and Lamanai (LAM; 15 bones), located in Orange Walk District, Belize. Those bones were excavated by Drs. Stephen Houston and Hector Escobedo (PN), Drs. Antonia Foias and Kitty Emery (MSJ) and Drs. Elizabeth Graham and David Pendergast (LAM; Figure 2-1).

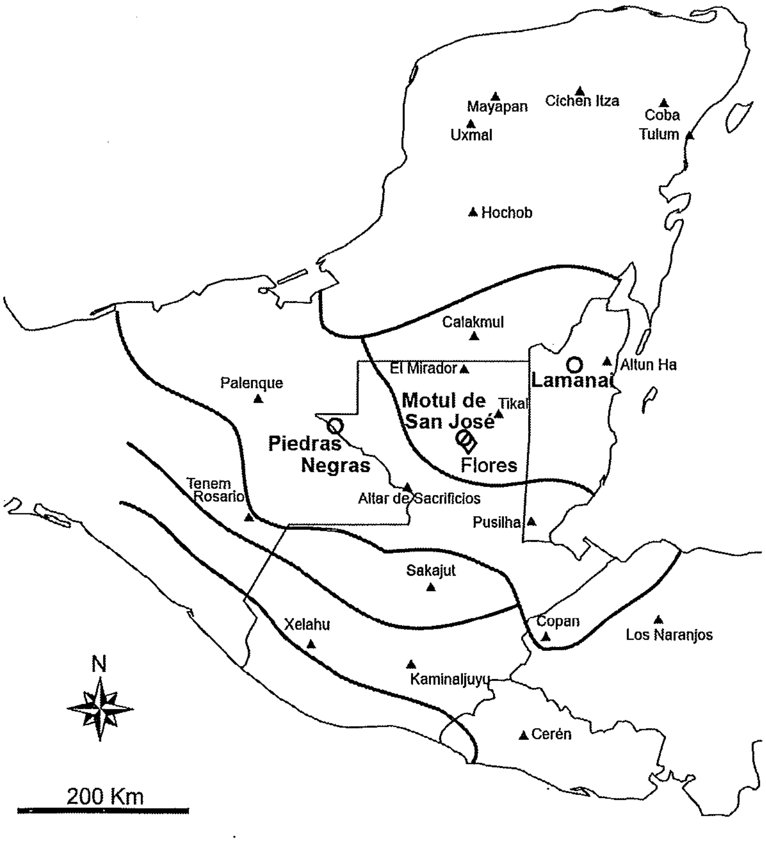

Figure 2-1. Location of the three archeological sites (**o**) the samples were excavated from (Lamanai & Motul de San José, Central Lowlands; Piedras Negras, Southern Lowlands), and the weather station of Flores (◊) mentioned in Chapter 1). A few other maya archeological sites are shown (▲).

Bones were identified to taxon, element, side and age by Dr. Kitty Emery and Erin Thornton, and samples from separate adult individuals were selected for this study. All bones are from assemblages well-dated by stratigraphic analysis of the presence or absence of ceramic wares (Harris, 1979; table 2-1), and range from Pre-Classic (LAM and PN) to Post-Classic periods (LAM, MSJ and PN). A few post-colonial bones were also available from Lamanai.

Table 2-1. Origin, age, type and number of bones analyzed in this study.

Cultural phase	Years (AD)	Number of bones	Bone types
Lamanai			
Pre-Classic	Before 300	2	Astragalus, Calcaneus
Post-Classic	1000-1519	6	Astragalus , Calcaneus, Metacarpal
Colonial	1519-1821	7	Astragalus
	All phases	*15*	
Motul de San José			
Late Classic	600-800	6	Femur
Terminal Classic	800-1000	5	Humerus, Rib, Tibia, Coxa
Early Post-Classic	1000-1250	1	Metatarsal
	All phases	*12*	
Piedras Negras			
Abal/Pom	300BC - 350	2	Metatarsal, Ilium
Naba	350-560	4	Mandible, Ilium, Humerus
Balche	560-620	12	Mandible, Tibia, Scapula, Calcaneus, Acetabulum, Vertebrae, Femur
Yaxche	620-750	26	Calcaneus, Femur, Humerus, Phalanx, Astragalus, Ilium, Radius, Ischium, Mandible, Scapula, Pubis
Chacalhaaz	750-850	24	Phalanx, Tibia, Ilium, Femur, Ischium, Astragalus, Metatarsus, Humerus, Metapodial, Mandible, Radius, Metacarpal, Scapula
Kumche	850-900	3	Metatarsal, Tibia,
	All phases	*71*	

2.2) Bone structure

Bones form a family of highly complex, heterogeneous and composite connective tissues, characterized by the mineralized nature of their extra-cellular matrix. In addition to its mechanical function, bone can be seen as an organ because of its two fundamental biological functions: (1) a metabolic function, by stocking and releasing several mineral salts, contributing to the phosphocalcic metabolism and (2) a hematopoietic function, by hosting the bone marrow, containing the stem cells of the three lineages of blood corpuscles.

2.2.1) Hierarchical levels of organization

As for other Tetrapods, seven hierarchical levels of organisation are distinguished for mammalian bones (see figure 2-2; Weiner & Wagner, 1998; Cui & Wang, 2007).

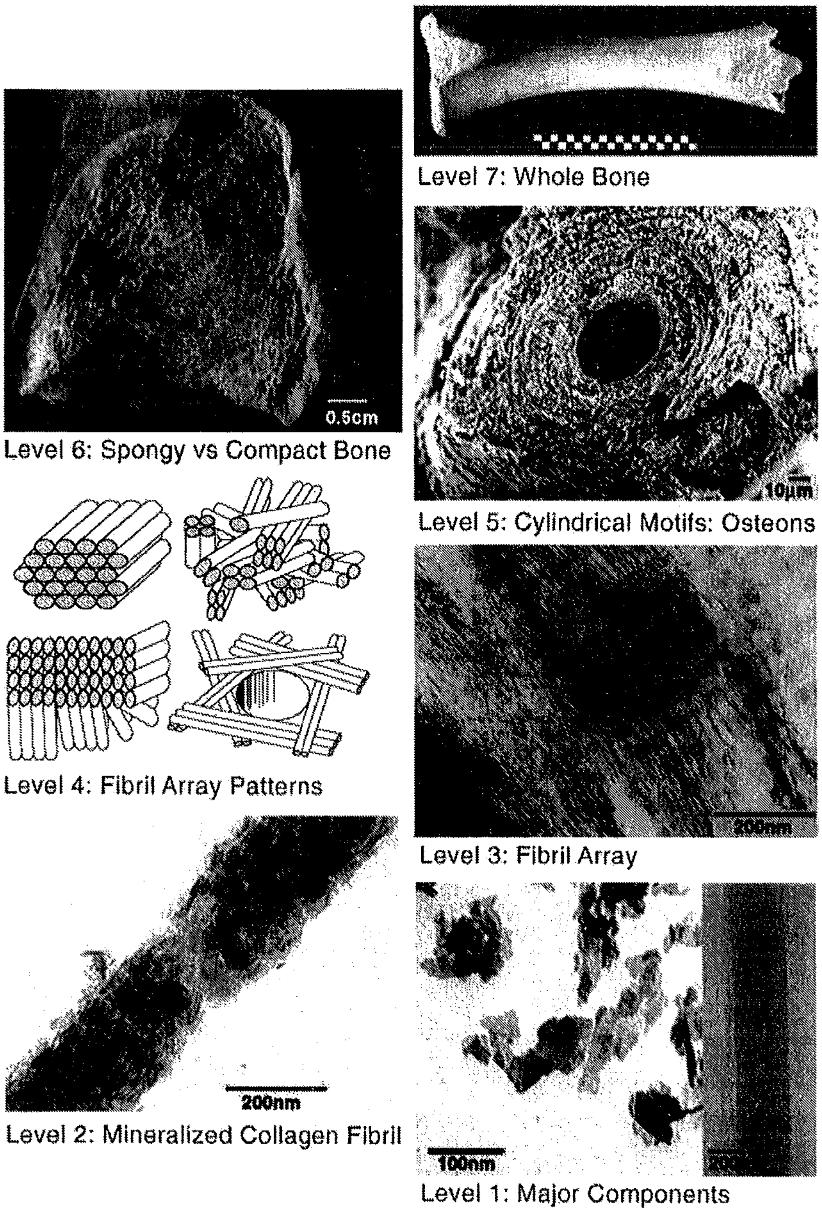
Level 7: Whole Bone

Level 6: Spongy vs Compact Bone

Level 5: Cylindrical Motifs: Osteons

Level 4: Fibril Array Patterns

Level 3: Fibril Array

Level 2: Mineralized Collagen Fibril

Level 1: Major Components

Figure 2-2. The 7 hierarchical levels of organization of bone tissues. Level 1: isolated crystals from human bone (left) and part of unmineralized collagen fibril from turkey tendon observed in Transmission Electron Microscopy (TEM, right). Level 2: TEM micrograph of mineralized collagen fibril from turkey tendon. Level 3: TEM micrograph of a thin section of mineralized turkey tendon. Level 4: four fibril array patterns of organization found in the bone family of materials. Level 5: Scanning Electron Microscopy (SEM) micrograph of a single osteon from human bone. Level 6: Light micrograph of a fractured section through a fossilized (about 5500 years old) human femur. Level 7: whole bovine bone (scale 10 cm). From Weiner & Wagner, 1998.

The last level (level 7) is the level used to describe at the organ scale. At that level, it is possible to distinguish different types of bones (e.g.: long, flat), with distinct functions. At the centimetre scale, level 6 distinguishes the two different types of anatomical structures encountered in a bone: a dense external shell (cortical bone), and a porous material (cancellous bone; Fratzl & Gupta, 2007). Long bones (e.g.: tibia) consist of an outer cylinder of cortical bone surrounding a marrow cavity including struts of cancellous bone. Short bones (e.g.: finger bones) are similar in structure to long bones, but do not contain bone marrow. Flat bones (e.g.: ribs) consist of two layers of cortical bone tightly enclosing a layer of cancellous bone.

At a millimetre scale, cortical bone has usually a lamellar structure, consisting of successive layers of parallel mineralized collagen fibrils (level 3), assembled in plywood-like structure (level 4). Each blood vessel in cortical bone is surrounded by concentric bone lamellae (Cui & Wang, 2007). The central channel for the blood vessel and the surrounding lamellae form an *osteon*, the structural unit of cortical bone, also referred as level 5 of hierarchical organization (Fratzl & Gupta, 2007).

At the micrometer scale, the basic building block of the bone is the mineralized collagen fibril (level 2). At the nanometer scale, the level 1 of hierarchical organization of bone is represented by its major elemental components (*i.e.* mineral and collagen). On average, only about 20% of bone's volume is made of mineralized tissues, the remainder consists in bone marrow (Fratzl & Gupta, 2007).

2.2.2) The mineralized collagen fibril

According to Weiner & Wagner (1998), the term bone refers to "*a family of materials each with a somewhat different structural motif, but all having in common the basic building block, the mineralized collagen fibril*".

As well as for other connective tissues (*i.e.* skin, dentin, cementum, ligaments and tendons), the principal component (85-90 wt.%; Fratzl & Gupta, 2007) of bone's organic matrix is type I collagen, a large insoluble fibrous protein. Collagen is the protein that gives the flexibility to the other connective tissues, but its association with the mineral component of bone makes it rigid, also giving bone its load-bearing capacity (Fratzl *et al.*, 2004). The remaining 10-15 wt.% of the organic matrix corresponds to other non-collagenous proteins, mainly phosphorylated proteins, playing several roles in the mineralization processes.

In mature deer bones, the organic matrix represents ~30 wt.% of the bone, into which mineral crystals grow, forming the ~70 wt.% remaining inorganic matrix (Weiner & Wagner, 1998; Wright & Schwarcz, 1996). The average mineral content is species-dependant and lies between the range of 50-74 wt.% (30-55 vol.%; e.g.: Bloebaum *et al.*, 1997): deer bones are in the upper range of average mineral content.

2.3) Osteogenesis

The processes of bone formation (osteogenesis) are extremely complicated and require a long detour through biology that cannot be done here (see Glimcher, 2006 for a summary of the most recent progresses about that subject). In the present work, we will address only two aspects of osteogenesis that are critical in the present work: the bone remodelling and the biomineralization patterns.

2.3.1) Bone remodelling

The bone matrix is in a dynamic state, continuously resorbed and re-deposited by the activity of the two main lineages of bone specialized cells, osteoclasts and osteoblasts, respectively.

- The osteoclasts are the bone destroying cells. While mature, those cells secrete active enzymes, such as acid phosphatase, causing dissolution of the mineral substrate (Teitelbaum, 2000). In cortical bone, osteoclasts are organized as a cone ("destructive" or "cutting cone") and dig tunnels through the mineralized tissue; those resorption spaces are subsequently filled with new organic matrix deposited by osteoblasts (organized in a "closing cone"), forming new concentric lamellar structures (*i.e.* new osteons, see VanOers *et al.*, 2007). This process involves the obliteration of the previous osteons by newly formed ones (secondary intracortical remodelling)

- The osteoblasts are the bone-forming cells. In cortical bone, they progressively deposit the organic matrix (*ossification*), where the mineral crystals precipitate. It has been shown that osteoblasts release alkaline phosphatase (a weak base) in the surrounding organic matrix, locally increasing the pH, resulting in the precipitation of mineral crystals, from the chemical species present in the extracellular fluids (see Currey, 2002 for more references).

Because of the permanent remodelling of mineralized collagen fibrils, osteons of different age coexist in the same bone, leading to a pronounced local variation (at the length scale of 10 to 100 μm) of the mineralization degree of the tissue (Fratzl *et al.*, 2004).

Little is known about deer bone turnover rate, but some studies have shown that bone remodelling during antler growth is similar in some aspects to the remodelling of bone during growth. Deer antlers are not superficial body growth like hair, nail or horns, but they are true bone extensions, thus also made of bioapatite. During antler growth, the high demand on mineral salts induces increased rates of bone resorption, causing temporary osteoporotic conditions, and those processes seem to be strongly bone-dependent (Hillman *et al.*, 1973; Baxter *et al.*, 1999). In humans, it has been estimated that the total mass of bone in the skeletal system is synthesized and resorbed every five to six years, again with large differences in turnover rate between bones or bone regions (Glimcher, 2006).

2.3.2) Biomineralization patterns

The exact mechanisms of crystal nucleation and growth within the collagen framework (biological mineralization or biomineralization, sometimes referred as *calcification*; Weiner & Wagner, 1998) are not very well established. The role of each protein is yet to be identified mainly because of the difficulty of *in vivo* analysis of the process at the nanoscale (Dorozhkin, 2007).

The mineralization of the newly formed bone matrix follows a particular pattern. It has been shown that in human bone matrix, the mineralization of the deposited collagenous fibrils starts after a lag time of 13 days. Within a few days, those fibrils mineralize up to 70% of the full mineralization capacity (primary mineralization). The reaching of the remaining 30% mineralization capacity (second mineralization or maturation) lasts several years (Akkus *et al.*, 2003). It is assumed here that a similar pattern occurs during deer bone mineralization.

2.4) Mineralogical aspects of bones

2.4.1) Crystallites

Mineral crystals in bone are plate-like, and are probably the smallest biologically formed crystals known (*i.e.* nanocrystals or crystallites; Weiner & Traub, 1992). Their average dimensions are approximately 50×20×3 nm, but their size can vary from 10 to more than 100 nm long (refer to figure 2-3 for a spatial representation of the collagen-crystal association in the bone; Weiner & Wagner, 1998; Surovell & Stiner, 2001).

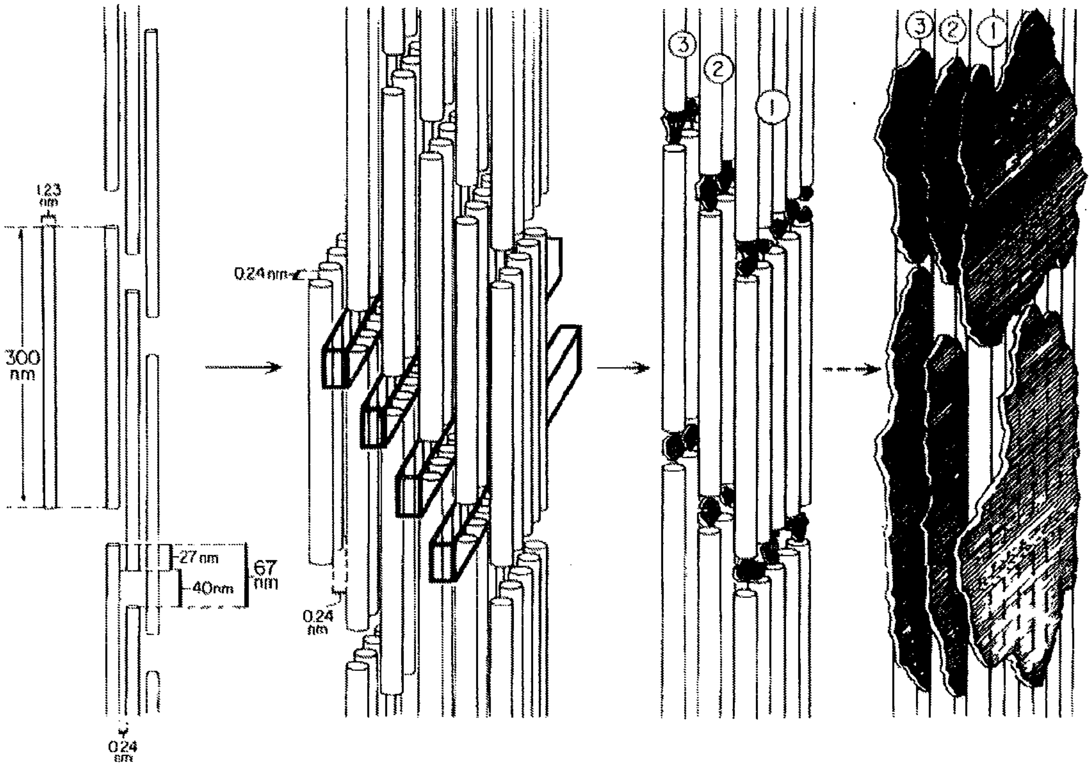

Figure 2-3. Three-dimensional representation of collagen assembly and association with mineral crystal in bone. The first sketch (left) is showing the organization and dimensions of the collagen fibrils. Bioapatite crystals are thought to nucleate in the 40 nm gaps between the bundles of collagen (2nd and 3rd sketch). The crystals are growing in a plate-like pattern and end by occluding the collagen fibrils (right sketch). From Landis, 1996.

2.4.2) Bio-apatite

The mineral of which bone crystallites are made is called bioapatite, and belongs to the apatite group, a group of phosphate minerals. The apatite mineral group is a group of isomorphous hexagonal minerals (*i.e.* the same hexagonal molecular arrangement). The general formula of the group is:

$$Me_{10}(XO_4)_6Y_2$$

where ***Me*** represents a divalent metal cation (Ca^{2+}, Ba^{2+} or Sr^{2+}), ***XO_4*** is a trivalent anion (PO_4^{3-}, AsO_4^{3-} or VO_4^{3-}), and ***Y*** a monovalent anion (F^-, Cl^- or HO^-). However, there are only three types of apatites *stricto sensu* (*i.e.* true, classical apatites, that are calcium phoshphate apatites): fluorapatite, hydroxylapatite and chlorapatite, designated by the general formula $Ca_{10}(PO_4)_6(F,HO,Cl)_2$.

Bioapatite has been described as a poorly crystalline (see below) distinctive type of non-stoechiometric hydroxylapatite closely related to geological dahllite (Surovell & Stiner, 2001). The pure end-member hydroxylapatite has a composition of $Ca_5(PO_4)_3OH$, often written $Ca_{10}(PO_4)_6(OH)_2$, to show the two formula units in the crystallographic unit cell (see figure 2-4; Wopenka & Pasteris, 2005).

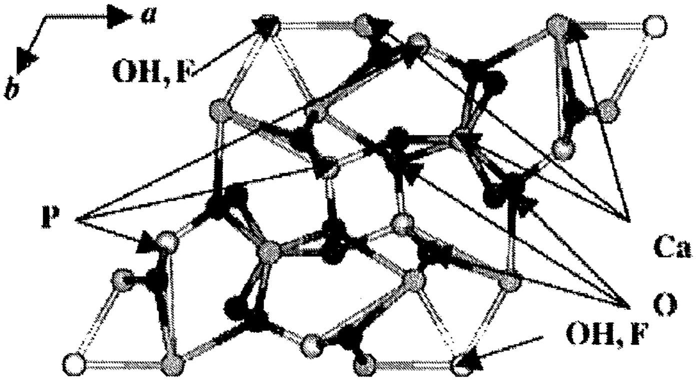

Figure 2-4. Structure of the hexagonal apatite unit cell, showing the position of the fluoride or hydroxyl anions in the *c*-direction into the plane of the paper [O = black, Ca = dark grey, P = light grey, F (or HO) = white]. From DeLeeuw, 2001.

Four different types of crystallographic positions are distinguished in the apatite unit cell: (1) six "tetrahedral sites" for the six PO_4^{3-} groups, (2) four "Ca[1]" sites for four of the Ca^{2+} ions,

(3) six "Ca[2]" sites for the six other Ca^{2+} ions, and (4) the "channel-site", typically occupied by two monovalent anions (*Y*). The channel-site is formed by the particular spatial arrangement of the six Ca[2] sites along the *c*-axis of the crystallographic unit cell (Wopenka & Pasteris, 2005). The spatial conformation of the channel site involves a high lability of the monovalent anions. Because the hydroxyl anion (HO^-) is not spherical (as F^- is), hydroxylapatite has a lower symmetry than fluorapatite ($Ca_5(PO_4)_3F$), and is therefore monoclinic rather than hexagonal (space group $P2_1/b$ rather than $P6_3/m$), constraining the overall shape and size of bioapatite crystals (Elliott *et al.*, 1973).

2.4.3) Crystallinity

"Crystallinity" is the term used to refer that degree of order within the lattice. A material is crystalline if its clusters of atoms or unit cells are repeated multiple times and are arranged in a predictable spatial pattern throughout (Wopenka & Pasteris, 2005). High crystallinity is defined by large crystal size and/or and regular crystal lattice, resulting in low strain exerted on the crystals (see figure 2-5 and Chapter 4, part 4.1 for further aspects of bioapatite crystallinity).

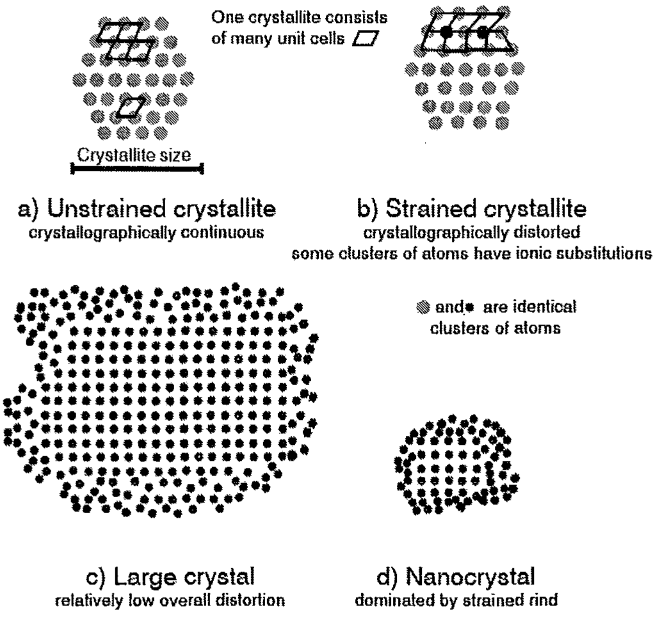

Figure 2-5. Simplified representations of the reiterations of identical clusters of atoms in the crystal lattice. A crystallographically continuous crystallite is consisting of many unit cells, all exactly the same (*i.e.* a regular crystal lattice) as shown in (**a**). Sometimes, the crystallite regularity is distorted (**b**) because of the inclusion of irregular clusters of atoms ("impurities" in the crystal lattice). The chemical bonds of the ionic units exposed at the surface of a crystal are electronically unsatisfied, causing a rind of distortion in the position of the nearby atoms at the surface of the crystal (lack of charge balance). In (**c**), the crystal has a big size, so that the distorted rind is volumetrically less significant than in the case of a nanocrystal (**d**), as found in bone apatite (after Wopenka & Pasteris, 2005).

2.4.4) Substitutions

Unlike most other minerals, apatite is likely to accommodate chemical substitutions (Wopenka & Pasteris, 2005). Geological apatites are able to incorporate half the elements of the periodic chart in their crystal lattice (Pan *et al.*, 2002). Those substitutions (that can be seen as "impurities") are introducing stresses into the crystal lattice, making apatites less stable and more reactive than any other mineral (Dorozhkin, 2007). While biologically formed, the number of substitutions possible in apatite is smaller, due to the limited bioavailability of some elements, but the following are known or reported (among others): F^-, Cl^-, Na^+, K^+, Fe^{2+}, Zn^{2+}, Sr^{2+}, Mg^{2+}, citrate and carbonate (Piccoli & Candela, 2002). The biochemical controls and regulation of the inclusion of those substitutions allow the adjustment of plasticity and physiologic characteristics of bones, such as crystallinity and dissolution rate during bone remodelling processes.

Bone apatite contains approximately 7 wt.% carbonate (CO_3^{2-}, Elliott, 2002), but there is still dissension among mineralogical community about how those ions are incorporated into the apatite lattice or adsorbed at the surface of the crystallite. However, carbonate ions can substitute in the lattice only in two sites: (1) in the channel-site (HO-site, "type-A" substitution), or (2) in one of the tetrahedral site (PO_4-site, "type-B" substitution; Wopenka & Pasteris, 2005). The latter type-B substitution seems the most frequent ionic substitution in bioapatite (Wright & Schwarcz, 1996). It has been shown on artificially-produced apatites that type-B substitutions in the crystal lattice affect several aspects of the physical properties of hydroxylapatite, such as crystal size (decrease in the *a*-axial length and increase in the *c*-axial length, or in other words, a stretching of the crystals), and consequently the degree of crystallinity of the crystal lattice (Wopenka & Pasteris, 2005).

Ultimately, very small dimensions, high frequency of substitutions and constant resorption/redeposition are the three major features of bioapatite crystals in bone (Dorozhkin, 2007).

2.5) Conclusions

Taking into account that (1) the life expectancy of wild white-tailed deer is about 10 years (some specimens were reported to be more than 15 years old; DelGiudice *et al.*, 2007), (2) the strong spatial variation of mineral content in bone at a micrometer scale, (3) the temporal pattern of mineralization and (4) the sampling protocol (see Chapter 4, part 4.1), *i.e.* the sampling of a bulk bone mass of a few grams (containing thousands of mixed osteons), it is considered that it is impossible to distinguish the temporal origin (within the span of deer's life) of the analyzed mineral content.

In other words, due to the combination of the resolution of the sampling strategy and osteogenesis mechanisms, the mineral content of each analyzed sample is likely to represent a "time-average" of about 10 years of biomineralization processes.

References

Akkus O., A. Polyakova-Akkus, F. Adar, M.B. Schaffler (2003) - Aging of micro-structural compartments in human compact bone. *Journal of Bone and Mineral Research* 18, (6):1012-1019.

Baxter B.J., R.N. Andrews, G.K. Barrell (1999) – Bone turnover associated with antler growth in red deer (Cervus elaphus). *The Anatomical Record* 256, 14-19.

Bloebaum R.D., J.G. Skedros, E.G. Vajda, K.N. Bachus, B.R. Constantz (1997) - Determining mineral content variations in bone using backscattered electron imaging. *Bone* 20, (5):485-490.

Cui F.-Z. & X.-M. Wang (2007) - Mechanical and structural properties of skeletal bone in wild-type and mutant Zebrafish (Danio rerio). Handbook of Biomineralization, *Vol 1 - Biological aspects and structure formation.* E. Bäuerlein. Weinhein, WILEY-VCH.

Currey J.D. (2002). Bones - Structure and Mechanics. Princeton, Princeton University Press.

De Leeuw N.H. (2001) - Local ordering of hydroxy groups in hydroxyapatite. *Chemical Communications* (17), 1646-1647.

Delgiudice G.D., M.S. Lenarz, M.C. Powell (2007) - Age-specific fertility and fecundity in northern free-ranging white-tailed deer: Evidence for reproductive senescence? *Journal of Mammalogy* 88, (2):427-435.

Dorozhkin S.V. (2007) - Calcium orthophosphates. *Journal of Materials Science* 42, (4):1061-1095.

Elliott J.C., P.E. Mackie, R.A. Young (1973) - Monoclinic Hydroxyapatite. *Science* 180, (4090):1055-1057.

Elliott J.C. (2002) - Calcium phosphate biominerals, in: M.J. Kohn, J. Rakovan, J.M. Hughes (Eds.), Phosphates: Geochemical, Geobiological and Material Importance, Reviews in Mineralogy and Geochemistry, vol. 48, Mineralogical Society of America, Washington, DC, 2002, pp. 427– 454.

Fratzl P. & H.S. Gupta (2007) - Nanoscale mechanisms of bone deformation. Handbook of biomineralization, *Vol 1 - Biological aspects and structure formation.* E. Bäuerlein. Weinheim, WILEY-VCH.

Fratzl P., H.S. Gupta, E.P. Paschalis, P. Roschger (2004) - Structure and mechanical quality of the collagen-mineral nano-composite in bone. *Journal of Materials Chemistry* 14, (14):2115-2123.

Glimcher, M.J. (2006) - Bone: nature of the calcium phosphate crystals and cellular, structural, and physical chemical mechanisms in their formation. *Reviews in Mineralogy & Geochemistry* 64, 223-282.

Harris E.C. (1979) – Principles of Archaeological Stratigraphy. Academic press, London.

Hillman J.R., R.W. Davis, Y.Z. Abdelbaki (1973) – Cyclic bone remodelling in deer. *Calcified Tissue Research* 12, 323-330.

Landis W.J. (1996) - Mineral characterization in calcifying tissues: Atomic, molecular and macromolecular perspectives. *Connective Tissue Research* 35, (1-4):1-8.

Pan Y., M.E. Fleet (2002) - Compositions of the apatite-group minerals: substitution mechanisms and controlling factors, in: M.J. Kohn, J. Rakovan, J.M. Hughes (Eds.), Phosphates: Geochemical, Geobiological and Material Importance, Reviews in Mineralogy and Geochemistry, vol. 48, Mineralogical Society of America, Washington, DC, 2002, pp. 13–50.

Piccoli P.M. & P.A. Candela (2002) - Apatite in igneous systems, in: M.J. Kohn, J. Rakovan, J.M. Hughes (Eds.), Phosphates: Geochemical, Geobiological and Material Importance, Reviews in Mineralogy and Geochemistry, vol. 48, Mineralogical Society of America, Washington, DC, pp. 255–292.

Surovell T.A. & M.C. Stiner (2001) - Standardizing infra-red measures of bone mineral crystallinity: An experimental approach. *Journal of Archaeological Science* 28, (6):633-642.

Teitelbaum S.L. (2000) - Bone resorption by osteoclasts. *Science* 289, (5484):1504-1508.

Van Oers R.F.M., R. Ruimerman, E. Tanck, P.A.J. Hilbers, R. Huiskes (2008) - A unified theory for osteonal and hemi-osteonal remodeling. *Bone* 42, (2):250-259.

Weiner S. & W. Traub (1992) - Bone-Structure - from Angstroms to Microns. *Faseb Journal* 6, (3):879-885.

Weiner S. & H.D. Wagner (1998) - The material bone: Structure mechanical function relations. *Annual Review of Materials Science* 28, 271-298.

Wopenka B. & J.D. Pasteris (2005) - A mineralogical perspective on the apatite in bone. *Materials Science & Engineering C-Biomimetic and Supramolecular Systems* 25, (2):131-143.

Wright L.E. & H.P. Schwarcz (1996) - Infrared and isotopic evidence for diagenesis of bone apatite at Dos Pilas, Guatemala: palaeodietary implications. *Journal of Archaeological Science* 23, 933-944.

Chapter 3 - Isotopes, Climate & Deer bones

The aim of this chapter is to delineate the conceptual framework of deer bone utilization as a climatic proxy, and more specifically as an aridity indicator. The first part is extensively dedicated to the variation of rain water isotopic composition, in the tropics and in the Yucatán peninsula in particular. The isotopic composition of plant's tissues in relation with water source and its modulation by climatic fluctuations will be approached in the second part. The third part finally links together rain water, plants and deer bone isotopic compositions. The expected effects of droughts in the Maya region on deer bone isotopic composition are ultimately detailed in the final part.

3.1) Oxygen isotopes in water

Oxygen naturally occurs on Earth in three stable isotopic forms (^{16}O, ^{17}O and ^{18}O), each with a nucleus including 8 protons, but with different numbers of neutrons (8, 9 and 10, respectively). Their average proportions are 99.762% (^{16}O), 0.200% (^{18}O) and 0.038% (^{17}O; IAEA, 2009).

The abundance of the heavy oxygen isotope relatively to the light one ($^{18}O/^{16}O$) in ocean waters is close to 2.01×10^{-9} (Baertschi, 1976). The ocean, being the largest relatively homogeneous water reservoir and the source of nearly all the water molecules forming precipitation, was chosen as the reference standard (SMOW: Standard Mean Ocean Water) for the $\delta^{18}O$-scale of oxygen isotopes in water samples (Craig, 1961). The oxygen isotopic ratio $\delta^{18}O$ (in ‰) of a water sample is now defined as:

$$\delta^{18}O = \left(\frac{\left(\frac{^{18}O}{^{16}O}\right)_{sample}}{\left(\frac{^{18}O}{^{16}O}\right)_{VSMOW}} - 1 \right) \times 1000 \qquad \textbf{[Eq. 3.1]}$$

where VSMOW stands for Vienna-SMOW, the standard used today, distributed by the International Atomic Energy Agency (IAEA), based in Vienna.

Positive $\delta^{18}O$ values will thus signify an enrichment of the water sample in the heavy isotopic species relative to the standard, while negative $\delta^{18}O$ values indicate a relative depletion in ^{18}O.

3.1.1) ^{18}O fractionation of during evaporation

The difference in the number of neutrons causes two distinct isotope processes during water evaporation:

(1) *A thermodynamic (equilibrium) fractionation effect.* This partitioning of the isotopic species between the liquid and vapour phases is due to quantum mechanical effects, governed by the vibrational frequencies of theses species. Quantum mechanics model stipulates that the potential energy of vibration of heavy water molecule ($H_2{}^{18}O$) is lower (more negative) than the light one ($H_2{}^{16}O$). As a consequence, in liquid water, $H_2{}^{18}O$ molecules require more energy to release themselves from the attraction of other water molecules and escape to the atmosphere (*i.e.* to vaporize) than $H_2{}^{16}O$, so $H_2{}^{16}O$ molecules evaporate slightly more readily than $H_2{}^{18}O$. The oxygen equilibrium (thermodynamic) fractionation factor of vaporization ($^{18}\alpha_{L/V}$) is strictly temperature-dependant (see the example of a closed air-water system presented in Appendix 3.A, and for further details and references).

(2) *A kinetic (non-equilibrium) fractionation effect.* The ^{18}O atoms being heavier than ^{16}O atoms (by about 3.34×10^{-30} g or by ~12.5 %), heavy water molecule $H_2{}^{18}O$ is also heavier than light water molecule $H_2{}^{16}O$. In water vapour, the kinetic energy (~mobility) of heavy water molecule is then lower (kinetic theory of gases), so the rate of evaporation of $H_2{}^{16}O$ is faster than the one of $H_2{}^{18}O$. At Earth's surface, thermodynamic equilibrium is never reached because of atmospheric circulation: before reaching the saturation vapour pressure, air masses are moving and remain unsaturated, so kinetic fractionation effects have to be taken into account. The model commonly used to describe the isotopic fractionation of ^{18}O during evaporation of water into a turbulent

unsaturated atmosphere is based on the model formulated first by Craig & Gordon (1965), detailed in Appendix 3.B.

As a consequence of those two effects, while a water surface is evaporating, the water vapour will tend to be depleted in $H_2{}^{18}O$ molecules (lower $\delta^{18}O$), while the remaining liquid water will tend to be enriched in $H_2{}^{18}O$ (higher $\delta^{18}O$). The extent of the enrichment [depletion] in heavy isotopes of the liquid water [water vapour] is strongly depending on temperature at which evaporation occurs, and to a lesser extent, to the movements of air masses above the evaporative surface.

3.1.2) Oxygen isotopic composition of rain water

When water vapour condenses to form rain, the reverse phenomenon of heavy oxygen fractionation during evaporation occurs: the heavier $H_2{}^{18}O$ water molecules will tend to precipitate slightly more readily, leading to a relative enrichment of rain water relatively to its vapour source.

Early studies on the isotopic composition of precipitation were made by Dansgaard (1953), Epstein & Mayeda (1953) and Friedman *et al.* (1962). Later, the International Atomic Energy Agency, in collaboration with the World Meteorological Organization (IAEA/WMO), established the Global Network of Isotopes in Precipitation (GNIP), a world-wide selection of meteorological stations at which samples are collected to monitor the $\delta^{18}O$ composition of precipitation. Several studies derived from the collected datasets (e.g.: Dansgaard, 1964; Bowen, 1991; Rozanski *et al.*, 1992) have shown that the oxygen isotopic composition of precipitation ($\delta^{18}O_{Rain}$) is controlled by several factors including:

(1) *The temperature effect.* To a good approximation, the depletion in heavy oxygen in precipitation correlates well with the near-ground temperature, as shown by Dansgaard (1964) and Yurtsever (1975), or more precisely with the temperature at the cloud base (Rindsberger & Magaritz,1983). Outside the tropics, the temperature is the main factor affecting $\delta^{18}O_{Rain}$: this dependence is clearly seen on figure 3-1, presenting the modelling of $\delta^{18}O_{Rain}$ as a function of

annual surface air temperature, as established from the worldwide dataset of GNIP. On this figure, the annual surface temperature range can also be considered as the gradient of average temperatures from the equator to higher latitudes (the poles are not included, due to different fractionation processes occurring during solid precipitation). The curve is not strictly a straight line, given that the temperature dependence of the latitude effect ranges from ~ +0.8 ‰ per 1°C increase at 0°C to ~ +0.5 ‰ per 1°C increase at 20°C (Gat, 2000).

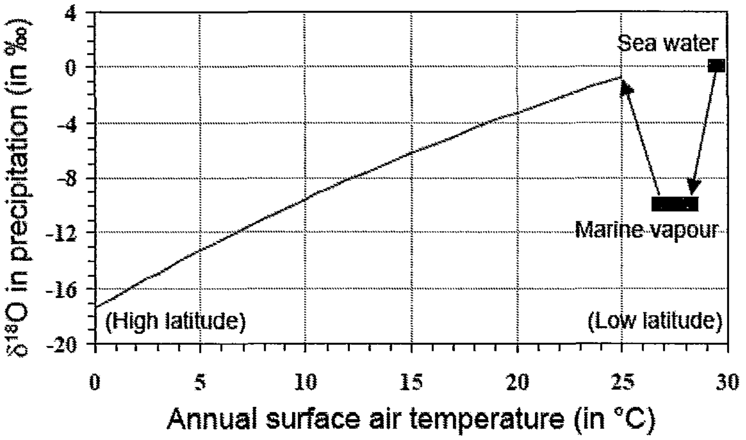

Figure 3-1. Schematic representation of the temperature-dependence of the latitude effect, according to a simplified model established from the GNIP database. The fractionation of sea water $\delta^{18}O$ (considered to be 0 ‰) during evaporation at the tropics (fractionation factor of 10 ‰) is indicated in the right part. The subsequent condensation of moisture carried towards higher latitude (thus lower temperatures) is progressively decreasing the $\delta^{18}O_{Rain}$. After Gat (2000).

(2) *The source the water is derived from.* As stated in Chapter 1 (part 1.2.1), the Maya region is fed with moisture picked up over the Caribbean Sea, derived from ocean whose isotopic composition is close to 0 ‰, but due to the high evaporation rates occurring in the tropics, surface waters in the Caribbean sea are probably slightly ^{18}O-enriched ($\delta^{18}O > 0$ ‰).

(3) *The fraction of moisture remaining in the precipitating air mass.* Within the cloud, equilibrium fractionation between vapour and the condensing phases preferentially partitions ^{18}O into the rain. Along the trajectory of the air mass, the process of "rain-out" distils the heavy isotopes from the vapour: isotopically enriched rain is forming and the residual vapour then becomes progressively depleted in ^{18}O according to a Rayleigh–type distillation. Subsequent precipitation, while enriched with respect to the remaining vapour, will be depleted with respect to the earlier one from the same vapour mass. Rayleigh distillation results in two coupled isotope effects: the more intense the precipitation is (*amount effect*) or the further the vapour source is (*continental effect*), the more isotopically-depleted the precipitation will be (*i.e.* the lower $\delta^{18}O_{Rain}$ will be; e.g.: Dansgaard, 1964; Merlivat & Jouzel, 1979; Gat, 1996). In Belize and northern

Guatemala, a recent study has shown that (1) the *amount effect* provokes a decrease of $\delta^{18}O_{Rain}$ values by ~1.2‰ per 100 mm increase of monthly average rainfall, and (2) the *continental effect* is of ~0.7‰ decrease in $\delta^{18}O_{Rain}$ per 100 km distance from the Carribean coast, once corrected for altitude effects (Lachniet & Patterson, 2009).

(4) *The altitude effect.* Rain is produced through the cooling of a vapour mass. Cooling occurs by adiabatic expansion as warm air rises to lower pressures, or by radiative heat loss. When the dew point is passed (when air is at the temperature at which vapour pressure ρ has reached ρ_{SAT}, *i.e.* when relative humidity is 100%), water vapour starts to condense and rain occurs. The *altitude effect* is the direct consequence of a greater oxygen fractionation factor that occurs at higher altitude (thus lower temperature): when air masses are orographically uplifted, the subsequent cooling precipitates preferentially the heavier isotopes so that, as the cloud is progressively depeleted in these isotopes, higher altitude precipitation will exhibit lower $\delta^{18}O$ values. In Belize and northern Guatemala, the altitude effect has been estimated as ~0.2 ‰ decrease in $\delta^{18}O$ per 100 m increase in altitude (Lachniet & Patterson, 2009).

(5) *The amount of evaporation that occurs as rain falls through the atmosphere.* Unlike fractionation of heavy oxygen during evaporation (being a non-equilibrium process; see part 3.1.1 above), the ^{18}O fractionation during the condensation of water vapour to form clouds and precipitation takes place in an intimate mixture of vapour and water droplets where relative humidity is 100% (*i.e.* saturation in vapour pressure). Here, equilibrium fractionation between vapour and water dominates although some in-cloud processes, as well as possible re-evaporation of falling rain (especially in the tropics), play a role in determining the $\delta^{18}O$ composition of precipitation. The lower diffusive exchange of heavy isotopes in water vapour (see Appendix 3.B, part 3.B.2) causes rain to reduce isotope ratios both in and downwind from regions where precipitation occurs, in zones of decreased relative humidity (Lawrence *et al.*, 2004).

In the end, the fractionation occurring during evaporation and condensation are responsible for the much larger spatial and temporal variations in rain and water vapour $\delta^{18}O$ than the ocean water they derive from (Craig & Gordon, 1965). The isotopic composition of precipitation and water vapour therefore reflect changes in climate and atmospheric circulation regimes (Dansgaard, 1964; Lawrence *et al.*, 2004).

3.1.3) $\delta^{18}O_{Rain}$ fluctuations in the Maya region

Available data of isotopic measurements of rain water in the region are scarce: only two weather stations (Veracruz in Mexico and Ilopango in El Salvador, figure 3-2) from the GNIP have recorded the $\delta^{18}O_{Rain}$ on a regular monthly basis for more than 20 years (from 1969 to 1984 at Ilopango and from 1962 to 1989 at Veracruz; n=95 and n=130, respectively).

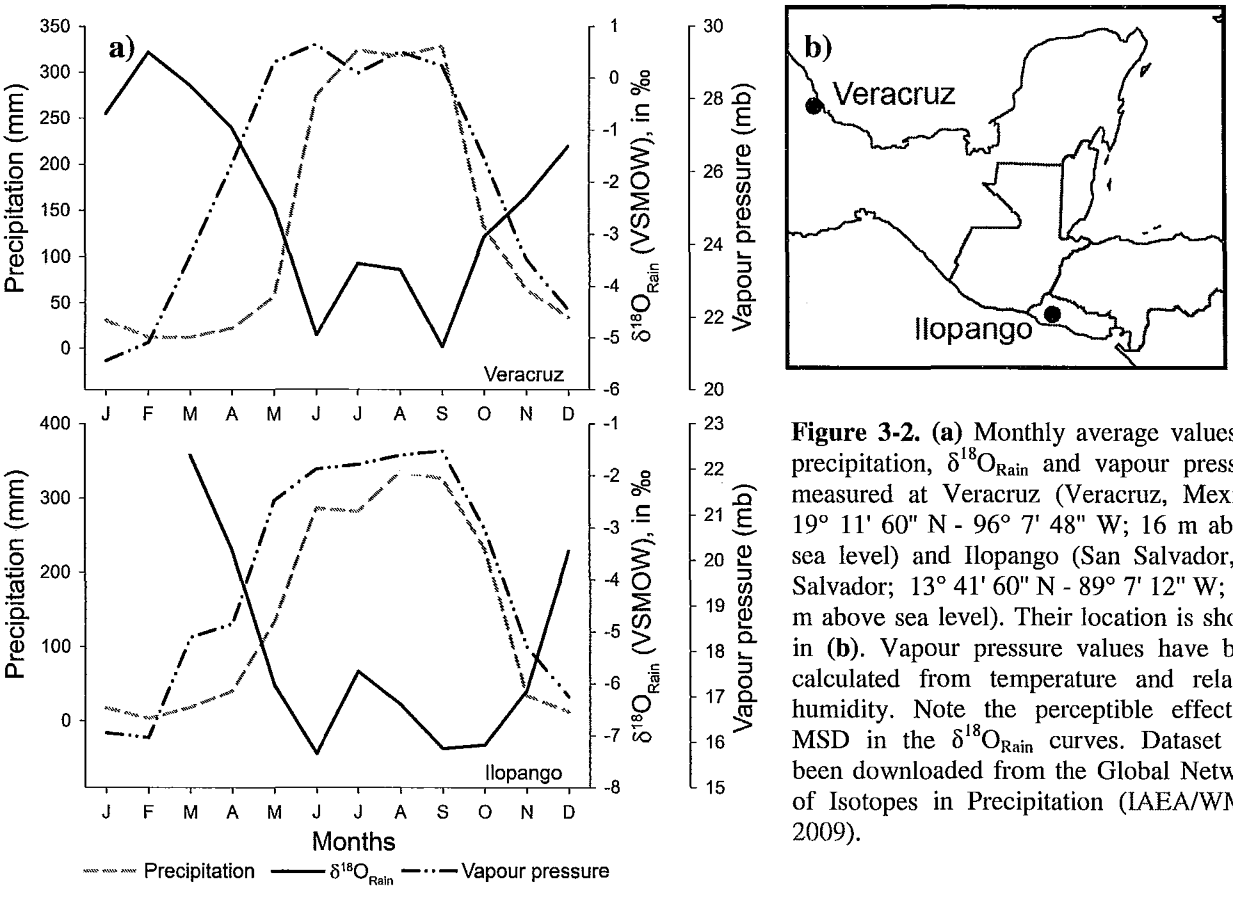

Figure 3-2. (**a**) Monthly average values of precipitation, $\delta^{18}O_{Rain}$ and vapour pressure measured at Veracruz (Veracruz, Mexico; 19° 11' 60" N - 96° 7' 48" W; 16 m above sea level) and Ilopango (San Salvador, El Salvador; 13° 41' 60" N - 89° 7' 12" W; 615 m above sea level). Their location is shown in (**b**). Vapour pressure values have been calculated from temperature and relative humidity. Note the perceptible effect of MSD in the $\delta^{18}O_{Rain}$ curves. Dataset has been downloaded from the Global Network of Isotopes in Precipitation (IAEA/WMO, 2009).

As shown by figure 3-2, the highest values of $\delta^{18}O_{Rain}$ are seen during the winter (February), when the ITCZ is moving southwards, away from the Yucatán peninsula, associated with reduced amounts of rainfall and low vapour pressure (refer to Chapter 1, figure 1-3; Haug *et al.*, 2003). Conversely, lowest $\delta^{18}O_{Rain}$ values are seen during summer (September), when the

ITCZ lies precisely on the peninsula, providing heavy rainfall, in relation with high vapour pressure, as expected.

However, the major difference between the two sites is their location: Ilopango is on the Pacific coast of El Salvador (615 m above sea level), while Veracruz is located on the coast of the Gulf of Mexico (16 m asl). Even though the two cities are relatively close to each other, they are fed with rain from different origins, due to the presence of the Sierra Madre de Chiapas, preventing moisture from the Pacific from entering the peninsula (refer to Chapter 1, figure 1-2). Consequently, the rain falling at Ilopango is about 2 ‰ lighter than at Veracruz, at any moment of the year, this difference being approximately 1 ‰ higher than the one due to the *altitude effect* only (see part 3.1.2 above).

In the tropics, it is considered that the low monthly and annual thermal amplitudes make negligible the effect of air temperature variations on local $\delta^{18}O_{Rain}$. This is particularly the case at Ilopango, where annual thermal amplitude is very low (temperatures range from 22 to 24.5°C; figure 3-3): there, no correlation is found between $\delta^{18}O_{Rain}$ and temperature monthly averages (linear correlation coefficient r^2 close to 0; figure 3-3). At Veracruz, annual thermal amplitude is higher (temperatures range from 21.5 to 28°C) and monthly average $\delta^{18}O_{Rain}$ seems to be correlated to corresponding temperatures (r^2=0.72; figure 3-3), but the latter is also following the same pattern as precipitation amount (r^2=0.59, not shown). In the end, it can be seen that monthly averages of $\delta^{18}O_{Rain}$ are best correlated to precipitation amounts in both sites (r^2=0.60 at Ilopango; r^2=0.79 at Veracruz; figure 3-3).

The annual fluctuation patterns of temperature, vapour pressure and precipitation at the three sites should be comparable to those occurring at Veracruz and Flores (see Chapter 1, part 1.4). We can thus combine the climatic database at Flores to the one of Veracruz, to obtain reliable indicators of climatic conditions occurring at the three sites, as well as $\delta^{18}O_{Rain}$, if some factors are accounted for:

(1) *Seasonality.* Similarly to Veracruz, a difference of ~6 ‰ between winter and summer monthly average $\delta^{18}O_{Rain}$ values is expected because of the strong wet/dry seasonality (figure 3-2).

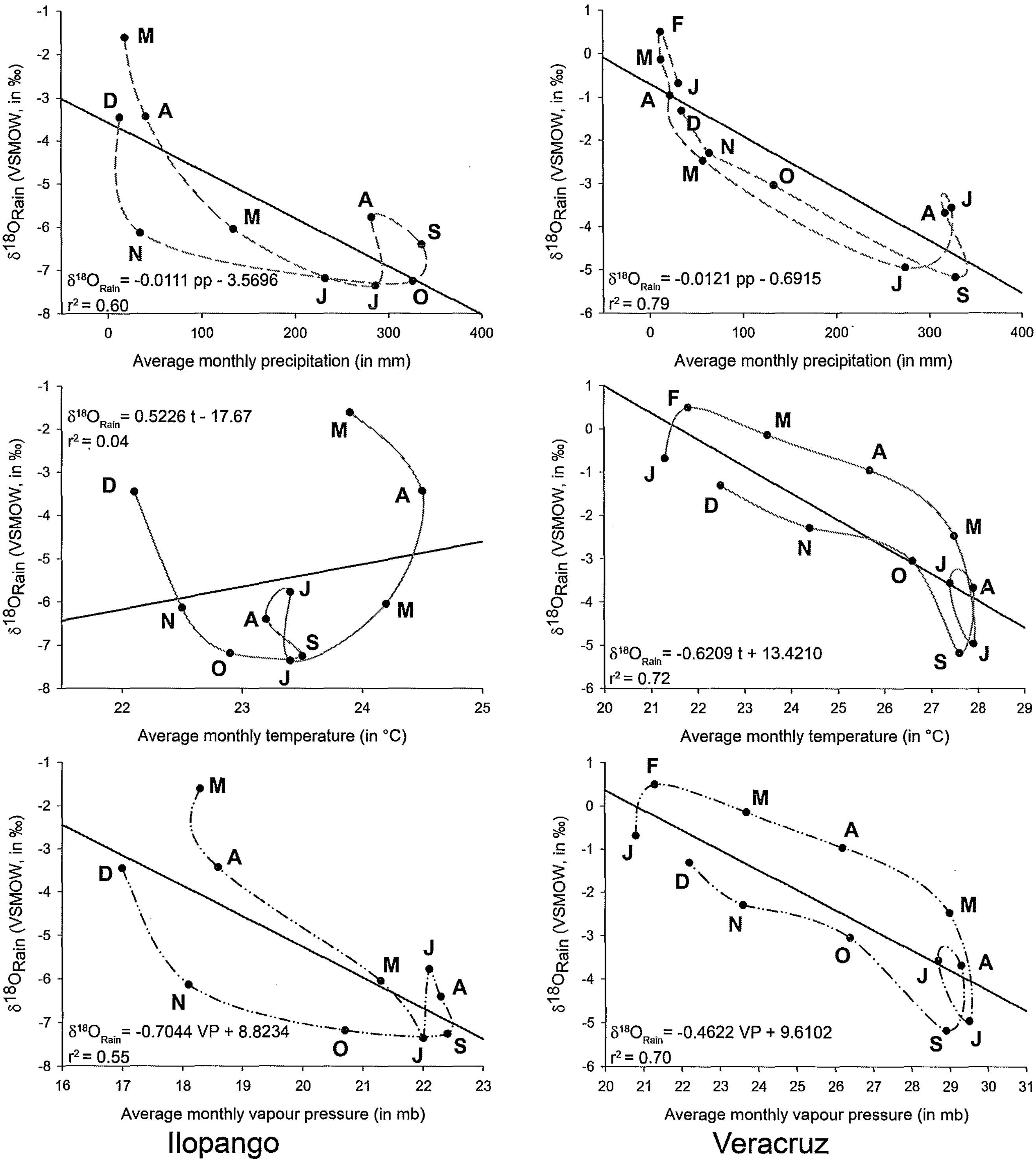

Figure 3-3. Monthly averages $\delta^{18}O_{Rain}$ measured at Ilopango (left) and Veracruz (right), plotted as functions of monthly averages of precipitation (top), temperature (middle) and vapour pressure (bottom). Linear correlations are shown, as well as corresponding equations and correlation coefficients r^2. Note that because of the absence of precipitation at Ilopango in January and February, no $\delta^{18}O_{Rain}$ value is available during those two months. Dataset has been downloaded from the GNIP (IAEA/WMO, 2009).

(2) *Amount effect.* In terms of average annual precipitation, a gradient exists from Lamanai (less than 2,000 $mm.yr^{-1}$) to Motul de San José (more than 2,000 $mm.yr^{-1}$) and Piedras Negras (close to 3,000 $mm.yr^{-1}$; refer to Chapter 1, figure 1-4). This difference can be related to an average difference in monthly rainfall of ~100 mm between PN and MSJ (slightly less compared to LAM), so that average $\delta^{18}O_{Rain}$ at PN is expected to be ~1.2‰ lower than at MSJ (or slightly lower compared to LAM), based on estimates from Lachniet & Patterson (2009).

(3) *Temperature effect.* The inter-sites temperature differences are considered as negligible. Vapour pressures are thus considered to co-vary with precipitation patterns, preceding them by about a month (figure 3-2; refer also to Chapter 1, figures 1-6 and 1-7).

(4) *Altitude effect.* Between MSJ and PN, we consider the altitude effect negligible, given the low difference of elevation of the two sites (both of them are ~200 m asl), but LAM is ~20 asl, so that $\delta^{18}O_{Rain}$ values at LAM will have to be corrected (by +0.4‰) to allow the comparison between the three sites (Lachniet & Patterson, 2009).

(5) *Continental effect.* As stated earlier, the three sites are fed with moisture from the Caribbean basin carried by easterly trade winds (refer to Chapter 1, figure 1-2 and part 1.4). Along a line parallel to the equator, MSJ is ~150 km from LAM, and PN is also ~150 km from MSJ, so that average $\delta^{18}O_{Rain}$ values at PN will tend to be ~1 ‰ lower than at MSJ, being itself ~1 % lower than at LAM.

(6) *Shadow effect.* Given the direction of prevailing easterly trade winds, no effect of rain shadow is expected on the northern slope of the Sierra Madre de Chiapas. Actually, this effect is clearly seen on the Pacific slope of the cordillera (Lachniet & Patterson, 2009), proving that more than just blocked by the cordillera, the Pacific air masses are pushed away south from the peninsula by the easterlies.

In the end, the following equation, giving monthly averages of $\delta^{18}O_{Rain}$ as a function of monthly average precipitation amount at Veracruz (see upper right graph in figure 3-3) can be applied to the Flores dataset:

$$\delta^{18}O_{Rain} = -0.0121\,pp - 0.6915 \qquad (r^2=0.79) \qquad \textbf{[Eq 3.2]}$$

Using monthly average precipitation amounts at Flores, equation [3.2] gives decrease of approximately 1 to 2 ‰ of the yearly average $\delta^{18}O_{Rain}$ between the driest years (e.g.: 1994, 1998) and the wettest years (e.g.: 2000, 2006; table 3-1; refer also to Chapter 1, figures 1-6 and 1-7), depending on precipitation distribution through the year (*i.e.* depending on the strength of the *amount effect*).

Table 3-1. Estimated yearly averages $\delta^{18}O_{Rain}$ in relation with average climatic conditions that have occurred at Flores (~MSJ) during relatively dry (1994 and 1998) and wet years (1997 and 2006), and corresponding $\delta^{18}O_{Rain}$ expected at PN and LAM.

Year	Total precipitation at Flores (in mm)^a	Expected yearly average $\delta^{18}O_{Rain}$ at Flores (in ‰)^b	Estimated yearly average $\delta^{18}O_{Rain}$ at Piedras Negras (in ‰)^c	Estimated yearly average $\delta^{18}O_{Rain}$ at Lamanai (in ‰)^c
1994	1,160	-1.9	-3.4	-0.9
1998	1,456	-1.6	-3.1	-0.6
1997	1,600	-2.3	-3.8	-1.3
2006	2,395^d	-3.6	-5.1	-2.6

a: available in Flores climatic dataset (INSIVUMEH, 2009); b: using eq. [3.2]; c: using estimates given by Lachniet & Patterson (2009); d: November 2006 values missing and were not taken into account

Ultimately, as for the inter-site comparison, considering the effects described above, a gradient of yearly averages of $\delta^{18}O_{Rain}$ values is expected from Lamanai to Piedras Negras, through Motul de San José. It is then considered that $\delta^{18}O_{Rain}$ values at MSJ will be on average ~1‰ lower compared to LAM (as a result of the *altitude effect*, and disregarding the *amount effect* difference between the two sites) and that $\delta^{18}O_{Rain}$ values at PN will be on average ~1.5 ‰ lower compared to MSJ (table 3-1).

3.2) Plant isotopic composition

Leaf water and atmospheric carbon dioxide (CO_2) being the substrate for all terrestrial photosynthesis, the resulting organic matter is the base of all terrestrial food chains. For this reason, carbon and oxygen isotopic composition of plant tissues have been studied extensively.

The following part focuses on two aspects: the mechanisms of leaf water $\delta^{18}O$ enrichment in relation with changes in humidity, and the carbon isotopic composition of plant's organic matter.

3.2.1) Oxygen isotopic composition of leaf water

No fractionation of oxygen is observed in terrestrial plants during water uptake and transport of crude sap in xylem: the isotopic composition of the water entering the leaves is equal to the one of the soil water ($\delta^{18}O_{SW}$; e.g.: Landais *et al.*, 2006; Barbour, 2007).

$\delta^{18}O_{SW}$ may vary considerably from that of $\delta^{18}O_{Rain}$, itself strongly dependant on several effects described earlier. $\delta^{18}O_{SW}$ can be strongly influenced by the coupled effects of relative humidity and temperature, regulating direct evaporation from the soil surface (the latter leading to a gradient of $\delta^{18}O_{SW}$ relative to the depth), but also by frequency of precipitation events, the loss by plant water uptake, and in some cases with uptake of groundwater isotopically distinct from surface water (Barbour, 2007). As a result of the gradient with depth, $\delta^{18}O$ of stem water (which ends up in leaves) can also vary somewhat depending the depth of the root system (Webb & Longstaffe, 2006).

The oxygen-isotope composition of leaf water ($\delta^{18}O_{LW}$) remains unchanged from that of soil water until affected by loss of water via transpiration in the leaves, resulting in a ^{18}O-enrichment of the residual leaf water (Barbour *et al.*, 2004; Webb & Longstaffe, 2006). The mechanisms of oxygen fractionation during leaf transpiration are similar to those occurring during water evaporation (described in part 3.1.1 above and Appendix 3.B), with slight modifications. The adaptation of Craig-Gordon model to leaf water evaporation includes specific features such as the resistance of stomatal closure to evaporation or leaf surface temperature (further details and references are given in Appendix 3.C).

In the present study, we will assume that the overall processes of $^{18}O_{LW}$-enrichment are mainly driven by the humidity gradient between the inside of the leaf and the surrounding air (e.g.: Farquhar *et al.*, 2007), as clearly shown in figure 3-4). In other words, the rate of water loss of a plant by evaporation is higher when subjected to dry air (resulting in higher $^{18}O_{LW}$

enrichment) than when subjected to moist air. This difference of $\delta^{18}O_{LW}$ can be as high as 20‰ (figure 3-4), as experimentally shown. On average, it can be considered that a 10 % decrease in relative humidity will result in a ~3 ‰ increase of $\delta^{18}O_{LW}$.

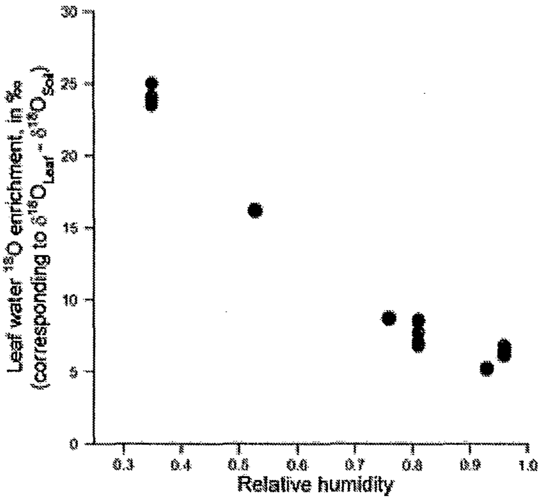

Figure 3-4. Enrichment of leaf water versus relative humidity in five C_3 grass species. All grasses were grown in chambers where the isotope ratio of source water was held constant, and only relative humidity varied across treatments. Note that relative humidity was calculated based on leaf temperature. After Farquhar *et al.* (2007).

In conclusion, the oxygen isotopic composition of leaf water depends on (1) the source the water is coming from (*i.e.* to $\delta^{18}O_{Rain}$ in most cases), and (2) air vapour pressure (~relative humidity), the latter modulating soil water evaporation and leaf transpiration. During dry conditions, frequent in the Maya region (see Chapter 1), those two factors are acting in the same direction, resulting in higher $\delta^{18}O_{LW}$.

3.2.2) Carbon isotopic composition of organic matter

Carbon naturally occurs on Earth under two stable isotopic forms (^{12}C and ^{13}C), each with a nucleus including 6 protons, with 6 (^{12}C) or 7 (^{13}C) neutrons. Their average proportions are ~98.9% (^{12}C) and ~1.1% (^{13}C) (IAEA, 2009).

Carbon isotopic compositions ($\delta^{13}C$) are generally given relatively to the V-PDB (Vienna-Pee Dee Belemnite), the international standard related to limestone from the PeeDee Formation in South Carolina (derived from the Cretaceous marine fossil *Belemnitella americana*). The abundance of the heavy carbon isotope relative to the light one in PDB limestone ($^{13}C/^{12}C$) is close to 1.12×10^{-2} (IAEA, 2009).

As in the case of oxygen isotopes, the mass difference between ^{13}C and ^{12}C atoms induces a fractionation during chemical reactions. The two main photosynthetic C3 and C4 pathways of terrestrial plants thus create distinct carbon-isotope signatures during atmospheric carbon dioxide (CO_2) fixation. The organic matter photosynthesized in C3 plants (representing ~90% of terrestrial plants; e.g.: trees, shrubs, wheat) is depleted by ~18.5 ‰ relatively to atmospheric CO_2, whereas in the case of C4 metabolism (e.g.: maize, crabgrass, sugarcane, sorghum), the spatial dissociation of dark and light phases of photosynthesis in the leaf leads to a lower fractionation of atmospheric CO_2 during organic matter synthesis (of ~4.5 ‰; those processes are reviewed in Farquhar *et al.*, 1989). Unlike the highly variable oxygen isotopic composition of leaf water, the carbon isotopic composition of plant organic matter ($\delta^{13}C_{POM}$) is then quite stable, so that terrestrial plants can be divided in two pretty well-defined isotopically-distinct groups, according to their photosynthetic pathways (figure 3-5; e.g.: Van Der Merwe & Medina, 1991).

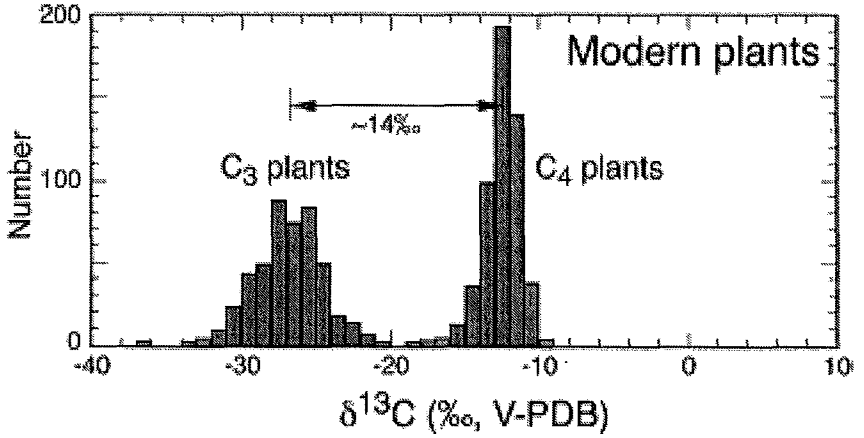

Figure 3-5. Histogram of $\delta^{13}C_{POM}$ of modern plants (*i.e.* in modern, industrial era). C3 plants have an average isotope composition of approximately -26 ‰, whereas C4 plants cluster ~14‰ higher at ~-12‰

From Kohn & Cerling (2002).

In addition to metabolic type, $\delta^{13}C_{POM}$ can also be affected by environmental conditions. Two of them are described below:

(1) *The canopy effect.* In dense forests (as found in Petén region), high rate of litter decomposition by bacteria (Vogel, 1978), as well as the presence of numerous aerial roots (Medina *et al.*, 1980) are provoking a gradient of $\delta^{13}C$ in the surrounding atmospheric CO_2, from

the ground to the canopy (more negative values are seen on the ground). Plants (or their organs) close to the ground are thus subjected to ^{13}C-depleted atmosphere, compared to those close to the canopy: in Amazonia one of the densest rain forest on Earth, the difference in $\delta^{13}C_{POM}$ can be as high as 6 ‰ (Vogel, 1978; Medina & Minchin, 1980). It has also been suggested that lower light availability near the ground in dense forest could partly explain the observed gradient of $\delta^{13}C_{POM}$, by increasing the ^{13}C-discrimination during photosynthesis, but in the end, the intensity of the *canopy effect* is clearly correlated to the density of the forest (Van der Merwe & Medina, 1991).

(2) *Water stress*. It has also been established that water stress impacts the $\delta^{13}C_{POM}$ of C3 plants, provoking organic matter enrichment in heavy carbon. The stomata closure, as a response to dry conditions, progressively reduces the internal leaf CO_2 concentration, the later lowering isotopic discrimination against ^{13}C in C3 plants (this strategy allows higher water use efficiency; e.g.: Farquhar & Richards, 1984). In agricultural species (wheat), $\delta^{13}C_{POM}$ enrichment due to water stress has been shown to range between 2 and 4 ‰ (Johnson *et al.*, 1989; Tieszen, 1991). As for C4 plants, water stress also reduce significantly $\delta^{13}C_{POM}$ by an average 0.5 ‰ (Ghannoum *et al.*, 2002), but unlike C3 plants, the magnitude of $\delta^{13}C_{POM}$ change during water stress seems to be strongly species-dependant (Fravolini *et al.*, 2002).

3.3) Deer bioapatite isotopic composition

White-tailed deer is a non-migrating browser, widely distributed throughout North and Central America (Cormie *et al.*, 1994). It is also a forage concentrator and opportunistic edge browser, subsisting almost entirely on energy-rich leafy forbs or C3 dicotyledonae (e.g.: shrubs, wheat) and rejecting fibrous tropical C4 plants (e.g.: crabgrass, sorghum), unless driven to starvation (Brown, 1994; Harlow & Guynn, 1994; Kroll, 1994; Bello *et al.*, 2001).

White-tailed deer has the ability to thrive in semi-arid regions because of its low drinking water requirements, since its water needs can be mostly satisfied by the water contained in the plants ingested (*i.e.* by leaf water). For example, a precise inventory of Mexican white-tailed deer's diet has been conducted in the Mixteca region (Southern Puebla State, at ~200 km south-west of Veracruz), in a region where almost no surface water is available during the dry season (Villarreal & Marín, 2005). This study reveals that to subsist, white-tailed deer selects fruits (e.g: *Ficus* sp.), flowers (e.g.: *Ceiba parvifolia*) and leafs (e.g.: *Opuntia* sp.) containing high humidity proportions (generally between 65 and 90 wt.%). Those plants generally have shallow root systems that directly absorb rainwater, without depending on groundwater (Cormie *et al.*, 1994).

However, the quantification of drinking water requirements is difficult: the factors influencing diet selection, habitat distribution and watering frequency are numerous, including the season, the reproductive stage, the vegetation distribution, the presence of sympatric species or surface water availability (Hervert & Krausman, 1986; Lautier *et al.*, 1988; Bello *et al.*, 2001). For example, in their experiment, Lautier *et al.* (1988) gave water *ad libitum* to 9 pen-raised male white-tailed deers, ranging in age from 1.5 to 3.5 years: the mean daily intake has been evaluated to be ~3.6 L ± 0.24 L, but values were ranging from 1.4 to 13.5 L. Further aspects of drinking water requirements of white-tailed deer in the Maya region will be approached later (Chapter 6).

3.3.1) Oxygen isotopic composition

Several studies on modern mammals have shown that, in the case of oxygen, there is an isotopic equilibrium between mineralised tissues (bones and teeth) and body water (e.g.: Longinelli, 1984; Luz *et al.*, 1984; Fricke & O'Neil, 1996), this balance being species-specific (e.g.: Bryant & Froelich, 1995; Fricke & O'Neil, 1996).

The oxygen present in mammal's body water comes from three possible sources: the drinking water, the atmospheric oxygen and the oxygen present in the food (Luz *et al.*, 1990). When species-specific relations are known, mammalian homeothermy allows the direct reconstitution of these parameters from the isotopic ratio of oxygen measured on mineralised tissues, for animals weighing more than 1 Kg (Bryant *et al.*, 1996; Kohn, 1996).

As a consequence of its low drinking water requirements, it has been established that the major source of oxygen of deer body water (and ultimately bioapatite phosphate and carbonate-bounded oxygen) is the water contained in the leaves ingested by the animal (Luz *et al.*, 1990;

Cormie *et al.*, 1994). The oxygen isotopic composition ($\delta^{18}O$) measured on both bioapatite carbonate groups ($\delta^{18}O_C$) and phosphate groups ($\delta^{18}O_P$) is thus reflecting the one of ingested leaf water ($\delta^{18}O_{LW}$).

3.3.2) Carbon isotopic composition

Substitutional carbonate groups in bioapatite are derived from dissolved inorganic carbon (DIC) in blood (carbon dioxide CO_2, carbonic acid H_2CO_3, bicarbonate HCO_3^- and carbonate CO_3^{2-}; Passey *et al.*, 2005), itself derived from the oxidation of dietary carbon (Lee-Thorp & Sponheimer, 2005).

The total fractionation among DIC and carbonate mineral in thermodynamic equilibrium, at mammal body temperature, is expected to lead to enrichment in $\delta^{13}C$ of the mineral of about 10‰, which is matched by isotopic differences of ~10-14‰ observed between dietary carbon and bioapatite carbonate among mammals (Lee-Thorp *et al.*, 1989; Cerling & Harris, 1999; Lee-Thorp & Sponheimer, 2005). Several controlled feeding experiments on herbivorous mammals have shown that the shift of $\delta^{13}C$ values measured on bones and teeth from the expected equilibrium is species-dependant and is related to differences in digestive physiology, mainly because of CO_2 and methane production by the intestinal flora (e.g. Sullivan & Krueger, 1981; Cerling & Harris, 1999; Ambrose & Krigbaum, 2003).

Even if the relationship between the diet and bioapatite carbonate (known as the trophic shift, often referred as $\Delta^{13}C$, where $\Delta^{13}C = \delta^{13}C_{Bone} - \delta^{13}C_{Diet}$) is complex and still not fully understood (Jim *et al.*, 2004), field estimates and lab experiments have demonstrated that herbivore bioapatite provides a robust monitor of the $\delta^{13}C$ of vegetation. Because "you are what you eat" (Kohn, 1999; figure 3-6), $\delta^{13}C$ studies in herbivorous mammal bioapatite have enjoyed extensive application in a variety of paleodietary studies, and especially C3 *versus* C4 consumption (e.g. MacFadden & Cerling 1996; Koch *et al.*, 1998; Bocherens *et al.*, 2001).

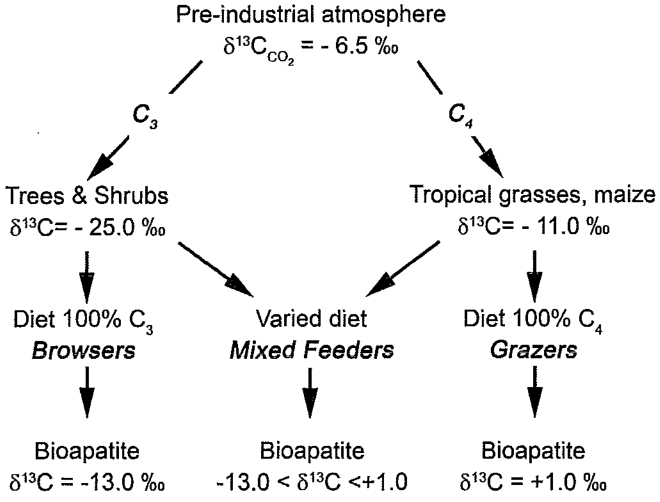

Figure 3-6. Variation of $\delta^{13}C_{POM}$, according to the two main types of photosynthesis pathways (C_3 and C_4) and the $\delta^{13}C$ of source CO_2. $\delta^{13}C_{Bone}$ in relation to the diet among herbivorous mammals is also represented. Values are given in ‰, relatively to V-PDB. After Lee-Thorp (2002).

In the end, as any change in diet carbon isotopic composition ($\delta^{13}C_{POM}$) is directly passed on to deer bone bioapatite $\delta^{13}C$ ($\delta^{13}C_{Bone}$), we are expecting to detect, through the analysis of $\delta^{13}C_{Bone}$, any possible change in ingested plants $\delta^{13}C_{POM}$, for the reasons detailed in part 3.2.2 above.

3.4) Conclusions

The use of oxygen isotopic composition of deer bones as an aridity indicator has been proposed in 1990 (Luz *et al.*, 1990). At the same time a similar strategy has been proposed, based on kangaroos bones, also because of their low drinking water requirements (Ayliffe & Chivas, 1990).

3.4.1) Expected consequences of droughts on deer bioapatite $\delta^{18}O$

In the Maya context, we consider the deer bone oxygen isotopic ratios to be reflecting changes in the average $\delta^{18}O$ of water in the leaves consumed by the deer. This is in turn controlled by two combined effects: (1) changes in $\delta^{18}O_{rain}$ principally reflecting the *amount effect*, causing rain water the $\delta^{18}O$ to decrease with increasing amount of rainfall, and (2) the variations of relative humidity causing both leaf water $\delta^{18}O$ and soil $\delta^{18}O$ to increase with lowered humidity levels. Both of these effects would lead to a shift of bioapatite $\delta^{18}O$ ($\delta^{18}O_P$ and $\delta^{18}O_C$) to higher values during droughts.

Luz *et al.* (1990) have measured deer bone $\delta^{18}O_P$ on several specimens with wide geographic distribution in North America, and it has been shown that deer bone $\delta^{18}O_P$ is strongly dependent on yearly averages of $\delta^{18}O_{Rain}$ and relative humidity. They extracted two regression equations by multivariate regression analysis of their dataset:

$$\delta^{18}O_P = 35.9 \pm 0.881 \times \delta^{18}O_{Rain} - 0.180 \times RH \qquad (n=44; r^2=0.93) \qquad \textbf{[Eq. 3.3]}$$

$$\delta^{18}O_P = 34.63 + 0.650 \times \delta^{18}O_{Rain} - 0.171 \times RH \qquad (n=44; r^2=0.95) \qquad \textbf{[Eq. 3.4]}$$

where RH is relative humidity (between 0 and 100). They specify that given the uncertainties in their $\delta^{18}O_{Rain}$ data, they cannot judge which equation would give more reliable estimates of isotopic composition of precipitation. These two equations clearly show the main control of $\delta^{18}O_{Rain}$ on $\delta^{18}O_P$ values and its modulation by relative humidity. In their data set, because samples were taken in temperate regions, $\delta^{18}O_{Rain}$ was principally controlled by variations in air temperature. In the present study, seasonal variation in air temperature is negligible and the principal controls become those cited above.

When equations [3.3] and [3.4] are applied to the climatic dataset from Flores (refer to table 3-1 and Chapter 1, part 1.4), it becomes possible to calculate deer bone $\delta^{18}O_P$ to obtain a rough estimate of the magnitude of its change in relation with annual precipitation and yearly average relative humidity, as presented in table 3-2.

Those numbers are to be taken with caution, given the uncertainties related to the calculated values and especially the absolute $\delta^{18}O_{Rain}$ values. However, it can be seen that rain distribution and temperature variation through the year, as well as their effects on relative humidity (refer to Chapter 1, figure 1-7) can impact both $\delta^{18}O_{Rain}$ and the expected deer bone $\delta^{18}O$ values, but these aspects will be discussed later (Chapter 6).

Table 3-2. Expected deer bone bioapatite $\delta^{18}O_P$ in relation with average climatic conditions that have occurred at Flores during relatively dry (1994 and 1998) and wet years (1997 and 2006).

Year	Total precipitation (in mm)[a]	Yearly average relative humidity[a]	Estimated yearly average $\delta^{18}O_{Rain}$ at MSJ[b]	Expected deer bone $\delta^{18}O_P$ range at MSJ (in ‰)[c]	Expected deer bone $\delta^{18}O_P$ at MSJ (in ‰)[d]
1994	1,160	76	-1.9	20.5 – 23.9	20.4
1998	1,456	74	-1.6	21.2 – 24.0	20.9
1997	1,600	83	-2.3	18.9 – 23.0	18.9
2006[e]	2,395	77	-3.6	18.9 – 25.2	19.1

a: available in Flores climatic dataset (INSIVUMEH, 2009); b: using eq. [3.2]; c: using eq.[3.3]; d: using eq. [3.4]
e: November 2006 values missing and were not taken into account

In the end, it seems reasonable to expect a shift of deer bone $\delta^{18}O_P$ towards higher values by about 1.5 to 2 ‰ during dry conditions. One can notice that the magnitude of this change lies in the range calculated by Kohn (1996) using the formula and dataset of Luz *et al.* (1990), *i.e.* a $\delta^{18}O$ increase of 1.7(±0.4) ‰ per 10% decrease in yearly averaged relative humidity, corrected for $\delta^{18}O_{Rain}$ variations.

3.4.2) Expected consequences of droughts on deer bioapatite $\delta^{13}C$

As for carbon isotopic ratios, deer bone bioapatite $\delta^{13}C$ is expected to vary to the same extent as its source (see part 3.3.2 above).

Changes in humidity would be expected to affect $\delta^{13}C$ of leaves eaten by deer and therefore the $\delta^{13}C_{Bone}$. Lower humidity (*i.e.* drought) would thus be expected to lead to higher $\delta^{13}C_{Bone}$ values, but the correlation between these variables is uncertain and depends on the plants selected for diet by the deer and the response of these plants to humidity change.

The proportion of ingested C4 plants may also increase in the case of starvation, likely to occur during more arid conditions, when C3 plants with sufficient humidity amounts would no longer be available (see part 3.3 above). A higher proportion of C4 plants in deer's diet will also result in increased $\delta^{13}C_{Bone}$ values, but this latter effect of climate on available vegetation is more difficult to quantify and will be approached later (chapter 6.).

In the end, it is considered that higher $\delta^{13}C_{Bone}$ will reflect unequivocally drier conditions.

References

Ambrose S.H. & J. Krigbaum (2003) - Bone chemistry and bioarchaeology. *Journal of Anthropological Archaeology* 22, 193-199.

Ayliffe L.K. & A.R. Chivas (1990) – Oxygen isotope composition of the bone phosphate of Australian kangaroos: potential as a palaeoenvironmental indicator. *Geochimica et Cosmochimica Acta* 54, 2603-2609

Baertschi P. (1976) - Absolute ^{18}O content of Standard Mean Ocean Water. *Earth & Planetary Scicence Letters* 31, 341–44.

Barbour M.M., J.S. Roden, G.D. Farquhar, J.R. Ehleringer (2004) - Expressing leaf water and cellulose oxygen isotope ratios as enrichment above source water reveals evidence of a Péclet effect. *Oecologia* 138, 426-435.

Barbour M.M. (2007) - Stable oxygen isotope composition of plant tissue: a review. *Functional Plant Biology* 34, 83-94.

Barnard R.L., Y.Salmon, N. Kodama, K. Sörgel, J. Holst, H. Rennenberg, A. Gessler, N. Buchmann (2007) - Evaporative enrichment and time lags between $\delta^{18}O$ of leaf water and organic pools in a pine stand. *Plant, Cell and Environment* 30, 539-550.

Bello J., S. Gallina, M. Equihua (2001) - Characterization and Habitat Preferences by White-Tailed Deer in Mexico. *Journal of Range Management* 54, (5):537-545.

Bocherens H., M. Machkour, D. Billiou, E. Pelle, A. Mariotti (2001) - A new approach for studying prehistoric herd management in arid areas: intra-tooth isotopic analyses of archaeological caprine from Iran. *Earth & Planetary Science Letters* 332, 67-74.

Bowen R. (1991) - Isotopes and climates. Elsevier Applied Science, London.

Brown R.D. (1994) - Digestion. In Deer. D. Gerlach, S. Atwater & J. Schnell (Eds). Stackpole Books, pp. 66–70. Pennsylvania.

Brutsaert W. (1965) - A model for evaporation as a molecular diffusion process into a turbulent atmosphere. *Journal of Geophysical Research* 70, (20):5017-5024.

Bryant J.D. & P.N. Froelich (1995) - A Model of Oxygen-Isotope Fractionation in Body-Water of Large Mammals. *Geochimica et Cosmochimica Acta* 59, (21):4523-4537.

Bryant, J.D., P. Koch, P.N. Froelich, W.J. Showers, B.J. Genna (1996) – Oxygen isotope partitioning between phosphate and carbonate in mammalian apatite. *Geochimica et Cosmochimica Acta* 60, 5145-5148.

Cappa C.D., M.B. Hendricks, D.J. Depaolo, R.C. Cohen (2003) - Isotopic fractionation of water during evaporation. *Journal of Geophysical Research* 108, (D16):4525, doi:10.1029/2003JD003597.

Cerling T.E. & J.M. Harris (1999) - Carbon isotope fractionation between diet and bioapatite in ungulate mammals and implications for ecological and paleoecological studies. *Oecologia* 120, 247-363.

Cernusak L.A., S.C. Wong, G.D. Farquhar (2003) – Oxygen isotope composition of phloem sap in relation to leaf water in *Ricinus communis*. *Functional Plant Biology* 30, 1059-1070

Cormie A.B., B. Luz, H. P. Schwarcz (1994) - Relationship between the hydrogen and oxygen isotopes of deer bone and their use in the estimation of relative humidity. *Geochimica et Cosmochimica Acta* 58, (16):3439-3449.

Craig H. (1961) - Isotopic variations in meteoric waters. *Science* 133, 1702–1708.

Craig H. & L.I. Gordon (1965) - Deuterium and oxygen–18 variations in the ocean and the marine atmosphere. Proceedings of a conference on stable isotopes in oceanographic studies and paleo-temperatures. Tongiorgi E (eds). Spoleto, Italy, pp 9–130.

Cuntz M., J. Ogée, G.D. Farquhar, P. Peylin, L.A. Cernusak (2007) - Modelling advection and diffusion of water isotopologues in leaves. *Plant, Cell and Environment* 30, 892-909.

Dansgaard W. (1953) - The abundance of ^{18}O in atmospheric water and water vapour. *Tellus* 5, 461–69.

Dansgaard W. (1964) - Stable Isotopes in Precipitation. *Tellus* 16, (4):436-468.

Epstein S. & T. Mayeda (1953) – Variations of ^{18}O content of waters from natural sources. *Geochimica et Cosmochimica Acta* 4, 213-224.

Farquhar G.D. & R.A. Richards (1984) - Isotopic composition of plant carbon correlates with water-use efficiency of wheat genotypes. *Australian Journal of Plant Physiology* 11, (6): 539-552.

Farquhar G.D., J.R. Ehleringer, K.T. Hubick (1989) – Carbon isotopes discrimination and photosynthesis. *Annual Review of Plant Physiology and Plant Molecular Biology* 40, 503-537.

Farquhar G.D., L.A. Cernusak, B. Barnes (2007) – Heavy water fractionation during transportation. *Plant Physiology* 143, 11-18.

Flanagan L.B., J.P. Comstock, J.R. Ehleringer (1991) - Comparison of modeled and observed environmental influences on the stable oxygen and hydrogen isotope composition of leaf water in *Phaseolus vulgaris* L.. *Plant Physiology* 96, 588-596.

Fravolini A., D.G. Williams, T.L. Thompson (2002) - Carbon isotope discrimination and bundle sheath leakiness in three C$_4$ subtypes grown under variable nitrogen, water and atmospheric CO2 supply. *Journal of Experimental Botany* 53, (378):2261-2269.

Fricke H.C. & J.R. O'Neil (1996) - Inter- and intra-tooth variation in the oxygen isotope composition of mammalian tooth enamel phosphate: Implications for palaeoclimatological and palaeobiological research. *Palaeogeography Palaeoclimatology Palaeoecology* 126, (1-2):91-99.

Friedman I., L. Machta, R. Soller (1962) - Water vapour exchange between a water droplet and its environment. *Journal of Geophysical Research* 67, 2761–2766.

Gat J.R. (1996) - Oxygen and hydrogen isotopes in the hydrologic cycle. *Annual Review of Earth and Planetary Sciences,* 225-262.

Gat J.R., W.G. Mook, Meijer H.A.J. (2000) – Volume II : Atmospheric water. Environmental Isotopes in the Hydrological Cycle : Principles and Applications. IAEA editions (online ressource).

Ghannoum O., S. Von Caemmerer, J.P. Conroy (2002) – The effect of drought on plant water use efficiency of nine NAD-ME and nine NADP-ME Australian C$_4$ grasses. *Functional Plant Biology* 29, 1337-1348.

Harlow, R.F. & D.C. Guynn (1994) – White-tailed deer habitats and ranges. In Deer. D. Gerlach, S. Atwater & J. Schnell (Eds). Stackpole Books, pp. 169-173. Pennsylvania.

Haug G.H., D. Günther, L.C. Peterson, D.M. Sigman, K.A. Hughen, B. Aeschliman (2003) - Climate and the collapse of Maya civilization. *Science* 299, 1731-1735.

Hervert J.J. & P.R. Krausman (1986) - Desert Mule Deer Use of Water Developments in Arizona. *The Journal of Wildlife Management* 50, (4):670-676.

IAEA (2009) – International Atomic Energy Agency. *Isotopes in precipitation.* Accessed online <http://www.iaea.org> , July 2009.

IAEA/WMO (2009) - Global Network of Isotopes in Precipitation. *The GNIP Database.* Accessed online <http://isohis.iaiea.org>, April 9, 2009.

INSIVUMEH (2009) – Instituto Nacional de Sismologia, Vulcanologia, Meteorolgia e Hidrologia (Guatemala). *Estadísticas Climáticas.* Accessed online <http://www.insivumeh.gob.gt>, August 2008.

Jim S., S.H. Ambrose, R.P. Evershed (2004) - Stable carbon isotopic evidence for differences in the dietary origin of bone cholesterol, collagen and apatite: Implications for their use in palaeodietary reconstruction. *Geochimica et Cosmochimica Acta* 68, (1): 61–72.

Johnson D.A., K.H. Asay, L.L. Tieszen, J. Ehleringer, P. Jefferson (1989) – Carbon isotope discrimination: a possible criterion for improving range grass production in water limited environment. *Crop Science* 30, 338-343.

Kelly J.F. (2000) – Stable isotopes of carbon and nitrogen in the study of avian and mammalian trophic ecology. *Canadian Journal of Zoology* 78,1-27.

Koch P. (1998) – Isotopic reconstruction of past continental environments. *Annual Review of Earth & Planetary Science Review* 26, 573–613.

Kohn M.J. (1996) – Predicting animal $\delta^{18}O$: accounting for diet and physiological adaptation. *Geochimica et Cosmochimica Acta* 60, 4811-4829.

Kohn M.J. (1999) – You are what you eat. *Science* 283, (5400):335-336.

Kohn M.J. & T.E. Cerling (2002) - Stable Isotope Compositions of Biological Apatite. in: M.J. Kohn, J. Rakovan, J.M. Hughes (Eds.), Phosphates: Geochemical, Geobiological and Material Importance, Reviews in Mineralogy and Geochemistry, vol. 48, Mineralogical Society of America, Washington, DC, pp. 255–292.

Kroll, J.C. (1994) - Internal anatomy. In Deer. D. Gerlach, S. Atwater & J. Schnell (Eds). Stackpole Books, pp. 24-30. Pennsylvania.

Lachniet M.S. & W.P. Patterson (2009) - Oxygen isotope values of precipitation and surface waters in northern Central America (Belize and Guatemala) are dominated by temperature and amount effects. *Earth and Planetary Science Letters* 284, (3-4):435-446.

Landais A., E. Barkan, D. Yakir, B. Luz (2006) - The triple isotopic composition of oxygen in leaf water. *Geochimica et Cosmochimica Acta* 70, 4105-4115.

Lautier J.K., T.V. Dailey, R.D. Brown (1988) - Effect of Water Restriction on Feed Intake of White-Tailed Deer. *The Journal of Wildlife Management* 52, (4):602-606.

Lawrence J.R., S.D. Gedzelman, D. Dexheimer, H.-K. Cho, G.D. Carrie, R. Gasparini, C.R. Anderson, K.P. Bowman, M.I. Biggerstaff (2004) - Stable isotopic composition of water vapor in the tropics. *Journal of Geophysical Research* 109, D06115, doi:10.1029/2003JD004046.

Lee-Thorp J.A., J.C. Sealy, N.J. Van der Merwe (1989) - Stable carbon isotope ratio differences between bone collagen and bone apatite, and their relationship to diet. *Journal of Archaeological Science* 16, 585-599.

Lee-Thorp J.A. (2002) – Preservation of biogenic carbon isotopic signals in Plio-Pleistocene bone and tooth mineral. In Biogeochemical approaches to paleodietary analysis. Ambrose & Katzenberg (Eds). Kluwer Academic/Plenum Publishers. New York.

Lee-Thorp J.A. & M. Sponheimer (2005) - Opportunities and constraints for reconstructing palaeoenvironments from stable light isotope ratios in fossils. *Geological Quarterly* 49, (2): 195-204.

Longinelli A. (1984) - Oxygen Isotopes in Mammal Bone Phosphate - a New Tool for Paleohydrological and Paleoclimatological Research. *Geochimica et Cosmochimica Acta* 48, (2):385-390.

Luz B., Y. Kolodny, M. Horowitz (1984) - Fractionation of Oxygen Isotopes between Mammalian Bone Phosphate and Environmental Drinking-Water. *Geochimica et Cosmochimica Acta* 48, (8):1689-1693.

Luz B., A.B. Cormie, H.P. Schwarcz (1990) - Oxygen isotope variations in phosphate of deer bones. *Geochimica et Cosmochimica Acta* 54, 1723-1728.

MacFadden B.J. & T.E. Cerling (1996) - Mammalian herbivore communities, ancient feeding ecology, and carbon isotopes: a 10 million-year sequence from the Neogene of Florida. *Journal of Vertebrate Paleontology* 16, 103–115.

Majoube M. (1971) - Fractionnement en oxygène-18 et en deuterium entre l'eau et sa vapeur. *Journal de Chimie Physique* 10, 1423-1436.

Medina E., H. Klinge. C. Jordan, R. Herrera (1980) - Soil respiration in Amazonian rain forests in the Rio Negro basin. *Flora* 170, 240-250.

Medina E. & P. Minchin (1980) - Stratification of $\delta^{13}C$ values of leaves in Amazonian rain forests. *Oecologia* 45, 371-318.

Merlivat L. & M. Coantic (1975) - Study of mass transfer at the air-water interface by an isotopic method. *Journal of Geophysical Research* 80, 3455-3464.

Merlivat L. & J. Jouzel (1979) - Global climatic interpretation of the deuterium-oxygen 18 relationship for precipitation. *Journal of Geophysical Research* 84, 5029–5033.

Passey B.H., T.F. Robinson, L.K. Ayliffe, T.E. Cerling, M. Sponheimer, M.D. Dearing, B.L. Roeder, J.R. Ehleringer (2005) - Carbon isotope fractionation between diet, breath CO_2, and bioapatite in different mammals. *Journal of Archaeological Science* 32, 1459-1470.

Rindsberger M. & M. Magaritz (1983) - The relation between air-mass trajectories and the water isotope composition of rain in the Mediterranean Sea area. *Geophysical Research Letters* 10,43– 46.

Rozanski K., L. Araguas-Araguas, R. Gonfiantini (1992) - Relation between Long-Term Trends of O-18 Isotope Composition of Precipitation and Climate. *Science* 258, (5084):981-985.

Rozanski K., K. Froehlich, W.G. Mook (2000) – Volume III : Surface waters. Environmental Isotopes in the Hydrological Cycle : Principles and Applications. IAEA editions (online ressource)

Sullivan C.H. & H.W. Krueger (1981) - Carbon isotope analysis of separate chemical phases in modern and fossil bone. *Nature* 292, 333-335.

Tieszen, L.L. (1991) – Natural variations in the carbon isotope values of plants: implications for archaeology, ecology, and paleoecology. *Journal of Archaeological Science* 18, 227-248

Van Der Merwe N.J. & E. Medina (1991) – The Canopy Effect, Carbon Isotope Ratios and Foodwebs in Amazonia. *Journal of Archaeological Science* 18, 249-259.

Villareal O. & Marín M. (2005) – Agua de origen vegetal para el venado cola blanca mexicano. *Archivos de Zootecnia* 53, (206-207):191-196

Vogel J.C. (1978) - Recycling of CO_2 in a forest environment. *Oecologia Pluntarum* 13, 89-94.

Ward A.D. & W.J. Elliot (1995) - Environmental Hydrology, CRC Lewis Publishers.

Webb E.A. & F.J. Longstaffe (2006) - Identifying the $\delta^{18}O$ signature of precipitation in grass cellulose and phytoliths: refining the paleoclimate model. *Geochimica et Cosmochimica Acta* 70, 2417-2426.

Yurtsever Y. (1975) - Worldwide survey of stable isotopes in precipitation. In Reports, section isotope hydrology. International Atomic Energy Agency, Vienna.

Appendix 3.A – Water evaporation in thermodynamic equilibrium

In a closed air-water system, the saturation water vapour pressure (ρ_{SAT}) and oxygen equilibrium (thermodynamic) fractionation factors of vaporization (${}^{18}\alpha_{L/V}$) or condensation (${}^{18}\alpha_{V/L}$) are strictly temperature-dependant and have been calculated empirically.

3.A.1) Equilibrium fractionation factor

${}^{18}\alpha$, the equilibrium fractionation factor for ${}^{18}O$ during phase change has been calculated empirically by Majoube (1971) and is given by:

$$\ln {}^{18}\alpha_{V/L} = -\ln {}^{18}\alpha_{L/V} = 2.0667\times10^{-3} + \frac{0.4156}{T_W} + \frac{1.137\times10^{-3}}{T_W{}^2} \qquad \textbf{[Eq. 3.A.1]}$$

where T_W is the absolute water temperature, in degrees Kelvin. Equation [3.A.1] is valid for temperatures ranging from 0 to 100°C (Rozanski *et al.*, 2000).

3.A.2) Saturation vapour pressure

Saturation vapour pressure ρ_{SAT} was calculated empirically (Ward & Elliot, 1995) and is given by:

$$\rho_{SAT} = \exp\left(\frac{16.78\times T - 116.9}{T + 237.3}\right) \qquad \textbf{[Eq. 3.A.2]}$$

where T is the air temperature of the system, expressed in degrees Celsius, and ρ_{SAT} is given in kPa. Equation [3.A.2] is valid for temperatures ranging from 0 to 50°C (table 3-A-1; Rozanski *et al.*, 2000).

Table 3-A-1. Vaporization equilibrium fractionation factors ${}^{18}\alpha_{L/V}$ (Majoube, 1971) and saturation vapour pressures (Ward & Elliot, 1995) at temperature ranging from 0 to 29°C.

T (°C)	${}^{18}\alpha_{L/V}$	ρ_{SAT} (hPa)	T (°C)	${}^{18}\alpha_{L/V}$	ρ_{SAT} (hPa)	T (°C)	${}^{18}\alpha_{L/V}$	ρ_{SAT} (hPa)
0	1.01173	6.110	10	1.01071	12.285	20	1.00980	23.396
1	1.01162	6.570	11	1.01062	13.133	21	1.00972	24.884
2	1.01152	7.059	12	1.01052	14.032	22	1.00963	26.455
3	1.01141	7.581	13	1.01043	14.985	23	1.00955	28.111
4	1.01131	8.136	14	1.01034	15.994	24	1.00946	29.857
5	1.01121	8.727	15	1.01025	17.062	25	1.00938	31.697
6	1.01111	9.355	16	1.01015	18.192	26	1.00930	33.635
7	1.01101	10.023	17	1.01007	19.388	27	1.00922	35.676
8	1.01091	10.732	18	1.00998	20.651	28	1.00914	37.823
9	1.01081	11.486	19	1.00989	21.986	29	1.00906	40.083

Appendix 3.B - The Craig-Gordon model

The key-point of Craig-Gordon model (Craig & Gordon, 1965) is that atmosphere above a water surface is no longer considered as a uniform gaseous volume (as in thermodynamic equilibrium model), but is rather seen as a superposition of sublayers where different kinetic fractionation processes occur. From the surface of water to the free atmosphere, Craig-Gordon model distinguishes at least three sublayers (figure 3-B-1), assuming no divergence or convergence of air masses in the vertical air column.

3.B.1) Interface water surface – atmosphere

In the interface layer, thermodynamic equilibrium is considered as occurring: vapour is in isotopic equilibrium with water. Isotopic composition of the vapour (δ_V) in this layer is then strictly dependant on both isotopic composition of the water (δ_L) and the surface temperature of the water, the latter affecting the equilibrium fractionation factor of vaporisation ($^{18}\alpha_{L/V}$; see Appendix 3.A).

3.B.2) Diffusive sublayer

In this layer (also called viscous diffusive layer), air mass is considered as motionless. The difference of partial vapour pressure (humidity gradient) between water-air interface (where air is saturated, *i.e.* where relative humidity is 100 %) and the upper atmosphere (where relative humidity h' < 1) is leading to vapour diffusion. Two aspects of the phenomenon must be then considered: (1) the flux density of vapour and (2) the different diffusivities of gaseous water isotopomers.

(1) *Flux density of vapour.* The vapour follows Fick's law: the rate of diffusion of vapour in air is proportional to the negative of the gradient of the concentration of vapour. The rate of diffusion (flux density) is expressed in $mol.m^{-2}.s^{-1}$. The lower the vapour pressure of the upper layer is, the denser the flux of water vapour through the layer is. In other words, the dryer the upper

atmosphere is, the faster the vapour will flow through the layer, and as a result, the more vapour will enter the atmosphere.

(2) *Diffusivities of gaseous water isotopomers.* It is due to the differential diffusivities of gaseous $H_2{}^{16}O$ and $H_2{}^{18}O$. During diffusion, molecular transport is dominating. Following Graham's law, the diffusion constant (diffusivity) of a gas in another (expressed in $m^2.s^{-1}$) in a given set of conditions (temperature and pressure) is proportional to molecule mass. Because of that molecular mass difference (rather than atomic masses differences), the average diffusivity D_{18} of gaseous $H_2{}^{18}O$ in air will be slightly less than the one of $H_2{}^{16}O$ (D_{16}). As predicted by the kinetic theory of gases, the ratio D_{18}/D_{16} is 0.9691. The forces opposing the fluxes of light and heavy vapour (resistances ρ_M and ρ_{Mi} respectively, as shown in figure 3-B-1) are then equal to the inverse of the diffusivities of gaseous $H_2{}^{16}O$ and $H_2{}^{18}O$ in air (*i.e.* the conductance of air with respect to vapour). In motionless air, ρ_M and ρ_{Mi} are thus approaching $D_{16}{}^{-1}$ and $D_{18}{}^{-1}$, respectively (Gat *et al.*, 2000).

During its diffusion through the diffusive sublayer, vapour will thus become more and more depleted in ^{18}O while moving away from the interface, due to the kinetic fractionation factor.

3.B.3) Turbulently mixed sublayer

In this sublayer, atmospheric air masses are moving, subsequently transporting vapour. It is assumed that no isotope fractionation occurs during a fully turbulent transport (i.e. $\rho_T = \rho_{Ti}$, see figure 3.B.1; Gat, 1996). Atmospheric modelers refer the transport effects to as kinetic effects, not to be confused with a standard kinetic isotope effect which refers to isotope-dependant reaction rates of microscopic processes (Cappa *et al.*, 2003).

In the case of a completely stagnant air layer above the water surface (no turbulences), only diffusion occurs, as described above. For water surface under strong wind conditions, turbulent mixing of air is constantly removing newly formed vapour at the top of the diffusive sublayer. This continuous creation of drier areas over the diffusive layer happens in a random motion, and the transient-eddy model (Brutsaert, 1965) is then applied. Briefly, because the humidity gradient is still present between the base and the top of the sublayer (h'> h_N; figure 3-B-1), diffusion still occurs, but in that sublayer, the eddies induced by air mass movements decrease the forces opposing the fluxes of light and heavy vapour (ρ_M and ρ_{Mi}), analogous to a suction force increasing flux density of vapour. During strong wind conditions (also increasing surface roughness), ρ_M and ρ_{Mi} are mathematically considered as approaching $D_{16}^{-1/2}$ and $D_{18}^{-1/2}$, respectively (Merlivat & Coantic, 1975).

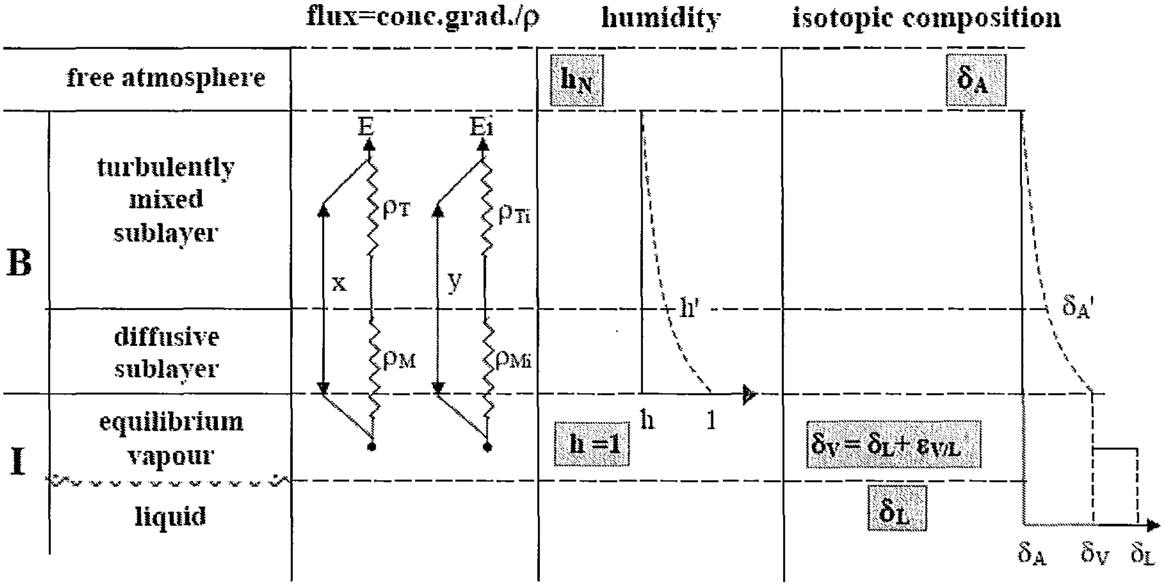

Figure 3-B-1. The Craig-Gordon model for isotopic fractionation during evaporation of open water body into the free atmosphere (from Gat *et al.*, 2000).

I is the interface zone, where vapour is in isotopic equilibrium, and B is the atmospheric boundary layer, subdivised in the diffusive sublayer and the turbulently mixed sublayer.

Isotopic composition: δ_L refers to the isotopic composition of the evaporating body of water, δ_V is the one of the water vapour in equilibrium at the interface, $\delta_{A'}$ is the one of the air moisture at the boundary of the diffusive sublayer, and δ_A is the one of the free atmosphere moisture. $\varepsilon_{V/L}$ is the deviation of $\alpha_{V/L}$ from 1 ($\varepsilon_{V/L} = \alpha_{V/L} - 1$).

Humidity: h is the relative humidity of the atmosphere at the interface water-atmosphere (h=1), h' and h_A are the relative humidities at the boundary of the diffusive sublayer and of the free atmosphere, respectively. h_N is the relative humidity of the free atmosphere over the body of water, normalised to the surface temperature of the liquid water.

Fluxes of vapour in Ohmian representation: E represents the water vapour flux. ρ terms are for the appropriate resistances as explained in the text. Subscripts M and T signify the diffusive and turbulent sublayer, respectively. Right pathway (subscripts i) is concerning the heavy molecules ($H_2{}^{18}O$), while left pathway is for all vapour molecules. Because no isotope differentiation occurs in the turbulent mixed sublayer, $\rho_T = \rho_{Ti}$. x and y are the gradient of concentration of water vapour and heavy water vapour in the atmosphere.

This explains why a fractionation effect is still observed while moving away from the diffusive sublayer towards free atmosphere, in a lesser extent than the fractionation occurring in the diffusive sublayer (figure 3-B-1).

3.B.4) The two aspects of Craig-Gordon model

Craig-Gordon model is primarily considering the flux of water vapour during the evaporation of a body of water. This flux of water vapour, and then the amount of gaseous $H_2{}^{18}O$ entering the atmosphere, is described in terms equivalent to an Ohmian law, so that this flux density depends on the quotient of the vapour concentration gradient (expressed as the humidity difference) and the transport resistance (forces opposing the vapour flux).

Secondly, among this water vapour flux, three factors are involved in determining the overall isotope fractionation (Gat, 1996): (1) the equilibrium fractionation of the liquid to vapour phase transition (*i.e.* the temperature of the water surface), (2) the fractionation resulting from the different diffusivities of isotopomers of vapour through the boundary layer (kinetic fractionation) and (3) the back flux of atmospheric moisture (air mass movements).

3.B.5) The endothermic nature of evaporation

Due to the endothermic nature of evaporation, if heat is not supplied to the surface of an evaporating surface of water, the surface temperature of that water will cool below the bulk value. So rather than using a value of ${}^{18}\alpha_{L/V}$ as given in table 3-A-1 (Appendix 3.A) corresponding to the bulk water temperature, a more appropriate one corresponding to the temperature of the cooled surface should be used, so this temperature needs to be known.

Using existing data and lab experiments, Cappa *et al.* (2003) have been able to calculate a surface cooling coefficient of ~ 0.505°C per mmol of evaporated water, per m^2, per s^2 ($mmol^{-1}.m^{-2}.s^{-2}$) in an air of 19°C. They estimate that surface cooling of an evaporating dish (with a surface of ~ 34 cm^2) subjected to air streams with fixed relative humidities can range from 1.8°C (50%

relative humidity, hence low evaporation rate) to more than 4°C (0% relative humidity, hence high evaporation rate).

In addition to changing the equilibrium fractionation factor $^{18}\alpha_{L/V}$, the surface cooling also affects the diffusivity of vapour in air (Graham's law). The extent of the variation of "diffusive" (*i.e.* kinetic) fractionation factor (α_{diff}) has been calculated by Cappa *et al.* (2003) for surface coolings of 1, 3 and 5°C and is shown in figure 3-B-2. They stress that if a surface cooling of 3°C is considered, the measured experimental values of α_{diff} are in accordance with the calculated ones.

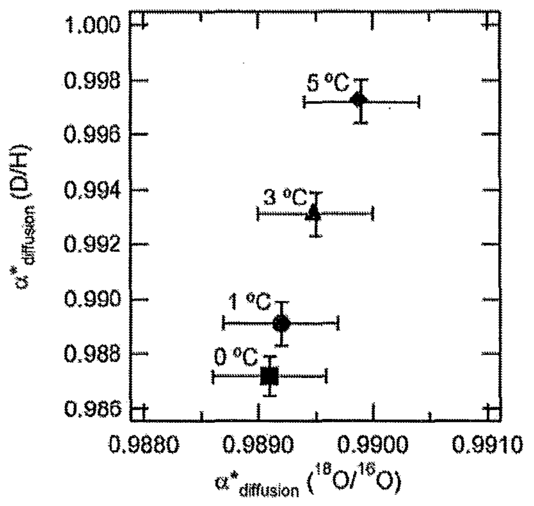

Figure 3-B-2. The diffusive fractionation factors (α_{diff}) calculated for $^2H/^1H$ and $^{18}O/^{16}O$ for a dish with an evaporative surface of ~ 34 cm^2 subjected to a continuous airstream of constant 20 % relative humidity. α_{diff} were calculated using the bulk liquid temperature (■), and surface coolings of 1°C (●), 3°C (▲) and 5°C (♦).
From Cappa *et al.* (2003).

In conclusion, when modelling water isotope fractionation during evaporation processes, it is necessary to consider the evaporative surface temperature rather than the bulk temperature of the water, as it is this temperature that determines the equilibrium fractionation factors to be used ($^{18}\alpha_{L/V}$) as well as the diffusive fractionation factor α_{diff} (Cappa *et al.*, 2003).

Appendix 3.C - The Craig-Gordon model adapted to leaf water evaporation

The adaptation of Craig-Gordon model (Appendix 3.B) to describe leaf water evaporation includes some fitted parameters (Flanagan *et al.*, 1991). The model states that leaf water enrichment above source water ($\Delta 18O_{ES}$) is due to fractionation associated with water diffusion through stomata and leaf boundary layer (*i.e.* kinetic fractionation factor ε_k), phase transition (*i.e.* equilibrium fractionation factor ε^+, analogous to $^{18}\alpha_{L/V}$ depending on leaf surface temperature) and oxygen isotope composition of vapour relative to source water ($\delta^{18}O_V$). It is also stated that the extent of that enrichment is controlled by water vapour pressure differences of the gas phase inside and outside the leaf (ratio of atmospheric to intercellular vapour mol fraction e_a/e_i, also called relative humidity normalized to leaf temperature; Barbour, 2007). The adaptation of Craig-Gordon model is accepted under the assumption of isotopic steady state (Barnard *et al.*, 2007).

When leaf water is at isotopic steady state, the isotopic composition of the transpiration water is the same as the source or stem water isotopic composition (Flanagan *et al.*, 1991). The leaf water enrichment above source water is then given by the following equation:

$$\Delta^{18}O_{ES} = \varepsilon^+ + \varepsilon_k + \left(\delta^{18}O_V - \varepsilon_k\right) e_a / e_i \qquad \textbf{[Eq. 3.C.1]}$$

As ε^+ is strictly temperature-dependant (see appendix 3.A), and (e_a/e_i) is easily measurable, if the total kinetic fraction factor ε_k is known, then leaf water enrichment above source water is calculable. Once Craig-Gordon model is adapted to leaf water enrichment, the forces opposing the diffusion of vapour are still due to boundary layer resistance, but the stomatal resistance must also be taken into account. According to Farqhuar *et al.* (2007), ε_k in (*‰*) is given by:

$$\varepsilon_k = \frac{32r_s + 21r_b}{r_s + r_b} \qquad \textbf{[Eq. 3.C.2]}$$

where r_s and r_b are stomatal and boundary layer conductances, respectively. Fractionation factor for diffusion of vapour through air (and stomata) has been determined by Cappa *et al.* (2003) to be 32 ‰ and the one for diffusion of vapour through the boundary layer is taken by Cernusak *et al.* (2003) to be 21 ‰ (given a 2/3 power effect at moderate wind speeds, see appendix 3.B).

The water volume of a leaf and the transpiration rate are characteristics influencing the leaf water turnover time, and therefore the time required to reach the isotopic steady-state (Flanagan *et al.*, 1991). This time was assessed experimentally and is given to be as approximately 1 hour for the thin small leaves of common bean plants (*Phaseolus vulgaris* L.), and is thought to be significatively much longer for leaves of succulent plants with high water content and low transpiration rates (such as Crassulaceae or C4 plants; Flanagan *et al.*, 1991).

But, as mentioned by Cuntz *et al.* (2007), a number of studies have reported that observed leaf water is either slightly less or more enriched than the prediction of Craig-Gordon model. Subsequent improvements of the Craig-Gordon model have been studied to take into account specific effects occurring leaf water enrichment, such as the *Péclet effect.* Those effects are important when modelling leaf water enrichment with high accuracy, but will not be approached further in the present study.

Chapter 4 - Method

This chapter summarizes the methods that have been used to analyze the oxygen and carbon isotopic compositions of deer bones from the Maya area. The sampling procedure is presented first, followed by the protocol for $\delta^{18}O_P$ measurement as well as the one for simultaneous $\delta^{18}O_C$ and $\delta^{13}C_{Bone}$ measurements. The rest of the chapter emphasizes on the detection and quantification techniques of *post-mortem* chemical alterations the bone samples could have been subjected to.

4.1) Sampling procedure

Isotopic measurements and infra-red spectrometry require the destruction of part of these valuable archaeological samples. In order to preserve any possible information given by bone external aspect for later exploitation by archaeologists (e.g.: colour, racloir or cutting traces), a set of high-resolution pictures were taken for each bone prior to the analyses.

On each sample, a small piece (~0.5 cm^3) of cortical (dense) bone has been sampled in zones where cortical bone layer was the thickest. The external and internal layers of cortical bone were manually removed to a depth of about 2 mm, using a hand-held electric drill kept at low speed under a trickle of water (to prevent any local heating), to completely remove the periosteum, endosteum and beyond. Among the 98 bones analyzed in this study, 24 of them were considered large enough and/or with no apparent archaeological value to be sampled on two different locations.

Every sample has then been dried overnight in a drying cabinet (50°C) to remove possible tap-water contamination. Once completely dry, bone fragments were ground in liquid nitrogen using a cryo-crusher (SPEX™ SamplePrep), following the same grinding program (strength and duration), to obtain a very fine-grained homogenised powder. The resulting powder mass ranged from 1 to 2 grams per sample.

4.2) Isotopic measurements

Oxygen ($\delta^{18}O_P$ and $\delta^{18}O_C$) and carbon ($\delta^{13}C_{Bone}$) isotopic results are presented relatively to Vienna Standard Mean Ocean Water (VSMOW) and Vienna Pee Dee Belemnite (VPDB), respectively, using the standard delta (δ) notation in per mille (‰; Coplen, 1996; refer also to equation [3.1] in Chapter 3). All isotopic analyses were replicated three times, and were conducted in the stable isotope laboratory at the School of Geography & Earth Sciences, McMaster University (Ontario, Canada). The reproducibilities of the following methods will be presented in Chapter 5 (part 5.1) and their reliability will be discussed in Chapter 6.

4.2.1) Bioapatite $\delta^{18}O_P$

The sample preparation for $\delta^{18}O_p$ analyses followed the protocol from Bassett *et al.* (2007). This protocol is a modification of the "quick method" established by Dettman *et al.* (2001) to avoid the utilization of extremely corrosive and highly toxic hydrofluoric acid (HF), commonly used for such analyses.

The extraction of phosphate groups (PO_4^{3-}) from bone bioapatite mineral lattice is done in 6 steps: (1) 5000 µg of powder is first reacted for 48 hours in 15 mL falcon test tube with ~10mL of 2.5% sodium hypochlorite (NaOCl) to partly dissolve bone organic matrix (see Chapter 2, part 2.2) and the remaining material (*i.e.* the mineral part and associated collagen) is then carefully rinsed five times with double de-ionized (DDI) water and dried at 50°C until complete desiccation; (2) the dried powder is then dissolved in 500 µL nitric acid (HNO_3) at 0.5 mol.L^{-1} (molar or M) to dissolve bioapatite phosphate groups; (3) the pH of the solution is then raised by an addition of 375 µL of potassium hydroxide (KOH, 0.5 M); (4) calcium ions and remaining collagen are removed by precipitation and centrifugation, provoked by the addition of 1000 µL of ammonium fluoride (NH_4F, 0.2 M); (5) the supernatant is transferred in a low binding tube in which 1250 µL of silver amine solution are added ($AgNO_3$, 0.2M; NH_4NO_3, 0.35 M; NH_4OH, 0.74M), to precipitate bone bioapatite phosphate into silver phosphate crystals (Ag_3PO_4) during 48 hours in a drying oven at 50°C, and (6) the silver phosphate crystals are then carefully rinsed five times with DDI water and dried overnight in a drying oven at 50°C.

The dried silver phosphate crystals were subsequently transferred into silver cups for $\delta^{18}O_P$ measurements. Silver cups were dropped into a graphite crucible at 1440°C on a Thermo Finnigan high Temperature Conversion/Elemental Analyzer (TC/EA), where silver phosphate crystals are fully dissociated by thermal decomposition, and ionized oxygen species are recombined with carbon atoms from the crucible. The resulting carbon monoxide (CO) was then carried out to a Thermo Finnigan DeltaPlus Gas Chromatograph-Isotope Ratio Mass Spectrometer (GC-IRMS), where oxygen isotope ratio ($\delta^{18}O_P$) is measured.

4.2.2) Bioapatite $\delta^{18}O_C$ & $\delta^{13}C_{Bone}$

Bioapatite $\delta^{18}O_C$ and $\delta^{13}C_{Bone}$ are measured simultaneously. The sample preparation for $\delta^{18}O_C$ and $\delta^{13}C_{Bone}$ analyses has been adapted from the offline method outlined by Koch *et al.* (1997).

The extraction of oxygen and carbon atoms from carbonate groups is done in 4 steps: (1) 75 mg of bone powder is first reacted for 72 hours in 15mL falcon test tube with ~10mL of 2.5% sodium hypochlorite (NaOCl) to dissolve part of the bone organic matrix, and the remaining material (*i.e.* the mineral part and associated collagen) is then carefully rinsed five times with DDI water and dried at 50°C until complete desiccation; (2) the dried powder is then reacted during 12 hours with a 1 M solution of weak acetic acid (CH_3-COOH) buffered with acetate ions (CH_3-COO^-), to "etch" the surface of bioapatite crystallites, in order to remove any secondary carbonate that could have been adsorbed or replaced diagenetically at the surface of bioapatite crystallites (Wright & Schwarcz, 1996; Koch *et al.*, 1997), and the remaining powder is then carefully rinsed five times with DDI water and dried overnight in a drying oven at 50°C; (3) 25 mg of that powder is then transferred into Pyrex boats and sealed into 9 mm Pyrex tubes containing ~2 ml of 100% anhydrous phosphoric acid (H_3PO_4) under vacuum; sealed tubes are then placed in a water bath, at 25°C and inverted to react the bone powder with the acid, according to the following equation (quantitative reaction);

$$CaCO_3 + H_3PO_4 \rightarrow CaHPO_4 + CO_2 + H_2O \qquad \textbf{[Eq. 4.1]}$$

(4) the extraction of the resulting CO_2 is done after 3 days, on a transfer line, where 9 mm sealed pyrex tube is opened under vacuum, so water and other non-condensible gases can be removed cryogenically, and the evolved CO_2 is then purified and collected into a 6 mm pyrex tube.

The resulting CO_2 was then analyzed on an Optima GC-IRMS, in which $\delta^{13}C_{Bone}$ and $\delta^{18}O_C$ were measured simultaneously.

4.3) Diagenesis assessment

Structure and chemical composition of archaeological bones can potentially be altered after animal's death by natural processes like disintegration, dissolution, precipitation, bacterial remodelling, mineral replacement, ionic substitutions or recrystallization (e.g.: Hedges, 2002; Munro *et al.*, 2007). Each of these phenomena is a possible form of diagenesis, defining the post-burial processes affecting the physical and chemical properties of sediments (*sensu strictu*) and, by extension, biological remains.

In the case of paleoclimatic reconstructions based on isotopic analyses, it is crucial to scrupulously ensure that (1) the measured isotopic ratios ($\delta^{18}O_P$, $\delta^{18}O_C$ and $\delta^{13}C_{Bone}$) are really those corresponding to the bioapatite crystallites formed during deer's life, and (2) that no chemical alteration of these crystallites occurred since the death of the animal (*i.e.* that bones have kept their original isotopic signature).

In addition to a visual examination of archaeological remains aspect (mainly to detect physical alteration), the extent of diagenetic alteration can be assessed by the study of three side-effects of chemical remodelling: a different alteration of carbonate groups compared to phosphate groups, a crystallinity increase and a change in the degree of ionic substitution on the crystal lattice. Those facets are developed below.

4.3.1) Appearance

The fastest way to partially screen archaeological material for geochemical analyses is to visually check its physical characteristics. Colour, morphological and histological study can give information on a possible bacterial, fungal or plant attack, as well as to detect if bones have been burnt (Shipman *et al.*, 1984; Nicholson, 1993). For example, biological attack (*i.e.* the use of collagen as nutrient source by a biological agent) is believed to induce strong chemical alteration, but little is clear about those mechanisms, and their effects on the mineral part of bones (see Hedges, 2002 for an overview of what is currently known).

The way the Maya people prepared the deer meat before consumption is also important: burning and boiling are not diagenetic effects strictly speaking (they are not post-burial processes), but they are *post-mortem* processes. Boiling and/or burning bones can affect (or not) deer bone bioapatite isotopic values. Munro *et al.* (2008) have measured the $\delta^{18}O_P$ and $\delta^{18}O_C$ on heated samples of white-tailed deer bones, after having boiled them and/or having heated them up to 900°C. They indicate that when the bones are heated below 250°C [300°C], the original $\delta^{18}O_P$ [$\delta^{18}O_C$] values are preserved (either boiled before heating or not; figure 4-1). Beyond this temperature, the values fluctuate and can decrease up to ~8 ‰. It can be considered that the heat possibly released by the decomposition of refuse in middens does not seem to deteriorate the original isotopic values, neither if the bones have been boiled.

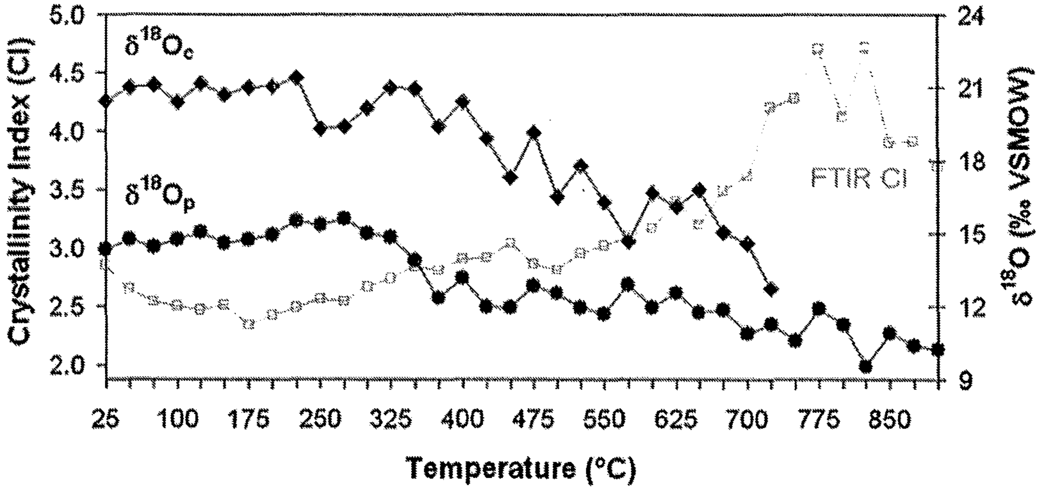

Figure 4-1. Comparison of bone apatite $\delta^{18}O_C$ (♦) and $\delta^{18}O_P$ (●) values with FTIR CI (□; see part 4.3.3.2) values measured on heated aliquots of a bone sample. Modified, after Munro *et al.* (2008).

Munro *et al.* (2007) also established a burnt bone colour index, allowing the evaluation of the temperature at which a bone has been exposed. As it can be seen on figure 4-2, it is at near 300°C that the bone colour starts to change noticeably (the bone is turning from cream-colour to black).

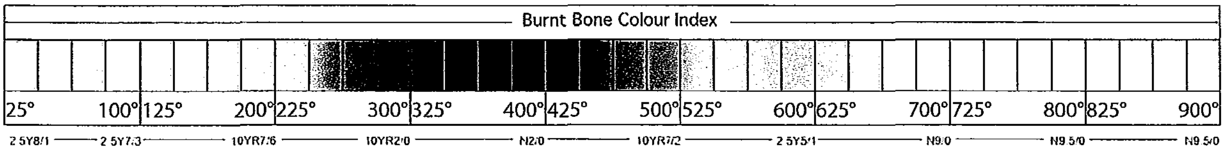

Figure 4-2. Colours obtained by Munro *et al.* (2007) for bones samples heated from 25°C to 900°C in 25°C increments. Colours for samples boiled prior to dry heating were the same at a given temperature, as those produced by dry heating alone. The colour codes are given in the Munsell Colour system. From Munro *et al.* (2007).

Ultimately, to minimize the use of altered bones, charred and crumbly bones were automatically screened out. Only cortical (dense) bone has been sampled. Due to its low porosity, it is believed that cortical (dense) bone mineral is less exposed to fluid circulation (and thus possible chemical interaction with them) in the sediment layers than cancellous (spongy) bone (refer to Chapter 2, part 2.2.1).

4.3.2) Comparison $\delta^{18}O_C$ / $\delta^{18}O_P$

As stated in Chapter 3 (part 3.3.1), there is an isotopic equilibrium between mineralised tissues (bones and teeth) and body water (e.g.: Longinelli, 1984; Luz *et al.*, 1984; Bryant & Froelich, 1995; Fricke & O'Neil, 1996). Bryant *et al.* (1996) notice this link is not surprising, given the presence in blood of enzymes catalyzing oxygen isotope exchange between bone phosphate and body water (ATPases; Faller & Elgavish, 1984), and between CO_2, bicarbonate and body water (carbonic anhydrase; Silverman, 1982).

Given that (1) phosphate- and carbonate-bound oxygen in biopapatite are build up with oxygen atoms from the same body water source (cogenesis) and (2) metabolic reactions among mammals are occurring at a constant temperature (~37°C), *in vivo* $\delta^{18}O_C$ and $\delta^{18}O_P$ are in linear equilibrium. This relation has been calculated by empirical measurement and is considered to be (Iacumin *et al.*, 1996):

$$\delta^{18}O_P = 0.98 \times \delta^{18}O_C - 8.5 \qquad (n=31;\ r^2=0.98) \qquad \textbf{[Eq. 4.2]}$$

the 8.5 ‰ difference reflecting the different global fractionation factors between the two metabolic routes from the body water to bioapatite phosphate and carbonate groups (figure 4-3; Bryant *et al.,* 1996; Iacumin *et al.*, 1996; Lee-Thorp, 2000).

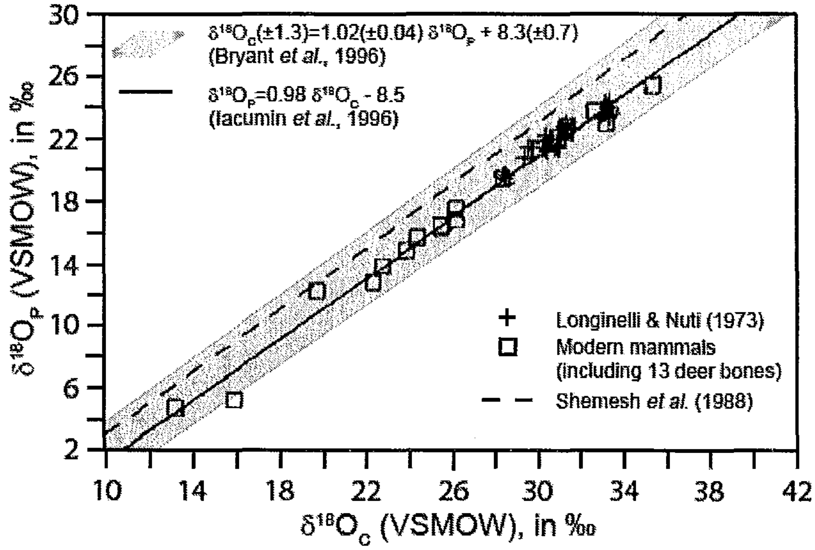

Figure 4-3. Relationship between $\delta^{18}O_P$ and $\delta^{18}O_C$ in several samples of modern mammal bioapatite (teeth and bone). The solid line is the best fit ($n=31$; $r^2=0.98$). The $\delta^{18}O$ values of modern carbonate shells are also shown (Longinelli & Nuti, 1973), along with the calculated straight line from geological calcite-apatite equation at 37°C calibrated by Shemesh *et al.* (1988). The shaded area corresponds to the accepted range of deviation from the equilibrium line in this study (Bryant *et al.*, 1996).

Modified, after Iacumin *et al.* (1996).

Given that phosphate-bounded oxygen is less sensitive to chemical weathering than carbonate-bound oxygen (because of the stronger P-O chemical bonds than C-O bonds; Longinelli, 1984; Kohn *et al.*, 1999), it has been suggested that this linear relationship between $\delta^{18}O_C$ and $\delta^{18}O_P$ could be used as a test of diagenetic alteration of skeletal remains (e.g.: Kolodny & Luz, 1991; Iacumin *et al.*, 1996; Bryant *et al.*, 1996). Chemical remodelling is thus expected to affect preferentially the carbonate groups in bioapatite, so diagenetically altered bones are expected to show deviation from the theoretical line defined by equation [4.2].

In the present study, it has been decided arbitrarily to set the limits for a maximum accepted range of deviation from the expected equilibrium line, by following Bryant *et al.* (1996). This range, indicated in equation [4.3], is considered here to take into account the uncertainties related to isotopic measurements (see Chapter 6). The corresponding correlation equation is:

$$\delta^{18}O_C(\pm 1.3) = 1.02(\pm 0.04) \times \delta^{18}O_P + 8.3(\pm 0.7) \qquad (n=42, r^2=0{,}99) \qquad \textbf{[Eq. 4.3]}$$

The acceptable range of $\delta^{18}O_C$ variations with respect to the linear equilibrium with $\delta^{18}O_P$ is represented by the shaded area shown on figure 4-3. It will be thus considered that the values falling outside this range are considered as diagenetically altered, and bones showing such relation between $\delta^{18}O_C$ and $\delta^{18}O_P$ will not be included in the reconstruction of past climate in the Maya region.

4.3.3) Infrared spectrometry

The crystallinity (the degree of order and/or substitution within the crystal lattice and the correlated crystal size; refer to Chapter 2, part 2.4.3), can be estimated by Fourier-Transform Infra-Red (FTIR) spectrometry.

To perform FTIR spectrometry, ~2 mg of bone powder is thoroughly mixed with ~150 mg of potassium bromide (KBr), the resulting powder being dried overnight (to remove possible atmospheric water vapour contamination) and loaded into a Carver™ hand press (model 3853-0) under 10 tons of pressure, to obtain a pellet of approximately 1 cm diameter and 1 mm thick (pelletization). KBr is the most frequent material used to hold solid samples, because of its transparency at mid-infrared frequencies. The pellet is then loaded into the chamber of the IR spectrometer (Thermo Scientific Nicolet™ model 5 PC; resolution: 4 cm^{-1}, or 0.025 μm) where a beam of mid-infrared light is directed onto the pellet and then recorded.

The principles of FTIR spectrometry, the measurement methods for crystallinity, the assessment of carbonate content, as well as the detection of exogenous mineral forms in bone bioapatite are presented hereafter.

4.3.3.1) Principle

In the FTIR spectra (mid-infrared, wavenumbers ranging from 400 to 4000 cm^{-1}, corresponding to wavelengths from 25 μm to 2.5 μm, respectively), associated photon energies are not large enough to reach electronic excited states. However, some wavelengths have sufficient energy to promote covalently bonded atoms or groups of atoms to excited vibrational states. Those specific wavelengths are quantized vibrational frequencies, affecting chemical bonds in two main ways: a bond stretching or a bond bending (figure 4-4). In addition to those two major vibrational modes, more complex ones can occur, such as scissoring, rocking, wagging or twisting modes, arising from combinations of bond bending and/or stretching in adjacent portions of the molecules.

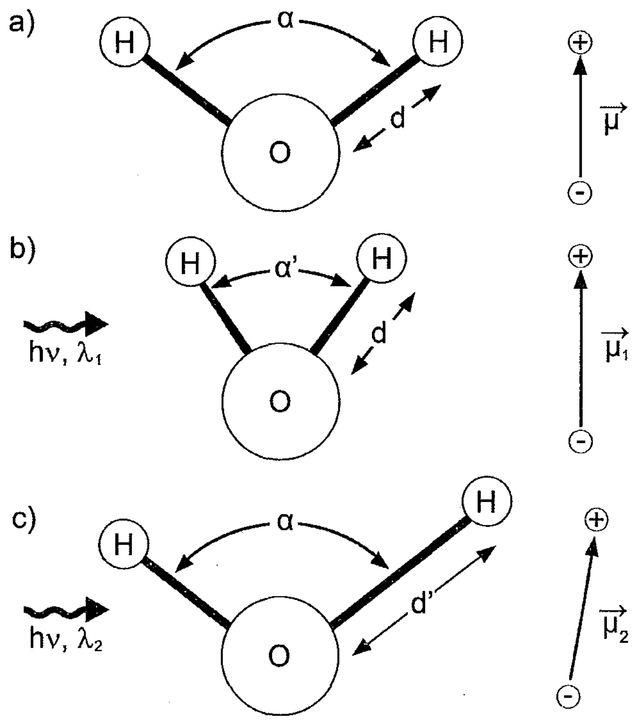

Figure 4-4. Schematic representation of the effects induced by infrared light irradiation (hν) of a water molecule (H_2O).

(a) In the case of an undistorted water molecule, the angle formed by the two O-H bonds is α (~104°), the distance between the oxygen atom and the hydrogen atoms is d (~96 pm), and the dipole moment (~6.2×10^{-30} C.m) of the molecule is represented by the vector $\vec{\mu}$ pointing towards the positive pole;

(b) At certain wavelengths (e.g. λ_1), the energy provided by the infrared beam provokes a bond bending, leading (in that example) to a modification of the angle between the two O-H bonds ($\alpha' \neq \alpha$);

(c) At some other wavelengths (e.g. λ_2), the incoming energy induces a bond stretching ($d' \neq d$), that can be either symmetrical or antisymmetrical.

Those vibrational modes are FTIR-active (*i.e.* provoking beam absorption and thus detectable) when irradiation results in a modification of the global dipole moment of the molecule (*i.e.* when $\vec{\mu}_1 \neq \vec{\mu}$ or $\vec{\mu}_2 \neq \vec{\mu}$);

The recorded interferogram (signature of infrared beam absorption by the pellet) is converted into an infrared spectrum by Fourrier Transform algorithms (Thermo Scientific™ OMNIC software, version 7.2) giving sample's beam absorbance per wavelength (figure 4-5). The absorbance bands (or peaks) are usually described as "strong" or "weak" and "broad" or "sharp". The main advantage of FTIR spectrometry is the acquisition of absorbance peaks at a broad range of wavelengths in one single quick measurement, reducing considerably the time/cost of experimentation.

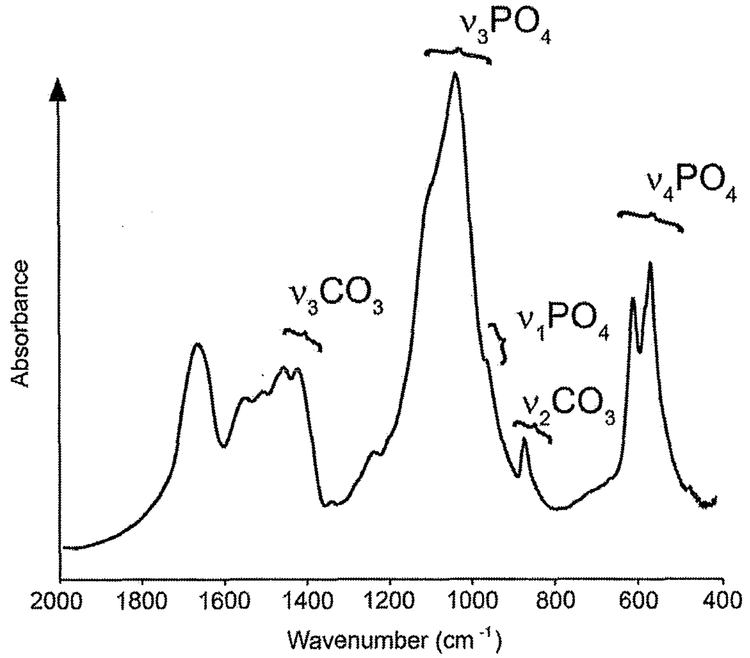

Figure 4-5. Typical FTIR spectrum obtained on fresh bone sample, giving the absorbance per wavenumber. Only the range of 400 to 2000 cm^{-1} and the main absorbance domains due to bioapatite crystallographic structure are shown (as mentioned in the text).

In the end, it is the molecular structure, *i.e.* the presence of specific functional groups (e.g.: PO_4, CO_3), as well as their environment, that determines the vibrational state of chemical bonds. In other words, the molecular structure determines which wavelengths will be transmitted and which ones will be absorbed (Sponheimer & Lee-Thorp, 1999; Surovell & Stiner, 2001). For example, calcite and aragonite (same chemical composition $CaCO_3$) will show distinct FTIR spectra because they are structurally dissimilar: in aragonite, each oxygen atom is bonded to three calcium atoms instead of two in calcite (Sponheimer & Lee-Thorp, 1999).

Indeed, FTIR spectra of molecules (or functional groups) with more than a few atoms are hardly decipherable. However, the presence of certain functional groups can be detected (*functional group analysis*) and even if the exact nature of each vibration is not known, FTIR spectroscopy can be used as a reliable tool for qualitative analysis. In addition, the intensity of absorbance is also proportional to the concentration of the absorbing molecule (or functional group) in the sample, allowing quantitative analysis (e.g.: Sponheimer & Lee-Thorp, 1999).

4.3.3.2) Crystallinity Index

FTIR spectrometry can be used to indirectly assess the crystallographic structure of the bone mineral. Actually, the effects of the environment surrounding the detected functional groups on their bonds' vibrational modes are quantifiable (Sponheimer & Lee-Thorp, 1999).

During deer's life, poorly crystalline bone apatite is formed at body temperature (~37°C), and is also constantly turning over (refer to Chapter 2, part 2.3.1). The kinetic factors are then predominant in the determining of the physical and chemical properties of bone apatite crystallites. Once removed from *in vivo* crystal-growth inhibitors, bone apatite has the potential to spontaneously recrystallize in a more crystalline form (more thermodynamically stable), resulting in increased mean crystal size (Trueman *et al.*, 2008). A higher crystallinity can also be due to a selective dissolution of the more soluble, less ordered crystals (Wright & Schwarcz, 1996). In both cases, there is a sign of a *post mortem* chemical remodelling.

Bone crystallinity quantification is derived from the pioneer work of Termine & Posner (1966), based on a particular vibrational mode of orthophosphate group (PO_4). In the case of the free undistorted orthophosphate ion (PO_4^{3-}, regular tetrahedron), two vibrational modes are FTIR-active in the so-called v_3-PO_4 domain (absorbance peak at 1017 cm^{-1}) and v_4-PO_4 domain (peak at 567 cm^{-1}; Elliott, 2002). In a crystal lattice, the vibrational domains of orthophosphate (as a functional group) are slightly different (figure 4-5). In geological apatite for example, the main absorbance peak of v_3-PO_4 domain appears at ~1040 cm^{-1} (Shemesh, 1990).

Termine & Posner work focused on the triply degenerate (*i.e.* three possible vibrational configurations for the same energy state) anti-symmetric bending vibration of the orthophosphate group. In apatite, this vibrational state absorbs infrared radiations at wavenumbers ranging from ~500 to ~600 cm^{-1} (in the v_4-PO_4 domain; figure 4-5). This absorption is detectable in both experimentally synthesized amorphous (non-crystalline) calcium phosphate and highly crystalline geological apatite (Shemesh, 1990). Using known concentrations of those two materials, Termine & Posner have calibrated a "percent crystallinity" (PC), reflecting the peak-splitting function, calculated as the ratio of the areas above and below the double peak detected in the v_4-PO_4

domain (figure 4-6a). The more crystalline the apatite is, the more those two peaks are narrow, due to the effects of the anisotropic electric field found in crystalline apatite, splitting the degeneracy of this absorption band into a well-defined doublet (Shemesh, 1990). In poorly crystalline apatite, each PO_4 group has a slightly different environment compared to another (refer also to Chapter 2, figure 2-5), and consequently the lattice has a less regular pattern of internal electric field. This lesser degree of anisotropy faintly affects the vibrational state of each PO_4 group, and results in a more "blurry" signal, betrayed by broader, thus more overlapping peaks.

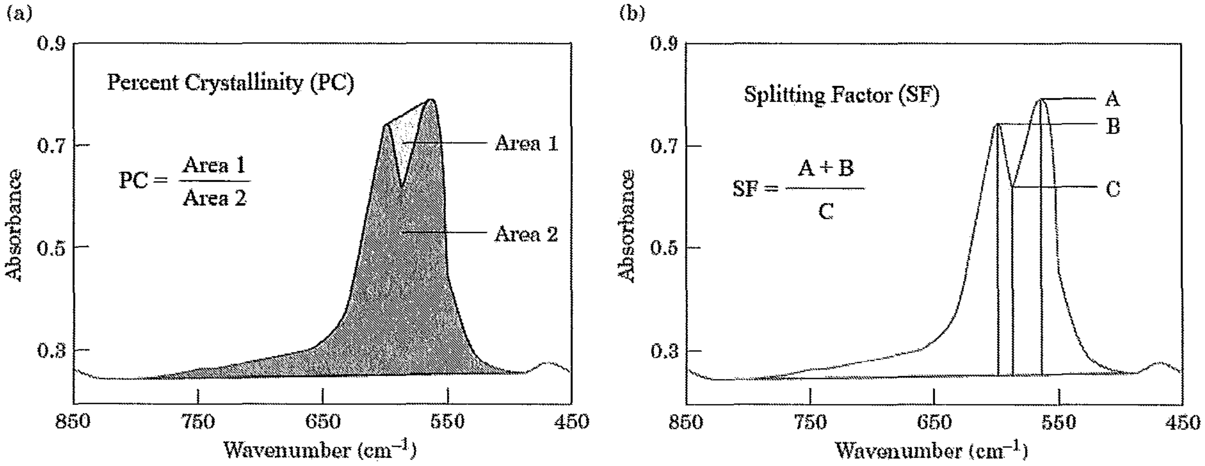

Figure 4-6. Two methods to calculate the crystallinity index of a bioapatite sample: **(a)** Percent Crystallinity (PC) as defined by Shemesh (1990) and **(b)** Splitting Factor (SF; e.g.: Wright & Schwarcz, 1996). Modified after Surovell & Stiner (2001).

Still based on Termine & Posner findings, another way of defining the peak-splitting function, known as the Splitting Factor (SF), has been developed. The SF is calculated by summing the heights of the ~563 cm^{-1} and ~603cm^{-1} peaks of the v_4-PO_4 domain and dividing this sum by the height of the lowest point between them (the valley situated at ~590 cm^{-1}), all heights measured from a baseline drawn approximately from 495 to 750 cm^{-1} (figure 4-6b; Shemesh, 1990; Weiner & Bar-Yosef, 1990; Wright & Schwarcz, 1996). The SF is now the most commonly used Crystallinity Index (CI) in apatite FTIR spectrometry and is therefore used in the present work to quantify bone's crystallinity. In the literature, as in this paper, CI is very often used as a synonym of SF. Ultimately, it can be added that in the recent times, some researchers considered that the SF can be used as a direct way to measure the mean crystal length (Trueman *et al.*, 2004):

$$Mean\ crystal\ length\ (in\ nm) = \frac{SF - 0.822}{0.048} \qquad \textbf{[Eq. 4.4]}$$

It is then considered that the oxygen isotopic composition of archaeological bone presenting a relatively high degree of crystallinity has been modified, and is then no longer usable for paleoclimatic reconstructions (as clearly seen on figure 4-1 above). Usual ranges of values of obtained CI indexes will be presented in Chapter 5 (part 5.3.2), and their reliability discussed in Chapter 6.

4.3.3.3) Carbonate content

As mentioned is Chapter 2 (part 2.4.4), bone apatite contains approximately 7 wt.% carbonate (CO_3), that can theoretically be found in the lattice at two different sites: replacing (1) an hydroxyl group (A-type substitution) or (2) a phosphate group (B-type substitution).

Three normal vibrational modes are FTIR-active in the case of a free (undistorted) carbonate ion (CO_3^{2-}, trigonal and planar): the ν_2-CO_3 domain (peak at 879 cm^{-1}), the ν_3-CO_3 domain (peak at 1415 cm^{-1}) and the ν_4-CO_3 domain (peak at 680 cm^{-1}), all corresponding to the transition moment in the plane of the ion (Elliott, 2002). ν_3-CO_3 and ν_2-CO_3 are the strongest and next strongest bands of absorption, but the ν_4-CO_3 vibrational mode has never been observed in any type of bioapatite (see figure 4-5; Elliott, 2002). However, the presence of carbonate groups in the bioapatite lattice is clearly and uniquely recognizable in the distinctive peaks for C-O vibrations in the IR spectra of bone and enamel (Wopenka & Pasteris, 2005).

Given that B-type substitutions affect the degree of crystallinity of the crystal lattice (Elliott, 2002; Wopenka & Pasteris, 2005; refer also to Chapter 2, part 2.4.4), an examination of the carbonate content is another way to assess the crystallographic structure of archaeological bone. The carbonate content can be measured following two approaches: (1) an assessment of A-type *versus* B-type carbonate substitution or (2) the total carbonate content.

(1) A-type *versus* B-type carbonate substitution

The effects of B-type compared to A-type substitution on the sensitivity of bone apatite to diagenesis have to be carefully accounted for. In addition to a crystallinity change, B-type substitution also induces a higher solubility of apatite crystals, due to the weaker nature of Ca-CO_3 than the Ca-PO_4 bonds (Wright & Schwarcz, 1996; Elliott, 2002; Botha *et al.*, 2004). In fact, the higher solubility of carbonated apatite is exploited in the preparation of bone sample for $\delta^{18}O_C$ and $\delta^{13}C_{Bone}$ analyses: the use of buffered acetic acid (see part 4.2.2 above) is presumed to remove any secondary carbonate that could have been adsorbed or replaced diagenetically at the surface of bioapatite crystallites (Wright & Schwarcz, 1996).

As mentioned by Wopenka & Pasteris (2005), it is presumably based on the theoretical possibility of A-type and B-type substitution that multiple maxima in a complex band (peak splitting) was interpreted in terms of substitution site (A- or B-type) by LeGeros *et al.* (1969). In the ν_2-CO_3 domain, two absorbance peaks have been assigned to A- and B-type carbonate substitution, situated at 878 and 871 cm^{-1}, respectively (Rey *et al.*, 1991). Another weak band, seen at 866 cm^{-1} has been assigned to CO_3^{2-} ions in a labile environment (Rey *et al.*, 1989). According to Elliott (2002), a source of interference is the presence of a supplementary absorption band in the ν_2-CO_3 domain due to the stretching of the P-OH bond at 870 cm^{-1}. This interference, as well as the close proximity of the peaks, make the use of the peaks found in the ν_2-CO_3 domain challenging to get information from (those peaks are not even visible on figure 4-5).

It quickly appeared that the use of the ν_3-CO_3 domain was more consensual. Nevertheless, to evaluate the relative abundances of A- and B-type substitutions, several peaks have been used. Following Sponheimer & Lee-Thorp (1999) and Botha *et al.* (2004), the relative amount of B- to A-type substitution (BAI) is given by the ratio of the peak heights seen at 1415 and 1540 cm^{-1}. Rink & Schwarcz (1995) used the absorption bands at 1450 and 1465 cm^{-1} to observe change in

A-type and B-type carbonate content, respectively. Due to the proximity of the peaks chosen by Rink & Schwarcz, Sponheimer & Lee-Thorp (1999) argued that the overlapping of those two peaks, in addition to poorly-understood carbonate environment, precludes their use as a tool to measure the variation of the A-type to B-type carbonate ratio. Elliott (1994) has shown that when the relative amount of A-type carbonate is increasing, the absorbance value of the 1450 cm^{-1} peak is increasing more than the one at 1540 cm^{-1}. This would tend to prove that those two absorption bands are not originating from the same crystallographic structure (Sponheimer & Lee-Thorp, 1999). Sponheimer & Lee-Thorp (1999) state that a BAI augmentation characterizes fossilization, and they propose three mechanisms that could induce this change (individually or conjugated): (1) an exogenous carbonate incorporation at B-sites, (2) an endogenous A-type carbonate loss, and/or (3) an endogenous carbonate reorganization.

(2) Total carbonate content

It is now generally accepted that B-type substitution is largely predominant in biological apatite (e.g.: Wright & Schwarcz, 1996). According to some researchers, the plausibility of A-type substitution is even decreasingly accepted (Elliott, 2002; Wopenka & Pasteris, 2005). In addition to substitution type in the crystal lattice, comes the problem of adsorbed carbonate ions. Because of the high surface area and high cation exchange capacity (high sorption coefficient) of bone apatite crystallites, it is currently thought that a significant proportion of carbonate groups is labile or more reactive, and probably represents ions adsorbed onto crystal surface (Wright & Schwarcz, 1996; Glimcher, 2006; Trueman *et al.*, 2008). It is even believed that some ionic PO_4^{3-} groups could also be labile (Glimcher, 2006).

Given that B-type substitution is the major type of substitution, along with the uncertainties about A-type substitution, three major methods have been used to track the overall carbonate content of bioapatite:

(1) *The C/P.* To measure the carbonate content, Wright & Schwarcz (1996) used the ratio between the absorbance of the CO_3 peak at ~1420 cm^{-1} in the ν_3-CO_3 domain and the main peak of the ν_3-PO_4 domain, at 1035 cm^{-1} (see figure 4-5). The use of the ν_3-PO_4 domain peak was preferred to the ν_4-PO_4 domain one, to avoid any interference with the peak splitting effect of a

possible crystallinity increase (Wright & Schwarcz, 1996). This relation has been checked by manometric measurement of the CO_2 volume liberated during the reaction between bone powder and orthophoshoric acid. Interestingly, CI is reported to be negatively correlated with C/P (n=33; $r^2 = 0.925$), showing that the carbonate content accounts for a substantial amount of the variability in crystallinity (Wright & Schwarcz, 1996).

(2) *The BPI.* The relative amount of B-type carbonate to phosphate (BPI) is calculated by Sponheimer & Lee-Thorp (1999) and Botha *et al.* (2004) by dividing the ~1420 cm^{-1} peak by the 605 cm^{-1} peak (one of the doublet of the v_4-PO_4 domain; figures 4-5).

(3) *The TCC.* The Total Carbonate Content (TCC) is a variant version of the two methods presented above that has been used by Pucéat *et al.* (2004). TCC is calculated using the ratio of intensities of the two strongest carbonate peaks (~1460 and ~1420 cm^{-1}, i.e. the doublet of the v_3-CO_3 domain) and the two phosphate peaks at ~603 and ~563 cm^{-1} (the doublet of the v_4-PO_4 domain), on the basis of a straight baseline drawn from 500 to 2000 cm^{-1} (figure 4-7).

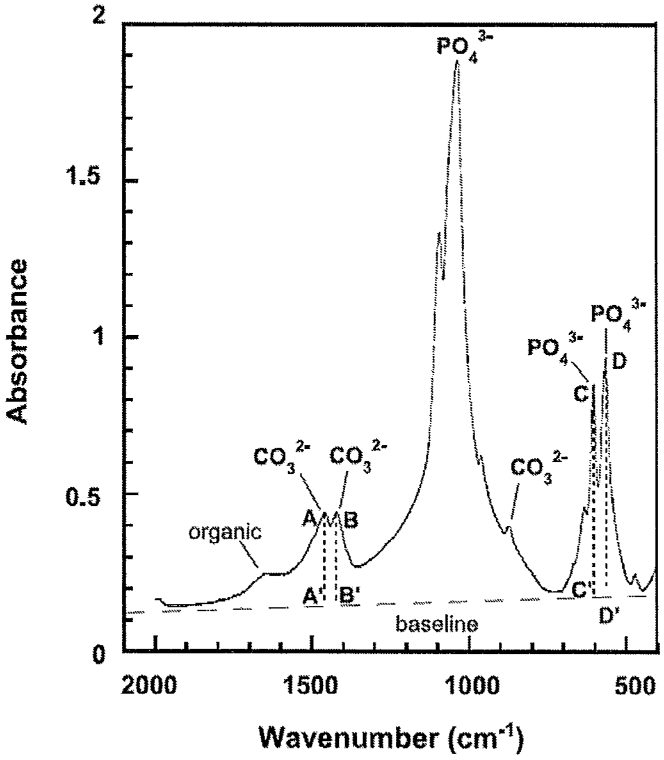

Figure 4-7. Method used by Pucéat *et al.* (2004) to measure Total Carbonate Content. TCC = [AA'+BB']/[CC'+DD']. Spectrum obtained on fossil fish tooth enamel. From Pucéat *et al.* (2004).

However, some researchers have used the proportion of A-type carbonate relative to phosphate (API) as an indicator of diagenesis. For example, Trueman *et al.* (2008) used the ratio of bands intensities at 1450 cm^{-1} and 605 cm^{-1}. Their results tend to show that a decrease in API values is correlated with an increased of the CI value.

The indicators of diagenesis based on carbonate content presented above have been far less used than the Crystallinity Index to assess diagenesis, but the corresponding indexes, as well as ranges obtained by several studies, will be presented in Chapter 5 (part 5.3.2) and their reliability will be discussed in Chapter 6.

4.3.3.4) Other mineral forms

During diagenetic processes, bioapatite can possibly re-crystallize in more stable mineral forms such as calcite or francolite: in that case, their presence can be simply checked, betrayed by the occurrence of peaks at 711 and 1096 cm^{-1}, respectively (Sponheimer & Lee-Thorp, 1999). As a consequence, bone samples showing such peaks are then screened out, and will not be included in the reconstruction of past climate in the Yucatán peninsula.

The presence of fluorine (F) in the crystal lattice can also be detected indirectly through the intensity ratio of the peak doublet seen in the ν_4-PO4 domain (see figure 4-5; Okazaki, 1983; Shemesh, 1990). In the case of F-containing apatites such as francolite, the intensity of the ~605 cm^{-1} peak increases relative to the one of the ~575 cm^{-1} peak, while F-deficient apatites tend to show an opposite pattern (more intense absorption at ~575 cm^{-1}; Trueman *et al.*, 2008). Even if fluorine inclusion in the apatite lattice induces a lower solubility (and thus a greater stability; Berna *et al.*, 2004), this indirect approach will not be considered, because of the relative lack of studies mentioning this method on bone bioapatite.

References

Bassett D., K.G. MacLeod, J.F. Miller, R.L. Ethington (2007) – Oxygen isotopic composition of biogenic phosphate and the temperature of early Ordovician seawater. *Palaios* 22,98-103

Berna F., A. Matthews, S. Weiner (2004) - Solubilities of bone mineral from archaeological sites: the recrystallization window. *Journal of Archaeological Science* 31, (7): 867-882.

Botha J., J. Lee-Thorp, M. Sponheimer (2004) - An examination of Triassic cynodont tooth enamel chemistry using Fourier Transform Infrared spectroscopy. *Calcified Tissue International* 74, (2): 162-169.

Bryant J.D. & P.N. Froelich (1995) - A Model of Oxygen-Isotope Fractionation in Body-Water of Large Mammals. *Geochimica et Cosmochimica Acta* 59, (21):4523-4537.

Bryant J.D., P. Koch, P.N. Froelich, W.J. Showers, B.J. Genna (1996) – Oxygen isotope partitioning between phosphate and carbonate in mammalian apatite. *Geochimica et Cosmochimica Acta* 60, 5145-5148.

Coplen T.B. (1996) - New guidelines for reporting stable hydrogen, carbon and oxygen isotope-ratio data. *Geochimica et Cosmochimica Acta* 60, 3359–3360.

Dettman D.L., M.J. Kohn, J. Quade, F.J. Ryerson, T.P. Ojha, S. Hamidullah (2001) - Seasonal stable isotope evidence for a strong Asian monsoon throughout the past 10.7 m.y. *Geology* 29, 31-34.

Elliott J.C. (1994) - Structure and Chemistry of the Apatites and Other Calcium Orthophosphates, Elsevier, Amsterdam.

Elliott J.C. (2002) - Calcium posphate biominerals. Phosphates - Geochemical, Geobiological, And Materials Importance. M. J. Kohn, J. Rakovan and J. M. Hughes. Washington DC, Mineral Society of America. **48:** 427-453.

Faller L.D. & G.A. Elgavish (1984) - Catalysis of oxygen-18 exchange between inorganic phosphate and water by the gastric H,K-ATPase. *Biochemistry 23, 6584-6590.*

Fricke H.C. & J.R. O'neil (1996) - Inter- and intratooth variation in the oxygen isotope composition of mammalian tooth enamel phosphate: Implications for palaeoclimatological and palaeobiological research. *Palaeogeography Palaeoclimatology Palaeoecology* 126, (1-2):91-99.

Glimcher M.J. (2006) - Bone: nature of the calcium phosphate crystals and cellular, structural, and physical chemical mechanisms in their formation. *Reviews in Mineralogy & Geochemistry* 64, 223-282.

Hedges R.E.M. (2002) - Bone diagenesis: An overview of processes. *Archaeometry* 44, 319-328.

Iacumin P., H. Bocherens, A. Mariotti, A. Longinelli (1996) - Oxygen isotope analyses of co-existing carbonate and phosphate in biogenic apatite: a way to monitor diagenetic alteration of bone phosphate? *Earth and Planetary Science Letters* 142, 1-6.

Koch P.L., N. Tuross, M.L. Fogel (1997) - The effects of sample treatment and diagenesis on the isotopic integrity of carbonate in biogenic hydroxylapatite. *Journal of Archaeological Science* 24, 417–429.

Kohn M.J., M.J. Schoeninger, W.W. Barker (1999) – Altered states: Effects of diagenesis on fossil tooth chemistry. *Geochimica et Cosmochimica Acta* 63, (18):2737-2747.

Kolodny Y. & B. Luz (1991) - Oxygen isotopes in phosphates of fossil fish: Devonian to recent. In Stable Isotope Geochemistry: A Tribute to Samuel Epstein. H.P. Taylor, J.R. O'Neil, & I.R. Kaplan, (Eds.). Special Publication No. 3, The Geochemical Society.

Lee-Thorp J.A. (2000) – Preservation of biogenic carbon isotopic signals in Plio-Pleistocene bone and tooth mineral. In Biogeochemical approaches to paleodietary analysis. Ambrose & Katzenberg (Eds). Kluwer Academic/Plenum Publishers. New York.

LeGeros R.Z., O.R. Trautz, E. Klein, LeGeros J.P. (1969) – Two types of carbonate substitution in the apatite structure. *Experientia* 25, (1):5-7.

Longinelli A. & S. Nuti (1973) - Revised phosphate-water isotopic temperature. Scale. *Earth & Planetary Science Letters* 19, 373-376.

Longinelli A. (1984) - Oxygen isotopes in mammal bone phosphate: a new tool for paleohydrological and paleoclimatological research? *Geochimica et Cosmochimica Acta* 48, 385-390.

Luz B., Y. Kolodny, J. Kovach (1984) - Oxygen isotope variations in phosphate of biogenic apatites, 111. Conodonts. *Earth & Planetary Science Letters* 69, 255-262.

Munro L.E., F.J. Longstaffe, C.D. White (2007) - Burning and boiling of modern deer bone: Effects on crystallinity and oxygen isotope composition of bioapatite phosphate. *Palaeogeography, Palaeoclimatology, Palaeoecology* 249, 90-102.

Munro L.E., F.J. Longstaffe, C.D. White (2008) - Effects of heating on the carbon and oxygen-isotope compositions of structural carbonate in bioapatite from modern deer bone. *Palaeogeography, Palaeoclimatology, Palaeoecology* 266, 142-150.

Nicholson R.A. (1993) - A Morphological Investigation of Burnt Animal Bone and an Evaluation of Its Utility in Archaeology. *Journal of Archaeological Science* 20, (4): 411-428.

Okazaki M. (1983) – F-CO_3^{2-} interaction in IR spectra of fluorinated CO_3-Apatites. *Calcified Tissue international* 35, 78-81.

Pucéat E., B. Reynard, C. Lécuyer (2004) - Can crystallinity be used to determine the degree of chemical alteration of biogenic apatites? *Chemical Geology* 205, 83– 97.

Rey C., B. Collins, T. Goehl, I.R. Dickson, M.J. Glimcher (1989) - The Carbonate Environment in Bone-Mineral - a Resolution-Enhanced Fourier-Transform Infrared-Spectroscopy Study. *Calcified Tissue International* 45, (3): 157-164.

Rey C., V. Renugopalakrishnan, B. Collins, M.J. Glimcher (1991) - Fourier-Transform Infrared Spectroscopic Study of the Carbonate Ions in Bone-Mineral During Aging. *Calcified Tissue International* 49, (4): 251-258.

Rink W. J. & H.P. Schwarcz (1995) - Tests for Diagenesis in Tooth Enamel - Esr Dating Signals and Carbonate Contents. *Journal of Archaeological Science* 22, (2): 251-255.

Shemesh A., Y. Kolodny, B. Luz (1988) - Isotope geochemistry of oxygen and carbon in phosphate and carbonate of phosphorite francolite. *Geochimica et Cosmochimica Acta* 52, 2565-2572.

Shemesh A. (1990) - Crystallinity and diagenesis of sedimentary apatites. *Geochimica Et Cosmochimica Acta* 54, (9): 2433-2438.

Shipman P., G. Foster, M. Schoeninger (1984) - Burnt Bones and Teeth - an Experimental-Study of Color, Morphology, Crystal-Structure and Shrinkage. *Journal of Archaeological Science* 11, (4): 307-325.

Silverman D.N. (1982) - Carbonic anhydrase: Oxygen-18 exchange catalyzed by an enzyme with rate-contributing proton-transfer steps. *Methods in Enzymology* 87, 732-752.

Sponheimer M. & J.A. Lee-Thorp (1999) - Alteration of enamel carbonate environments during fossilization. *Journal of Archaeological Science* 26, (2): 143-150.

Surovell T.A. & M.C. Stiner (2001) - Standardizing infra-red measures of bone mineral crystallinity: An experimental approach. *Journal of Archaeological Science* 28, (6): 633-642.

Termine J.D. & A.S. Posner (1966) - Infrared analysis of rat bone: age dependency of amorphous and crystalline mineral fractions. *Science* 153, 1523–1525.

Trueman C.N., A.K. Behrensmeyer, N. Tuross, S. Weiner (2004) - Mineralogical and compositional changes in bones exposed on soil surfaces in Amboseli National Park, Kenya: diagenetic mechanisms and the role of sediment pore fluids. *Journal of Archaeological Science* 31, (6): 721-739.

Trueman C.N., K. Privat, J. Field (2008) - Why do crystallinity values fail to predict the extent of diagenetic alteration of bone mineral? *Palaeogeography Palaeoclimatology Palaeoecology* 266, (3-4): 160-167.

Weiner S. & O. Bar-Yosef (1990) - States of preservation of bones from prehistoric sites in the Near East: a survey. *Journal of Archaeological Science* 17, 187-196.

Wopenka B. & J.D. Pasteris (2005) - A mineralogical perspective on the apatite in bone. *Materials Science & Engineering C-Biomimetic and Supramolecular Systems* 25, (2): 131-143.

Wright L.E. & H.P. Schwarcz (1996) - Infrared and isotopic evidence for diagenesis of bone apatite at Dos Pilas, Guatemala: palaeodietary implications. *Journal of Archaeological Science* 23, 933-944.

Chapter 5 - Results

In this chapter, the results from isotopic analyses and infra-red spectroscopy (FTIR) are presented and succinctly described. The precision of $\delta^{18}O_P$, $\delta^{18}O_C$ and $\delta^{13}C_{Bone}$ measurements is first detailed, followed by the results showing intra-bone variability, obtained from the dataset acquired on doubly-sampled deer bones. The third part is concerned with the results from the diagenesis screening methods: the comparison $\delta^{18}O_P$-$\delta^{18}O_C$ and the different measures of FTIR indexes are expounded, and a comparison between the two methodologies is then presented. The last part finally summarizes $\delta^{18}O_P$, $\delta^{18}O_C$ and $\delta^{13}C_{Bone}$ variations through time at Lamanai, Motul de San José and Piedras Negras. All the results presented in this chapter will be discussed in Chapter 6.

5.1) Precision

The standards used to control the reproducibility of the Optima Gas Chromatograph-Isotope Ratio Mass Spectrometer (GC-IRMS) during $\delta^{18}O_C$ and $\delta^{13}C_{Bone}$ measurements were usual calcite ($CaCO_3$) standards (NBS-18 and NBS-19), with known carbon and oxygen isotopic compositions ($\delta^{13}C_{NBS\text{-}18} = -5.014$ ‰ V-PDB, $\delta^{18}O_{NBS\text{-}18} = 6.94$ ‰ V-SMOW, $\delta^{13}C_{NBS\text{-}19} = 1.95$ ‰ V-PDB and $\delta^{18}O_{NBS\text{-}19} = 33.13$ ‰ V-SMOW). 17 replicated measurements were equally distributed throughout the runs for each standard. The standards used to control the reproducibility of the Thermo Finnigan DeltaPlus GC-IRMS during $\delta^{18}O_P$ measurements were two types of benzoic acids (C_6H_5COOH; IAEA-601 and another internal standard), and USGS-35 (sodium nitrate, $NaNO_3$) with known oxygen isotopic compositions ($\delta^{18}O_{IAEA\text{-}601} = 23.3$ ‰ V-SMOW and $\delta^{18}O_{USGS\text{-}35} = 57.5$ ‰ V-SMOW). 42 and 10 replicated measurements were equally distributed during the runs for the benzoic acids and USGS-35, respectively.

A total of 98 bones were sampled, among which 24 were sampled on two different locations, leading to a total of 122 samples processed for $\delta^{13}C_{Bone}$, $\delta^{18}O_C$ and $\delta^{18}O_P$ measurements. Each measurement has been replicated three times for each sampled bone powder.

Table 5-1 summarizes the reproducibilities obtained on standards and samples for each set of isotopic measurement.

Table 5-1. Summary of the reproducibilities obtained during the different isotopic measurements. For deer bones samples, standard deviations σ were calculated from the three replications of each isotopic measurement. All standard deviations are given in ‰.

Measure	Standards			Deer bone samples				
	name	**σ**	**replicates**	**location**	**min σ**	**max σ**	**average σ**	**samples**
$\delta^{13}C_{Bone}$	NBS-18	0.2	17	LAM	0.04	0.2	0.2	15
	NBS-19	0.2	17	MSJ	0.03	1.0	0.3	14
				PN	<0.01	0.7	0.1	93
$\delta^{18}O_C$	NBS-18	0.4	17	LAM	0.2	0.9	0.4	15
	NBS-19	0.3	17	MSJ	0.1	1.0	0.5	14
				PN	0.02	1.2	0.4	93
$\delta^{18}O_P$	Benzoic acid	0.2	42	LAM	0.1	0.8	0.4	15
	USGS-35	1.0	10	MSJ	0.1	1.0	0.5	14
				PN	0.03	1.4	0.4	93

LAM: Lamanai; MSJ: Motul de San José; PN: Piedras Negras

The standard deviations (σ) obtained by several replications of isotopic measurements on the standards are defining the expected reproducibility of each set of measurements: they are thus no less than 0.2 ‰, 0.3 ‰ and 0.2 ‰ for $\delta^{13}C_{Bone}$, $\delta^{18}O_C$ and $\delta^{18}O_P$ measurements, respectively.

The average σ calculated from three replicated measurements, obtained on each of the 122 bone samples, are considered to match the expected reproducibility for $\delta^{13}C_{Bone}$ (average σ including the 122 samples is less than 0.2 ‰) and $\delta^{18}O_C$ measurements (σ = 0.4 ‰, all 122 samples included, equivalent to the σ-value of 0.4 ‰ obtained on NBS-18). However, in the case of $\delta^{18}O_P$ measurements on deer bone samples, the average reproducibility is quite dissimilar to the expected one (0.4 ‰ instead of 0.2 ‰).

The σ-values on each bone sample range from very low values (close to σ = 0 ‰ in the case of $\delta^{13}C_{Bone}$, $\delta^{18}O_C$ and $\delta^{18}O_P$ at PN, thus indicating almost a perfect reproducibility) to very high values (e.g. σ = ~1.4 ‰ in the case of $\delta^{18}O_P$ at PN, indicating a high degree of scatter during replicated measurements).

5.2) Intra-bone variability

Among the 98 bones analyzed in this study, 24 of them were considered large enough to be sampled at two different locations (2 from MSJ, 22 from PN). Figure 5-1 is presenting the dispersion of $\delta^{18}O_P$ relatively to $\delta^{18}O_C$ values for those deer bones sampled twice. The summary of intra-bone variability is presented in table 5-2.

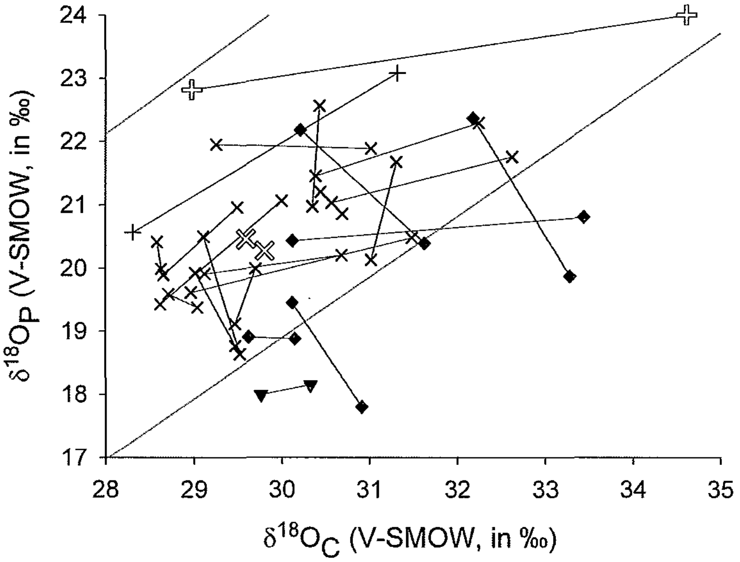

Figure 5-1. $\delta^{18}O_P$ *versus* $\delta^{18}O_C$ values for 24 deer bones sampled twice (2 from MSJ indicated by +, 22 from PN (indicated by ×, ◆ and ▼). Values from a same bone are linked by a line. The two sub-parallel grey lines are representing the relation $\delta^{18}O_C(\pm1.3) = 1.02(\pm0.04) \times \delta^{18}O_P + 8.3(\pm0.7)$; see text for further information.

Table 5-2. Summary of the intra-bone variability measured on 24 deer bones that were sampled twice, on two different locations. For each measurement ($\delta^{18}O_P$, $\delta^{18}O_C$ and $\delta^{13}C_{Bone}$), the average, minimum and maximum Δ-values are given, where Δ is the difference between the highest and the lowest value.

Group	n	average $\Delta^{18}O_P$	min $\Delta^{18}O_P$	max $\Delta^{18}O_P$	average $\Delta^{18}O_C$	min $\Delta^{18}O_C$	max $\Delta^{18}O_C$	average $\Delta^{13}C_{Bone}$	min $\Delta^{13}C_{Bone}$	max $\Delta^{13}C_{Bone}$
All	24	1.0	0.0	2.5	1.3	0.0	5.7	0.5	0.0	1.5
Inside(a)	18	1.0	0.1	2.5	1.3	0.0	5.7	0.5	0.1	1.2
Outside(b)	6	1.1	0.0	2.5	1.3	0.5	3.3	0.5	0.0	1.5

(a) *both duplicates are falling inside the accepted range described in Chapter 4, equation [4.3];*
(b) *one (or both) duplicate is falling outside this range*

All the cases are seen on figure 5-1: relatively low $\delta^{18}O_P$ difference ($\Delta^{18}O_P$) and high $\Delta^{18}O_C$ (e.g. duplicate indicated by a thick open +; 1.2 and 5.6 ‰, respectively), both low $\Delta^{18}O_P$ and $\Delta^{18}O_C$ (e.g. duplicate indicated by open ×; both 0.2 ‰), and intermediate cases.

No trend is observed as for the variability of $\delta^{18}O_P$ relatively to $\delta^{18}O_C$: for 12 bones, $\Delta^{18}O_P$ is higher than $\Delta^{18}O_C$, and inversely for the remaining 12. The two sub-parallel grey lines on figure 5-1 represent the accepted range for $\delta^{18}O_P$ variation relatively to $\delta^{18}O_C$ values in the case of non-diagenetically altered bones (refer to Chapter 4, equation [4.3], and part 5.3.1 below). Again, table 5-2 does not show a clear trend between bones for which both duplicates fall inside the accepted range and those from which one duplicate falls outside the range (or both in one case).

5.3) Diagenesis screening

Before using the measured isotopic values for past climate reconstructions in the Maya region, it is necessary to check possible *post-mortem* changes of bone chemical composition (refer to Chapter 4, part 4.3).

5.3.1) Comparison $\delta^{18}O_P$-$\delta^{18}O_C$

As stated in Chapter 4 (part 4.3.2), given the co-genesis of carbonate and phosphate groups in the bioapatite lattice from the same oxygen source (*i.e.* the body water), the linear relation between $\delta^{18}O_P$ and $\delta^{18}O_C$ can be used as an indicator of diagenesis. We decided in the present study to use the relation [$\delta^{18}O_C(\pm1.3) = 1.02(\pm0.04) \times \delta^{18}O_P + 8.3(\pm0.7)$] given by Bryant *et al.* (1996), to set up the limits for the accepted range of $\delta^{18}O_C$ variation with respect to $\delta^{18}O_P$ that a deer bone sample must show to be considered as non-diagenetically altered.

In the case of bones sampled twice, three configurations are observed: (1) both the duplicates fall outside this range (1 case, indicated by ▼ in figure 5-1), so the bone from which the duplicates are from has to be eliminated for further use; (2) both the duplicates fall inside the range (18 cases out of 24, indicated by × and ✚ in figure 5-1), so the average $\delta^{18}O_P$ and $\delta^{18}O_C$ values from the duplicates are then considered for further use; (3) one of the duplicate falls outside the range (5 cases, indicated by ◆ in figure 5-1), so that only the sample from which the couple $\delta^{18}O_P$-$\delta^{18}O_C$ falls inside the range is considered for further use. Once the values acquired on doubly-sampled bones were given the same weight as other samples (*i.e.* 1 instead of 2), a comparison of $\delta^{18}O_P$-$\delta^{18}O_C$ can be done again, including all the 97 remaining bones (*i.e.* 98 minus the doubly-sampled bone rejected).

The comparison of $\delta^{18}O_P$-$\delta^{18}O_C$ for the remaining 97 bones is presented in figure 5-2. It can be seen that almost all the samples fall inside the accepted range: 15 out of 15 for LAM, 11 out of 12 for MSJ and 67 out of 70 for PN. The four bones falling outside this range were then screened out, and will not be used for past climate reconstruction.

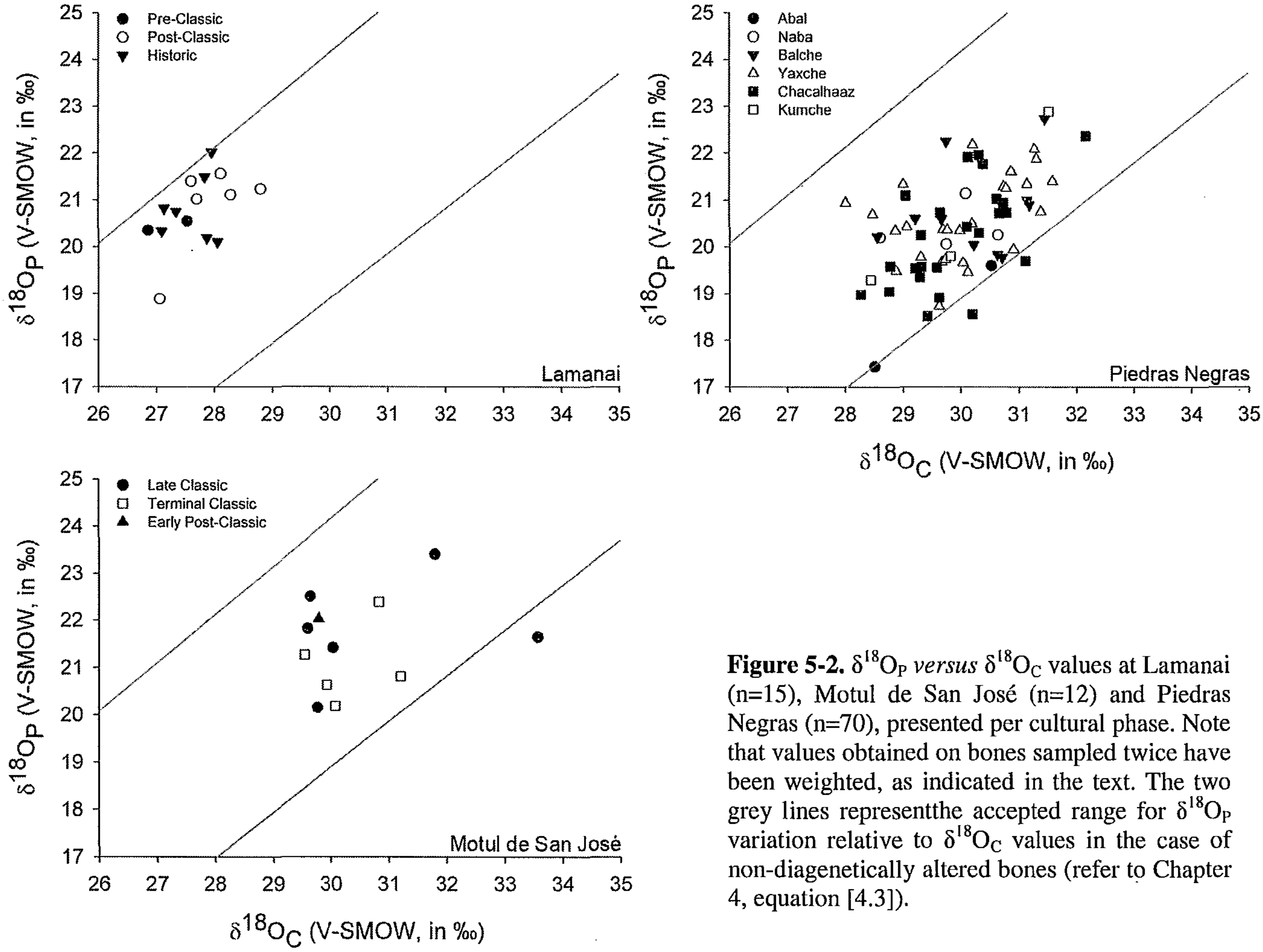

Figure 5-2. $\delta^{18}O_P$ *versus* $\delta^{18}O_C$ values at Lamanai (n=15), Motul de San José (n=12) and Piedras Negras (n=70), presented per cultural phase. Note that values obtained on bones sampled twice have been weighted, as indicated in the text. The two grey lines representthe accepted range for $\delta^{18}O_P$ variation relative to $\delta^{18}O_C$ values in the case of non-diagenetically altered bones (refer to Chapter 4, equation [4.3]).

5.3.2) FTIR spectroscopy

Among the 122 samples of bone powder, 97 of them were analyzed by FTIR spectroscopy. All the curves were automatically baseline-corrected before peak height measurements.

Each curve was first examined to detect the possible presence of secondary recrystallized mineral such as calcite or francolite (refer to Chapter 4, part 4.3.3.4). Only two samples exhibited the specific 711 cm^{-1} peak, caused by the presence of calcite (1 from LAM and 1 from MSJ). The presence of a peak at 711 cm^{-1}, in a zone where no peak is usually observed (refer to figure 4-5 in Chapter 4), is considered to reflect unequivocally the presence of calcite. The two samples showing this peak were thus screened out, and will not be used for past climate reconstruction.

The reproducibility of Crystallinity Index (CI) measurements by FTIR spectroscopy has first been tested. To perform those tests, a piece of approximately 1 cm^3 of modern (*i.e.* a few years old) cortical cow bone (femur), 1 cm^3 of fresh (a few months old) pig bone (long bone), and 1 cm^3 of archaeological charred deer bone (long bone) have been sampled, following the same procedure used to sample the archaeological deer bones (refer to Chapter 4, part 4.1). Four series of tests were conducted and are presented in table 5-3: (1) testing the effect of bone powder concentration in the pellet, by varying the ratio bone powder to potassium bromide (KBr; pellets 1-6); (2) testing the effect of pelletization, by preparing 3 pellets from the same charred deer bone powder, and measuring the CI twice on each of them (pellets 14-16); (3) testing the effect of the grinding intensity: two batches of bone fragments were ground separately using a cryo-crusher: the first has been ground during 5 cycles of 5 minutes, at a high rate (15 cpm), referred as "super grind" (pellets 7, 10 and 11), and the second has been ground during 3 cycles of 1 minute, at a low rate (5 cpm), referred as "low grind" (pellets 8, 12 and 13); and (4) testing the effect of grain size, by separation on cellulose filters of cow bone powder particles (ground following the normal program) with diameters ranging from 11 to 45 μm (pellet 9).

Table 5-3. Reproducibility testings for Crystallinity Index measurement by FTIR spectrometry

Pellet #	Bone	Proportion of bone powder (in %)	Grinding intensity	Other	Crystallinity Index(a)
1	cow	0.7	normal		2.8
2	cow	0.9	normal		2.9
3	cow	1.4	normal		2.8
4	cow	1.5	normal		2.8
5	cow	6.0	normal		2.9
6(b)	cow	1.4	normal	not dried	2.9
7	cow	1.3	super grind		2.8
8	cow	1.3	low grind		2.9
9	cow	1.3	normal	grain size	2.9
10	pig	1.3	super grind		3.1
11	pig	1.3	super grind		3.0
12	pig	1.3	low grind		3.1
13	pig	1.3	low grind		3.0
14	deer (charred)	1.3	normal	replicate 1	3.3
				replicate 2	3.3
15	deer (charred)	1.3	normal	replicate 1	3.2
				replicate 2	3.2
16	deer (charred)	1.3	normal	replicate 1	3.0
				replicate 2	3.0

(a) *CI is calculated by summing the heights of the ~563 cm^{-1} and ~603cm^{-1} peaks and dividing this sum by the height of the lowest point between them (the valley situated at ~590 cm^{-1}), all heights are calculated using a baseline drawn from approximately 750 and 500 cm^{-1}*
(b) *in this experiment, the bone hasn't been dried in the drying cabinet overnight prior to the analysis*

The CIs measured on pellets 1 to 5 show that the proportion of bone powder in the pellet does not strongly affect the CI. Pellet 6 shows that the cow bone was totally dry at the time it has been sampled. There is no noticeable difference between the two grinding strategies, and neither is there an effect when the bone powder is sifted to select a certain grain size (pellets 7 to 13). The position of the pellet on the sample holder inside the infra-red spectrometer does not impact the obtained CI value (pellets 14 to 16). One must notice that the CI values obtained on the fresh pig bone are close to those obtained on the charred deer bone. In the end, we estimate the reproducibility (σ) of CI measurement by FTIR spectroscopy to be ± 0.15.

Similar tests were conducted for FTIR indexes of carbonate content (C/P, BPI and TCC; refer to Chapter 4, part 4.3.3.3). The presentation of all the FTIR indexes (CI, C/P, BPI and TCC) obtained on the 95 remaining deer bone samples (97 minus the two samples screened out because of calcite presence) are presented in table 5-4, and comparative values are indicated.

Table 5-4. Ranges and average values of Crystallinity Index (CI), Carbonate/Phosphate ratio (C/P), amount of B-type carbonate to phosphate (BPI) and total carbonate content (TCC) measured by FTIR spectrometry on archaeological deer bones (n=95) and fresh bones (n=2). All the comparative values indicated were obtained on mammal bioapatite.

Index	Name	Material	Age (a)	Value range (b)	Average	σ	Source
Crystallinity Index	CI	enamel	M	3.5–3.8		± 0.1	Sponheimer & Lee-Thorp, 1999
		enamel	A	3.4–4.1			
		bone	M	3.0–3.6		± 0.1	Wright & Schwarcz, 1996
		bone	A	3.8–4.2			
		bone	A	2.8–4.0		± 0.15	Sillen & Parkington, 1996
		bone	A, F	2.8–3.8		± 0.05	Surovell & Stiner, 2001
		bone	F(c)	3.6–6.3		± 0.4	
		bone	M	2.8–3.3		± 0.05	Trueman *et al.*, 2008
		bone	A	2.8–4.1		± 0.2	
		bone	F	2.6–2.9		± 0.1	Munro *et al.*, 2007
		bone	F(c)	3.0-4.3			
		bone	F	2.8-3.1	2.9	± 0.15	This study
		bone	A	2.6-3.6	3.1	± 0.15	
Carbonate content	C/P	bone	M	0.2–0.3		± 0.01	Wright & Schwarcz, 1996
		bone	A	0.1–0.2			
		bone	A	0.3-0.7	0.4	± 0.05	This study
Relative B-type carbonate to phosphate amount	BPI	bone	M	0.6–0.8		n.a.	Trueman *et al.*, 2008
		bone	A	0.6–0.8			
		enamel	M	0.15–0.35		± 0.01	Sponheimer & Lee-Thorp, 1999
		enamel	A	0.20–0.35			
		bone	A	0.6-0.9	0.7	± 0.05	This study
Total carbonate content	TCC	bone	M	0.9		n.a.	Pucéat *et al.*, 2004
		bone	A	0.5-0.9	0.7	± 0.1	This study

(a) *the age of the samples has been arbitrarily divided in three categories: F = fresh bone (less than a few months old); M = modern (found in the wild on the ground or sampled long before spectroscopy, i.e. several months to several tenths of years old), A = archaeological or fossil (i.e. centuries to millions of years old);* (b) *values are indicative only;* (c) *fresh bone heated to temperatures superior to 500°C; n.a.: not available*

The ranges and reproducibility of the FTIR indexes we obtain are comparable to other studies, with the exception of the C/P, for which the average value (0.4) is somehow higher than data from Wright & Schwarcz (1996), where C/P measured on ancient bones ranges from 0.1 to 0.2 (table 5-4). The total carbonate content (TCC) indexes of the two bones previously screened (because of calcite; not included in table 5-4) were the only "abnormal" ones (*i.e.* indexes >1; see also figure 5-4 below) of the entire dataset, confirming the need of excluding them for further use.

5.3.3) Intra-bone variability of FTIR indexes

Among the 24 bones sampled twice, the duplicates from 15 of them were analyzed by FTIR spectroscopy and compared. The differences between each pair of samples from a same bone are summarized in table 5-5.

Table 5-5. Summary of intra-bone variability of FTIR indexes.

Index	All pairs (n=15)				One pair removed (n=14)		
	average Δ	min Δ	max Δ	σ	average Δ	max Δ	σ
CI	0.07	0.05	0.23	0.07	0.06	0.16	0.05
C/P	0.03	0.00	0.09	0.03	0.03	0.09	0.02
BPI	0.06	0.00	0.16	0.05	0.05	0.15	0.04
TCC	0.05	0.01	0.15	0.05	0.04	0.12	0.04

Δ = highest minus lowest value

The average intra-bone differences remain under the reproducibilities of CI, C/P and TCC measurements (i.e. < 0.15, 0.05 and 0.1, respectively), and is slightly higher for BPI index (0.06 compared to 0.05). However, a single pair of bone samples is responsible for all the maximum differences. Once removed from the dataset, the scatter of the Δ-values (σ) is significantly decreased for all indexes.

5.3.4) Correlation between FTIR indexes

The FTIR indexes obtained on the 95 samples were compared to each other and linear correlation coefficients have been calculated (figure 5-3). A very strong linear correlation between TCC and BPI (middle-right plot) is observed (r^2~0.97), and linear correlation between CI and C/P (top-left plot) is high (r^2~0.72). In the top-right plot (BPI against C/P), it can be seen that 9 samples are clearly not clustering along the regression line, showing relatively high C/P (2 from Lamanai, 1 from Motul de San José and 6 from PN). When those points are removed from the dataset, the correlation coefficients (r^2) between C/P against BPI and C/P against TCC are significantly increased (from 0.41 to 0.83 and from 0.42 to 0.82, respectively), but no significant change is observed as for other relations.

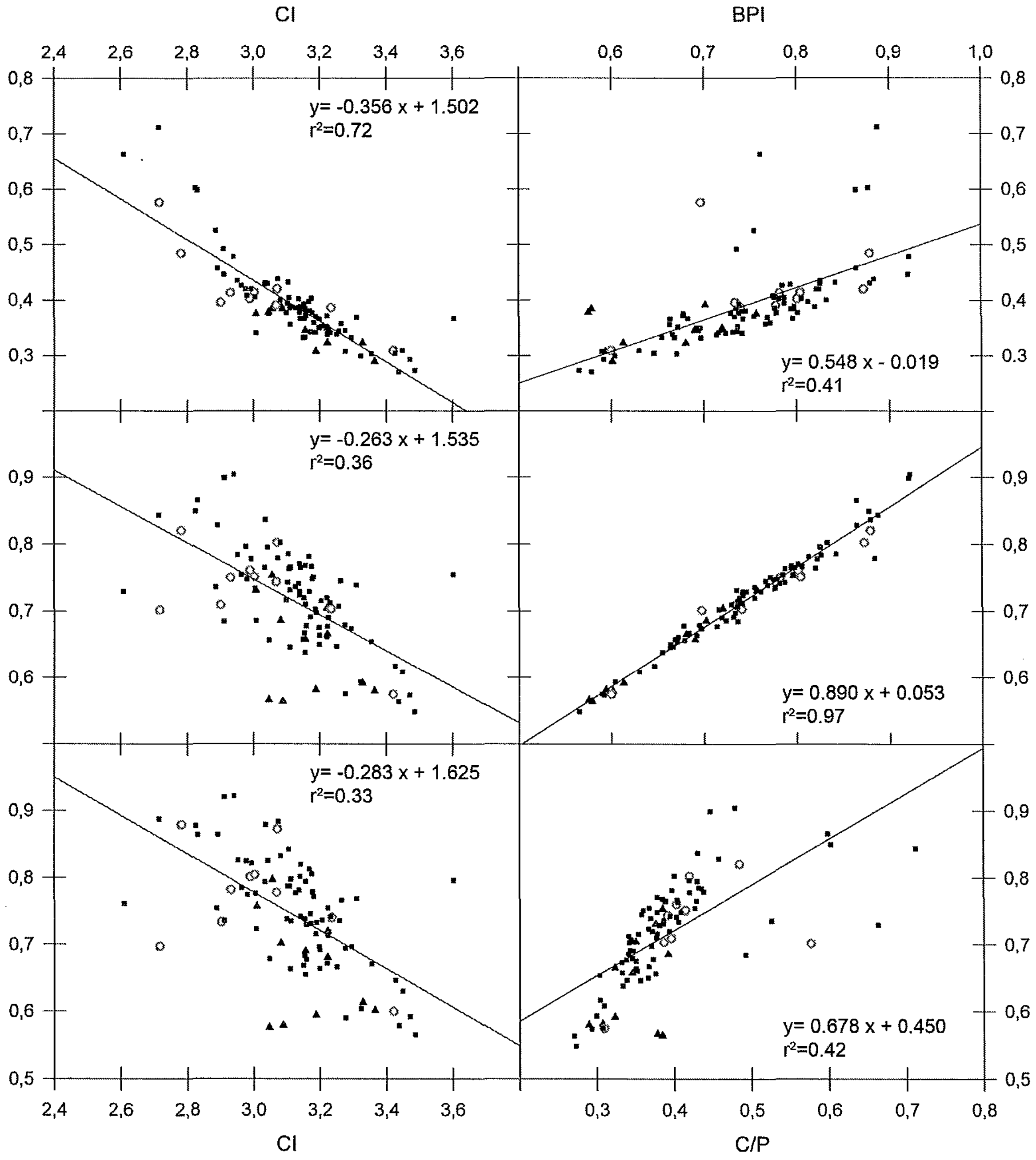

Figure 5-3. Comparison of FTIR indexes by pairs (CI, C/P, BPI and TCC) measured on 95 deer bone samples from Lamanai (▲), Motul de San José (O) and Piedras Negras (■). Linear regression equations and related correlation coefficients (r^2) are shown for each case

5.3.5) FTIR indexes and $\delta^{18}O_C$-$\delta^{18}O_P$ test

Lastly, the FTIR indexes obtained on the remaining 95 deer bone samples can be split in two sub-groups, corresponding to (1) the samples falling between the two lines in figures 5-1 and 5-2, *i.e.* included in the range [$\delta^{18}O_C(\pm1.3) = 1.02(\pm0.04) \times \delta^{18}O_P + 8.3(\pm0.7)$]; thus considered as non-diagenetically altered (n=86) and (2) the samples falling outside the range, that are considered as diagenetically altered (n=9). The summary of FTIR indexes obtained on those two sub-groups is presented in table 5-6.

Table 5-6. Summary of FTIR indexes measured on the samples accepted and rejected by the comparative test $\delta^{18}O_C$ *vs* $\delta^{18}O_P$.

Index	Accepted (n=86)				Rejected (n=9)			
	average	min	max	σ	average	min	max	σ
CI	3.1	2.6	3.6	0.2	3.2	2.9	3.4	0.2
C/P	0.39	0.27	0.71	0.08	0.37	0.27	0.47	0.06
BPI	0.74	0.57	0.92	0.08	0.72	0.57	0.92	0.11
TCC	0.71	0.54	0.89	0.07	0.70	0.56	0.90	0.11

Given the difference in the number of samples analyzed, the comparison between the two sub-groups is questionable. However, it appears that no difference is perceptible between the two categories, for any of the FTIR indexes. Lastly, one must notice that the two samples containing secondary recrystallized calcite were not rejected by $\delta^{18}O_C$-$\delta^{18}O_P$ comparison.

5.3.6) FTIR indexes, $\delta^{13}C_{Bone}$ and $\delta^{18}O_C$

With the high correlation coefficients linking CI and carbonate content, the relations between $\delta^{18}O_C$, $\delta^{13}C_{Bone}$ and those indexes have been tested, to check a possible effect of carbonate content on the isotopic composition of deer bone measured on carbonate groups ($\delta^{18}O_C$ and $\delta^{13}C_{Bone}$). On figure 5-4, it can be seen that neither $\delta^{18}O_C$ nor $\delta^{13}C_{Bone}$ values are linearly correlated with CI, C/P or BPI (and as a consequence, TCC): all the correlation coefficients are close to 0.

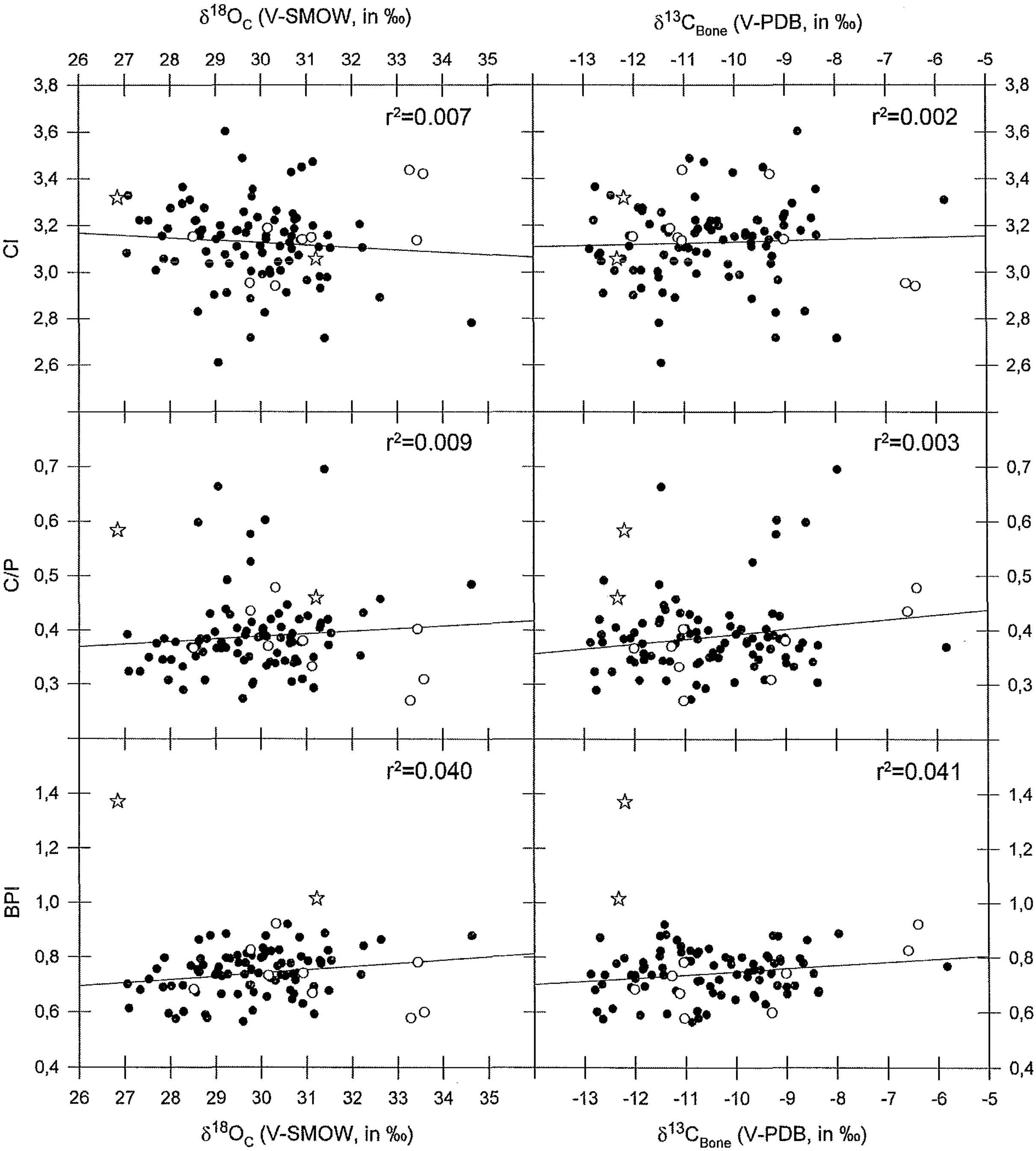

Figure 5-4. Comparison between $\delta^{18}O_C$, $\delta^{13}C_{Bone}$ and CI, C/P and BPI measured on 97 deer bone samples. ●: samples accepted by the $\delta^{18}O_C$ -$\delta^{18}O_P$ test (n=86); ○: samples rejected by the $\delta^{18}O_C$ -$\delta^{18}O_P$ test (n=9); ☆: samples with calcite (n=2; not included in the regression equations). Linear correlation lines and corresponding correlation coefficients are shown.

As previously mentioned (see part 5.3.5 above), there is no perceptible trend between samples accepted by the $\delta^{18}O_C$-$\delta^{18}O_P$ test and those rejected: the rejected bone samples (indicated by o in figure 5-4) do not cluster in specific portions of the graphs. Interestingly, only the BPI (or TCC) index is capable to differentiate the two samples containing calcite (indicated by ☆ in figure 5-4), with BPI's > 1.

5.4) $\delta^{18}O_P$, $\delta^{18}O_C$ and $\delta^{13}C_{Bone}$ variations through time

Given the uncertainties related to the use of FTIR indexes to detect diagenetically altered bones (confirmed by the data shown in table 5-6), it has been decided to not use them for diagenesis screening (except for the two samples containing calcite). Those aspects will be discussed in Chapter 6. The linear correlation between $\delta^{18}O_P$ and $\delta^{18}O_C$ as an indicator of diagenesis appears to be a more reliable index of diagenesis, given the underlying biologic effect, and the empirical verification by several studies (refer to Chapter 4, part 4.3.2).

In the end, among the 98 bones selected and analyzed for this study, 5 were rejected by $\delta^{18}O_C$-$\delta^{18}O_P$ comparison (1 from MSJ and 4 from PN) and 2 were rejected because of the presence of calcite (1 from LAM and 1 from MSJ). A total of 92 bones (table 5-7, next page) were then finally selected for reconstructing past climate variations at Lamanai, Motul de San José and Piedras Negras. The results are shown in figure 5-5, presenting the variations of $\delta^{18}O_P$, $\delta^{18}O_C$ and $\delta^{13}C_{Bone}$ through time at Lamanai, Motul de San José and Piedras Negras.

The Pre-Classic period at Lamanai (before AD 300) and the Abal/Pom cultural phase at Piedras Negras (BC 300-AD 350) were each only represented by a single bone, and haven't been included in figure 5-5.

Table 5-7. Summary of all the $\delta^{18}O_P$, $\delta^{18}O_C$ and $\delta^{13}C_{Bone}$ measured on samples of archaeological deer bones from Lamanai, Motul de San José and Piedras Negras. All isotopic values are given in ‰ and relatively to V-SMOW ($\delta^{18}O_P$, $\delta^{18}O_C$) or V-PDB ($\delta^{13}C_{Bone}$). The table indicates the number of bones analyzed per cultural phase and the number of bones finally accepted after diagenesis screening. All standard deviations σ are given in ‰.

Cultural phase	years (AD)	bones sampled	bones Accepted(*)	average $\delta^{18}O_P$	min $\delta^{18}O_P$	max $\delta^{18}O_P$	st. dev. (1 σ)	average $\delta^{13}C_{Bone}$	min $\delta^{13}C_{Bone}$	max $\delta^{13}C_{Bone}$	st. dev. (1 σ)	average $\delta^{18}O_C$	min $\delta^{18}O_C$	max $\delta^{18}O_C$	st. dev. (1 σ)
Lamanai															
Pre-Classic	<300	2	1	20.5	20.5	20.5	N/A	-10.3	-10.3	-10.3	N/A	27.5	27.5	27.5	N/A
Post-Classic	1000-1519	6	6	20.9	18.9	21.6	1.0	-12.0	-12.8	-10.8	0.8	27.9	27.0	28.8	0.6
Colonial	1519-1821	7	7	20.8	20.1	22.0	0.7	-11.9	-12.8	-11.1	0.6	27.6	27.1	28.0	0.4
	All phases	*15*	*14*	*20.8*	*18.9*	*22.0*	*0.8*	*-11.9*	*-12.8*	*-10.3*	*0.8*	*27.7*	*27.0*	*28.8*	*0.5*
Motul de San José															
Late Classic	600-800	6	5	21.9	20.2	23.4	1.2	-10.4	-11.8	-9.2	1.3	30.2	29.6	31.8	0.9
Terminal Classic	800-1000	5	4	21.1	20.2	22.4	1.0	-10.5	-12.7	-9.0	1.6	30.1	29.5	30.8	0.5
Early Post-Classic	1000-1250	1	1	22.0	22.0	22.0	N/A	-11.5	-11.5	-11.5	N/A	29.8	29.8	29.8	N/A
	All phases	*12*	*10*	*21.6*	*20.2*	*23.4*	*1.1*	*-10.5*	*-12.7*	*-9.0*	*1.3*	*30.1*	*29.5*	*31.8*	*0.7*
Piedras Negras															
Abal/Pom	300BC – 350	2	1	19.6	19.6	19.6	N/A	-11.3	-11.3	-11.3	N/A	30.5	30.5	30.5	N/A
Naba	350-560	4	4	20.4	20.1	21.1	0.5	-9.6	-9.9	-9.2	0.3	29.8	28.6	30.6	0.9
Balche	560-620	12	11	20.9	19.8	22.7	1.0	-10.0	-12.5	-8.6	1.3	30.3	28.6	31.5	0.9
Yaxche	620-750	26	26	20.6	18.7	22.2	0.9	-10.2	-12.0	-8.0	0.9	30.0	28.0	31.6	1.0
Chacalhaaz	750-850	24	22	20.3	18.5	22.4	1.1	-10.7	-12.8	-8.5	1.2	29.8	28.3	32.2	0.9
Kumche	850-900	3	3	20.7	19.3	22.9	1.9	-8.4	-10.9	-5.8	2.5	29.9	28.4	31.5	1.5
	All phases	*71*	*67*	*20.5*	*18.5*	*22.9*	*1.0*	*-10.2*	*-12.8*	*-5.8*	*1.2*	*30.0*	*28.0*	*32.2*	*0.9*

N/A : *not applicable ;* (*) *bones for which no calcite was detected by FTIR spectroscopy and the comparison* $\delta^{18}O_C$-$\delta^{18}O_P$ *falls in the range* $\delta^{18}O_C(\pm 1.3) = 1.02(\pm 0.04) \times \delta^{18}O_P + 8.3(\pm 0.7)$

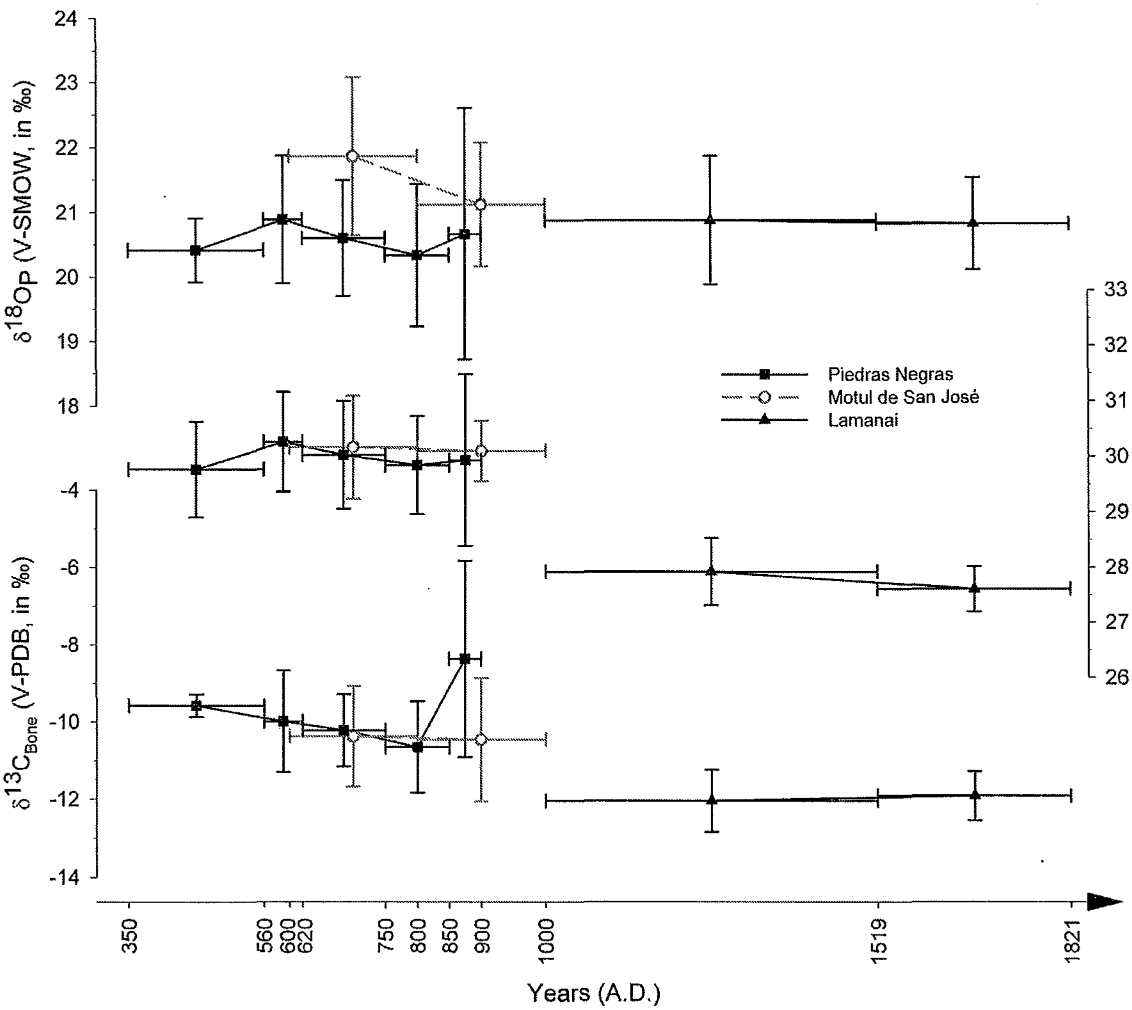

Figure 5-5. Summary plot of $\delta^{18}O_P$ (top), $\delta^{18}O_C$ (middle) and $\delta^{13}C_{Bone}$ (bottom) values measured on archaeological deer bones from Lamanai, Motul de San José and Piedras Negras. Time line indicates the boundaries of the cultural phases (horizontal whisker caps) distinguished at each site. Each phase is represented by its average value (▲: Lamanai, ○: Motul de San José, ■: Piedras Negras), plus or minus standard deviation (vertical whisker caps). Isotopic values are given relatively to V-SMOW ($\delta^{18}O_P$ and $\delta^{18}O_C$) or V-PDB ($\delta^{13}C_{Bone}$).

At a glance, the examination of table 5-7 and figure 5-5 shows that:

(1) At Lamanai, almost no difference in average $\delta^{18}O_P$ or $\delta^{13}C_{Bone}$ is observed from the Post-Classic period (AD 1000-1519) to the colonial period (1519-1821; - 0.1 ‰ and + 0.1 ‰, respectively), but the average $\delta^{18}O_C$ decreases slightly (-0.3 ‰).

(2) At Motul de San José, from the Late Classic period (AD 600-800) to the Terminal Classic period (AD 800-1000), the average $\delta^{18}O_P$ decreases by 0.8 *‰* while the average $\delta^{18}O_C$ remains stable (-0.1*‰*), as does the average $\delta^{13}C_{Bone}$ (-0.1 *‰*).

(3) At Piedras Negras, the three sets of isotopic measurements show the same pattern. From Balche (AD 560-620) to Chacalhaaz (AD 750-850) cultural phase, average values of $\delta^{18}O_P$, $\delta^{18}O_C$ and $\delta^{13}C_{Bone}$ decrease continuously (from 20.9 to 20.3 *‰*, from 30.3 to 29.8 *‰* and from -10.0 to -10.7 *‰*, respectively), and then increase from Chacalhaaz to Kumche (AD 850-900) cultural phase (by 0.4 *‰*, 0.1 *‰* and 2.3 *‰*). Average $\delta^{18}O_P$ and $\delta^{18}O_C$ values from Naba (AD 350-560) phase are lower than those of Balche (by 0.8 and 0.7 *‰*, respectively), but in the case of $\delta^{13}C_{Bone}$, the average is higher (by 0.4 *‰*).

(4) As for the comparison between the sites, in the case of $\delta^{18}O_P$, the values from Motul de San José are on average higher than those of Piedras Negras and Lamanai (21.6 *‰* against 20.5 *‰* and 20.8 *‰*, respectively). For $\delta^{18}O_C$ and $\delta^{13}C_{Bone}$, the average values from Lamanai are lower than those from Motul de San José and Piedras Negras (27.7 *‰* against 30.1 and 30.0 *‰*, and -11.9 *‰* against -10.5 and -10.2 *‰*, respectively).

The reliability of this dataset, its implications as well as its interpretation for the reconstruction of past climate reconstruction are discussed in the next chapter.

References

Bryant J.D., P. Koch, P.N. Froelich, W.J. Showers, B.J. Genna (1996) – Oxygen isotope partitioning between phosphate and carbonate in mammalian apatite. *Geochimica et Cosmochimica Acta* 60, 5145-5148.

Munro L.E., F.J. Longstaffe, C.D. White (2007) - Burning and boiling of modern deer bone: Effects on crystallinity and oxygen isotope composition of bioapatite phosphate. *Palaeogeography, Palaeoclimatology, Palaeoecology* 249, 90-102.

Pucéat E., B. Reynard, C. Lécuyer (2004) - Can crystallinity be used to determine the degree of chemical alteration of biogenic apatites? *Chemical Geology* 205, 83– 97.

Sillen A. & J. Parkington (1996) – Diagenesis of bones from Eland's bay cave. *Journal of Archaeological Science* 23, (4): 535-542.

Sponheimer, M. and J. A. Lee-Thorp (1999) - Alteration of enamel carbonate environments during fossilization. *Journal of Archaeological Science* 26, (2): 143-150.

Surovell T.A. & M.C. Stiner (2001) - Standardizing infra-red measures of bone mineral crystallinity: An experimental approach. *Journal of Archaeological Science* 28, (6): 633-642.

Trueman C.N., K. Privat, J. Field (2008) - Why do crystallinity values fail to predict the extent of diagenetic alteration of bone mineral? *Palaeogeography Palaeoclimatology Palaeoecology* 266, (3-4): 160-167.

Wright L.E. & H.P. Schwarcz (1996) - Infrared and isotopic evidence for diagenesis of bone apatite at Dos Pilas, Guatemala: palaeodietary implications. *Journal of Archaeological Science* 23, 933-944.

Chapter 6 - Discussion

In this last chapter, the objective is to discuss exhaustively the significance of the results presented in Chapter 5. The first part covers the methodological aspects of the study, including the effects of samples preparation and the degree of precision and reliability of the measured isotopic ratios. The second part evaluates the techniques used to detect possible diagenetic alteration of the samples, emphasizing on the reliability of FTIR spectroscopy to do so. The third part addresses the time resolution and representativeness of the studied material. The final part finally discusses the interpretation of the results in terms of climatic and environmental changes at Lamanai, Motul de San José and Piedras Negras.

6.1) Methodology and precision

Pretreatment protocols designated to eliminate contaminants, the isolation of the groups of interest (carbonate and phosphate) in a measurable form (CO_2 and Ag_3PO_4), and the way those chemical species are analyzed by the mass spectrometers (Optima and TC/EA) are steps likely to introduce artefacts that can modify the original isotopic composition of the bone samples. Hence, one must ensure that the measured isotopic ratios ($\delta^{18}O_P$, $\delta^{18}O_C$ and $\delta^{13}C_{Bone}$) are really corresponding to those of the bioapatite lattice, and that those ratios are measured with an acceptable degree of precision.

6.1.1) Sample preparation

6.1.1.1) Organic matter removal

The standard procedure for bone preparation first eliminates the organic component of the powdered samples by oxidization by weak sodium hypochlorite (NaOCl; Chapter 4, part 4.2.2)

The organic matter is thought to affect bone isotopic values by creating interferences due to: (1) the possible formation of radicals of the masses 44-46 in the ionization chamber of the mass spectrometer (Wierzbowski, 2007), (2) the liberation of organic-derived CO_2 during reaction with orthosphosphoric acid (Epstein *et al.*, 1953) or (3) interference during the precipitation of silver phosphate crystals (Wiedemann-Bidlack *et al.*, 2008).

One must keep in mind that the reaction of bone powder with NaOCl does not remove the total amount of organic matter in the bone, as approximately 15% of it is found in apatite crystal aggregates, where it is not vulnerable to attack by NaOCl (Weiner & Price, 1986; DeNiro & Weiner, 1988). The proportion of bone mass lost by NaOCl dissolution thus reflects the survival of that organic fraction, which is susceptible to loss during diagenesis (Garvie-Lok *et al.*, 2004).

Koch *et al.* (1997) demonstrated that the reaction between NaOCl and bone does alter slightly the isotope values of bone. However, interpreting this offset is difficult, because the comparison is made with a referent fresh bone (presumed unaltered), in which the organic content is higher than in archaeological bones, so the shift induced by NaOCl treatment may reflect the removal of actual contaminants. The same authors also examined the potential for isotopic exchange during NaOCl treatment by performing a set of experiments in which an isotopically enriched NaOCl solution was prepared by dilution in ^{18}O-enriched water, to obtain a solution in which $\delta^{18}O_{NaOCl}$ ~20‰: they shown that the reaction between ^{18}O-enriched NaOCl did not significantly affect $\delta^{18}O_C$ values.

Some authors also noticed that organic matter contamination can be inferred by the colour and shape of precipitated Ag_3PO_4 crystals (Chapter 4, part 4.2.1): a golden yellow coloration of large euhedral (regular) crystals is characteristic for a precipitate free of organic residue, while darker green to black fine-grained crystals is a good indication of remaining traces of organic material in the Ag_3PO_4 crystal lattice (e.g. O'Neil *et al.*, 1994; Wiedemann-Bidlack *et al.*, 2008). In the case of incomplete organic matter removal, a similar brown coloration of the phosphoric acid (H_3PO_4), characteristic of organic matter oxidization, would have been expected in the 9 mm pyrex tubes used for $\delta^{18}O_C$ and $\delta^{13}C_{Bone}$ preparation, at the end of the reaction (Chapter 4, part 4.2.2). None of these two features were observed during samples processing, leading to the conclusion that the organic matter seemed to have properly been removed from bone samples prior to isotopic measurements.

In the end, there is still no agreement on the effects of organic matter removal protocol on isotopic values of bone carbonate and phosphate, neither is there as for the optimal reaction time. As recommended by Koch *et al.* (1997), care must be taken to obtain consistent isotopic offsets as a result of pre-treatment of samples. In the present work, each sample has been scrupulously subjected to the same organic matter removal protocol, using the same NaOCl stock solution and the same reaction times. It is thus considered that a possible offset of the isotopic values would have been the same for each sample, allowing a meaningful comparison between the obtained values.

6.1.1.2) Secondary carbonate removal

After the organic matter removal step, bone powder for $\delta^{18}O_C$ and $\delta^{13}C_{Bone}$ measurements is reacted for 12 hours with a 1 M solution of weak acetic acid (CH_3-COOH) buffered with calcium acetate ($CaCO_2CH_3$; pH ~4.5; Chapter 4, part 4.2.2). The rationale behind this step is to "etch" the surface of bioapatite crystallites, in order to remove any labile secondary carbonate that could have been adsorbed or replaced diagenetically at the surface of bioapatite crystallites (see part 6.2 below; Krueger, 1991; Wright & Schwarcz, 1996; Koch *et al.*, 1997; Garvie-Lok *et al.*, 2004).

The technique of acetic acid treatment has been originally developed by Lee-Thorp (1989), using 1 M acetic acid (pH ~2.4). Several studies have been using this method (e.g. Wang & Cerling, 1994; Saliège *et al.*, 1995; Wright & Schwarcz, 1996), but some researchers were concerned about the effects of overly harsh acid treatment which may induce sample re-crystallization and excessive sample loss, so the use of less concentrated acetic acid (0.1 M, pH ~2.9; e.g. Balasse *et al.*, 2002) or a buffered acetic acid (e.g. Bocherens *et al.*, 1994; Wright & Schwarcz, 1998; this study) has sometimes been preferred.

Excessive sample loss by dissolution during acetic acid treatment can be linked to particle size (*i.e.* to the way the sample is ground): Lee-Thorp *et al.* (1997) showed that hand-drilled powder is more vulnerable to dissolution than powder obtained by cryo-crushing.

Lee-Thorp & van der Merwe (1991) documented the beginning of brushite ($CaHPO_4 \cdot 2 H_2O$) formation in modern bone samples treated with 1 M acetic acid after 48 hours of reaction time, and thus suggested to reduce treatment time to less than 2 days, or to use a less astringent solution.

However, there is still no consensus about a "universal" method to be adopted to remove diagenetic carbonate from bone samples. Several studies conclude differently: some authors claim they obtain good results using 1 M acetic acid (e.g. Krueger, 1991; Lee-Thorp & van der Merwe, 1991), other studies noticed a strong alteration of isotopic values with 1 M acetic acid but not when 0.1 M acetic acid is used (e.g. Balasse *et al.*, 2002; Stuart-Williams *et al.*, 1996), yet other suggest alteration even after a reaction of 1 hour in 0.1 M acetic acid (e.g. Nielsen-Marsh & Hedges, 1997).

A possible explanation for such a disagreement may be the diagenetic history of the material (Nielsen-Marsh & Hedges, 2000a): when bone samples underwent recrystallization processes forming highly soluble material at crystallite surface (e.g. calcite), treatment with acetic acid is believed to totally remove the diagenetic material, while samples contaminated with carbonate-poor recystallized apatite (fluorapatite), less soluble than the remaining intact bone mineral, poor results are obtained, regardless of the concentration of acetic acid solution (Nielsen-Marsh & Hedges, 2000b).

In the end, it has been chosen to follow Koch et al.'s recommendations (1997), and to use a 1 M acetic acid solution, acetate buffered. Although the same authors showed that acetic acid - acetate buffered treatment causes $\delta^{18}O_C$ values to increase and $\delta^{13}C_{Bone}$ values to decrease, presumably resulting from a partial recrystallization of bioapatite into brushite (causing isotopic exchange affecting $\delta^{18}O_C$) and/or a differential dissolution of A-type and B-type substituted carbonate (modifying average $\delta^{13}C_{Bone}$), they state that this treatment induces the smallest isotopic offsets in bone, compared to non-buffered acetic acid solutions at 0.1 and 1 M.

Again, it is considered here that the possible offset of isotopic values would have been the same for each sample, given that sample preparation protocol has been rigorously followed, and all bones were prepared using the same stock solution of acetic acid – acetate buffer. Comparison between sample's $\delta^{13}C_{Bone}$ and $\delta^{18}O_C$ values can thus be considered as meaningful.

6.1.1.3) CO_2 isolation for $\delta^{18}O_C$ and $\delta^{13}C_{Bone}$ measurements

Once organic matter and possible diagenetic carbonate have been removed, both carbon and oxygen atoms are extracted from the carbonate groups of the bioapatite lattice by reaction with an excess of 100% anhydrous phosphoric acid, provoking the liberation of CO_2, according to the following reaction:

$$CaCO_3 + H_3PO_4 \rightarrow CaHPO_4 + CO_2 + H_2O$$

This reaction is a quantitative reaction, so the conversion of carbonate groups (CO_3^{2-}) into CO_2 occurs in a one-way fashion, without possible backward equilibrium. As noticed by Wright & Schwarcz (1996), the oxygen isotopic fractionation during this reaction (due to the conversion of only two of the oxygen atoms of CO_3^{2-} into CO_2 at a time, *i.e.* not a 100 % yield) has not been experimentally determined but is presumed to result in the enrichment of liberated CO_2 by about 10.2 ‰, similar to the one determined for the reaction between geological calcite ($CaCO_3$) with phosphoric acid (H_3PO_4) at 25°C (Friedman & O'Neil, 1977). Hence, the measured $\delta^{18}O_C$ values should be understood as being ~10 ‰ lower than the "true" bone values. The reaction is left during three days in a water bath at 25°C to allow isotopic equilibration of liberated CO_2. No fractionation of $\delta^{13}C_{Bone}$ occurs during this reaction.

6.1.1.4) Ag_3PO_4 precipitation for $\delta^{18}O_P$ measurements

Isolation of bioapatite phosphate as silver phosphate crystals quickly became the protocol of choice because of its relative easiness and because Ag_3PO_4 crystals are not hygroscopic, thus avoiding possible atmospheric water vapour contamination during samples preparation (Crowson *et al.*, 1991).

Once organic matter has been removed (see above), bone powder samples are dissolved in nitric acid to ionize phosphate groups of the bioapatite lattice (*i.e.* to get PO_4^{3-} ions in solution; Chapter 4, part 4.2.1). The pH of the solution is then raised to allow a quicker precipitation of silver phosphate crystals (Dettman *et al.*, 2001). Calcium ions are precipitated as Calcium Fluoride (CaF_2) provoked by the addition of ammonium fluoride (NH_4F) and removed by centrifugation along with insoluble collagen (Stephan, 2000; Bassett *et al.*, 2007). The "quick" precipitation of silver phosphate crystals starts when the pH of the solution drops while ammonia, evolved from the reaction between silver amine ($AgNO_3$, 0.2M; NH_4NO_3, 0.35 M; NH_4OH, 0.74M) and ionized phosphate groups, evaporates. The reaction ends at pH of about 7, and the reaction is quantitative (O'Neil *et al.*, 1994). PO_4^{3-} ions are recombined with Ag^{3+} in the solution, so no fractionation occurs during the silver phosphate precipitation step (Stephan, 2000). In the TC/EA graphite crucible, Ag_3PO_4 is converted quantitatively to CO and analysed by continuous flow mass spectrometry. It has been recently showed that this method provides 100% yields for oxygen, and can thus be trusted to accurately measure the "true" $\delta^{18}O_P$ (Vennemann *et al.*, 2002).

6.1.2) Precision

6.1.2.1) TC/EA and $\delta^{18}O_P$ measurements

Table 5-1 (Chapter 5) shows that the standard deviations measured on benzoic acid and USGS-35 are quite different. Replicated measurements (n=42) of benzoic acid $\delta^{18}O$ give a good reproducibility (σ ~0.2‰), comparable to other studies using a similar method (e.g. O'Neil *et al.*, 1994; Dettman *et al.*, 2001; Vennemann *et al.*, 2002; Wiedemann-Bidlack *et al.*, 2008). However, the reproducibility obtained on 10 replicated measurements of USGS-35 standard KNO_3 $\delta^{18}O$ is poor (σ ~1.0‰). A recent study (Brand *et al.*, 2009) highlighted an effect of possible nitric oxide (NO) formation during high temperature combustion in the TC/EA column: NO is ionized in $^{14}N^{16}O^+$, interfering with the measurement of $^{12}C^{18}O^+$, detected by the same Faraday cup in the mass spectrometer (same atomic weight). This less well-defined value at the higher end of the calibration line may affect the "true" $\delta^{18}O_P$ values, but this is not a major issue in the present work for two reasons: (1) the $\delta^{18}O_P$ values obtained on deer bone samples (ranging from 18.5 to 23.4 ‰; table 5-7, Chapter 5) cluster slightly under the expected $\delta^{18}O$ value of benzoic acid ($\delta^{18}O_{IAEA\text{-}601}$ = 23.3 ‰), and are far away from the expected $\delta^{18}O$ values of USGS-35 ($\delta^{18}O_{USGS\text{-}35}$

= 57.5 ‰), so the uncertainties of measured $\delta^{18}O_{USGS\text{-}35}$ have a limited impact on the "true" $\delta^{18}O_P$ values, and (2) the objective of this study is to compare $\delta^{18}O_P$ values between them, so the "true" $\delta^{18}O_P$ values are not really important, but their relative differences are.

As for deer bone $\delta^{18}O_P$ reproducibility, the most striking feature of the dataset is the very high variability of standard deviations from triplicated measurements: the σ-values on each bone sample range from very low values (close to $\sigma = 0$ ‰, thus indicating almost a perfect reproducibility) to very high values (e.g. $\sigma = \sim 1.4$ ‰, indicating a high degree of scatter during replicated measurements; table 5-1, Chapter 5). The reasons underlying such variability remain unclear. No correlations between σ and CI or C/P FTIR indexes have been found (data not shown). A plausible explanation would be the contamination of Ag_3PO_4 crystals by organic matter is some samples that could result either in (1) a direct contribution of oxygen organic matter to the measured $\delta^{18}O_P$ or (2) an alteration of the TC/EA reaction, betrayed by misshapen CO peaks during data acquisition (Wiedemann-Bidlack *et al.*, 2008). Although organic matter contamination of the samples is the most probable explanation, no such misshapen peak were observed, and precipitated Ag_3PO_4 crystals all exhibited a bright yellow colour (see part 6.1.1.1 above). It is thus concluded that organic matter removal by bleaching (NaOCl) or by centrifugation after the addition of ammonium fluoride (NH_4F) might have been incomplete.

6.1.2.2) Optima, $\delta^{18}O_C$ and $\delta^{13}C_{Bone}$ measurements

Table 5-1 (Chapter 5) shows that the standard deviations measured standard calcite (NBS-18 and NBS-19, both n=17) are of ~0.2 ‰ ($\delta^{13}C$) and ~0.3-0.4 ‰ ($\delta^{18}O$). Surprisingly, the reproducibility we obtained was relatively poor, compared to other studies using the same offline reaction method to convert standard calcite into CO_2 (*i.e.* standard deviations closer to 0.1 ‰ for both isotopes; e.g. Wright & Schwarcz, 1996; Koch *et al.*, 1997; Garvie-Lok *et al.*, 2004). Yet the offline method is tedious, but is recognized to be the one giving the best reproducible results, compared to more recent and quicker online methods (e.g. Gasbench, Multiprep; Metcalfe *et al.*, 2009).

Although the mass spectrometer itself can be incriminated to explain this poorly reproducible measurements on standards, the reproducibility of $\delta^{13}C_{Bone}$ measurements is more than acceptable (average σ = 0.1 ‰ at PN, n=93), but some measurements were highly scattered (e.g. maximum σ of 1.0 ‰ at MSJ; table 5-1, Chapter 5). The average reproducibility of $\delta^{18}O_C$ measurements is comparable to the standard reproducibility (e.g. average σ at PN is 0.4 ‰, n=93), but as in the case of $\delta^{13}C_{Bone}$ measurements, some samples exhibit a high degree of scattering (e.g. maximum σ of 1.2 ‰ at PN; table 5-1, Chapter 5). No correlations between FTIR indexes and $\delta^{13}C_{Bone}$ or $\delta^{18}O_C$ reproducibility have been found (data not shown).

A recent study (Metcalfe *et al.*, 2009) conducted on human bones from Maya sites of the Pacific coast of Guatemala (dated from AD 250 to 400) obtained several results that support the validity of the method we used for $\delta^{13}C_{Bone}$ and $\delta^{18}O_C$ measurements (corresponding to their *Conventional 25* method). Interestingly, the same authors highlighted "abnormal" low and highly variable $\delta^{18}O_C$ values on some of their bones that are believed to be related to the production of an unidentified contaminant gas during CO_2 liberation, interfering with the measurement of oxygen isotopic ratios. Precursors of the contaminant gas in the bioapatite crystals were not identified by FTIR spectroscopy, and the presence of the contaminant gas has not been observed on bones from other contexts (Sudan). Similar abnormally low and inexplicable $\delta^{18}O_C$ values were also observed by Wright & Schwarcz (1996) on human bone from another Maya site of the Petén region, in Guatemala (dated from AD 600 to 950).

The high scatter degree of $\delta^{18}O_C$ and $\delta^{13}C_{Bone}$ we obtained on some bones is thus possibly related to either (1) the incomplete removal of organic matter, as in the case of $\delta^{18}O_P$ measurements (see above) or (2) the diagenetic context of Maya sites (e.g. seasonal variations in temperature and soil moisture), but the latter underlying mechanisms are not understood and should be further investigated.

In the end, only $\delta^{18}O_P$ values are considered to be reliable to reconstruct past climate variations in the Maya region (see part 6.2 below), so the poor reproducibility of $\delta^{18}O_C$ measurements, although affecting the accuracy of the $\delta^{18}O_P$-$\delta^{18}O_C$ diagenesis test, should have no significant impact on the reliability of the following climate reconstruction. The good reproducibility of $\delta^{13}C_{Bone}$ measurements allow us to consider them as precisely measured.

6.2) Diagenesis assessment

"Many authors involved in palaeoclimatological isotope research are inclined firmly to believe in the reliability of the results obtained, without even discussing the possibility that diagenetic processes may have modified the original isotopic values of the studied samples. This may be a venial sin in the case of relatively young fossils but becomes a sin of arrogance in the case of old and very old fossils" (Longinelli, 1996).

6.2.1) Limits of FTIR spectroscopy

6.2.1.1) Crystallinity Indexes

Measuring the Crystallinity Index from the perspective of using it as the expression of the degree of geochemical integrity of archaeological bone has its rough patches. They are mainly of three kinds: the standardization of (1) the method and (2) protocol, as well as (3) the sensitivity of the technique.

(1) Standardization of crystallinity measure by FTIR spectroscopy is not well established. In the first place, and surprisingly, there is still no consensus on the methodology for the choice of the baseline drawn as the starting point for peaks heights calculation. Weiner & Bar-Yosef (1990) suggest that the degree of splitting can be estimated by drawing a baseline from 750-495 cm^{-1}. However, several papers (e.g. Pucéat *et al.*, 2004; Munro *et al.*, 2007) follow Shemesh (1990), who draws the baseline between 750 and 450 cm^{-1}, (although Shemesh cites the article of Weiner & Bar-Yosef, 1990!). Surovell & Stiner (2001) drew a baseline "approximately" from 780 to 495 cm^{-1}. Another category of baseline "strategy" is to consider a global baseline including all, or most of the wavenumbers range of the spectrum: Sponheimer & Lee-Thorp (1999), as well as Botha *et al.* (2004) used a baseline correction from 4000 to 500 cm^{-1}, while Wright & Schwarcz (1996) used one ranging from 1800 to 400 cm^{-1}. In the present study, all peak heights for CI

calculation were measured from a baseline ranging from the next lowest points on either side of the double peak detected in the v_4-PO_4 domain (as represented in figure 4-6b, Chapter 4). From a rigorous point of view, the discrepancy between those methods prevents a strict comparison between the CI values. Nevertheless, since the CI is given only with one decimal place, the slight difference in the baseline choice does not affect the obtained values significantly, and comparison between different papers can be considered as meaningful.

(2) Secondly, care must be taken regarding the way bone sample is ground. Pelletizing bone powder for FTIR spectroscopy implies crushing the sample. Ideally, the diameter of crushed bone apatite particles should be less than the wavelength of the incident beam (between 2.5 μm at 4000 cm^{-1} and 25 μm at 400 cm^{-1}, but larger than the length of the biggest bone apatite crystals, that are 0.1 μm; refer to Chapter 2, part 2-4). If the diameter of crushed bone particles is larger than the wavelength of the incident beam, beam diffraction can occur, leading to a distorted CI value. On the other hand, if the sample is too finely ground, there is a chance of damaging bone apatite crystallites, and thus a risk of provoking the amorphization of bone apatite crystallites, and so, leading to the decrease of sample CI value. Surovell & Stiner (2001) have made an attempt to study the effects of grinding on measured CI values. Using the same archaeological bone, they asked three persons to grind the sample (using a pestle and mortar) and measured the CI values on several pellets. The obtained values ranged from 2.78 to 3.78, with reproducibility (σ) no more than ± 0.15 for each set (Chapter 5, table 5-4). This difference of ~35 % of CI value from a same bone clearly brings out the problem of bone preparation standardization. To circumvent that issue, in this paper, mechanical grinding has been chosen because we believe it is the best way to ensure a replicable grinding between bone samples (control on strength and duration). However, given that different types of bones have been used (e.g. tibia, ribs, finger bones), their hardness was somehow different. In the case of ribs, for example, the cortical part was relatively thin and easy to break, but for some long bones, some small fragments (a few millimetres in size) remained in the powder after cryo-crushing. The selection of powder particles with diameters ranging from 2.5 to 25 μm was impossible here, because the amount of bone powder that had to be sifted on cellulose filters (11-45 μm) to get the required 2 mg was excessive (~30 g) and is thus not applicable to archaeological samples, in which sampling size had to be kept at a minimum (Chapter 5, part 5.3.2).

(3) To test the sensitivity of FTIR spectrometry against CI, it is possible to mimic the effects of diagenesis, by artificially increasing the crystallinity of a bone sample by heating it (providing heat makes the crystallites more stable, by getting quicker and closer to the thermodynamic equilibrium). Several studies were designed to expose a bone sample to gradually increased temperature, then measure the CI, and compare it to the obtained $\delta^{18}O_P$ and $\delta^{18}O_C$ values measured afterwards. In their studies, Munro *et al.* (2007, 2008) heated fresh deer bone, from 25° to 900°, in 25° intervals (either boiled before heating or not, refer to Chapter 4, part 4.3.1), to simulate cooking and refuse disposal practices. Unfortunately, only small changes in measured CI were observed when the sample is heated below 675° (CI values stay in the same range, close to 3.0), despite much larger changes in $\delta^{18}O_P$ and $\delta^{18}O_C$ values above 225-250° (Chapter 4, figure 4-1). When heated above 675°, the CI values measured are progressively reaching the values usually seen on fossil samples (CI close to 4.0). These studies highlight the lack of sensitivity of FTIR spectroscopy to detect chemical remodelling in bone after exposure to heat.

Even though the results from 95 analyses of deer bone CI by FTIR spectroscopy have shown an acceptable level of reproducibility, they show that: (1) we were unable to detect a significant difference of CI between the average CI value (CI ~3.1; Chapter 5, table 5-4) and the CI measured on a charred deer bone sample, presumably strongly altered (CI ~3.1; Chapter 5, table 5-3); (2) no significant CI difference has been found between samples accepted by the $\delta^{18}O_C$-$\delta^{18}O_P$ test and those rejected (3.1 *versus* 3.2; Chapter 5, table 5-6); (3) unlike what was expected, the grinding intensity and duration do not seem to affect the CI value: no amorphization effect is detected when samples are heavily ground (Chapter 5, table 5-3); and (4) we cannot consider CI sensitive enough to accurately describe intra-bone variability (Chapter 5, figure 5-1 and table 5-5).

In the end, a high CI (>4.0) can be considered as a proof of *post-mortem* recrystallization with confidence, but a relatively low CI is not a token of geochemical integrity. For all the reasons described above, it has been decided to avoid the use of CI to screen out deer bones for past climate reconstruction, as recently suggested by several authors (e.g. Pucéat *et al.*, 2004; Trueman *et al.*, 2008).

6.2.1.2) Carbonate content

(1) BPI and TCC

The high linear correlation coefficient (r^2=0.97, n=95) between the BPI index (the amount of B-type carbonate to phosphate) used by Sponheimer & Lee-Thorp (1999) or Botha *et al.* (2004) and the TCC index (the total carbonate content) used by Pucéat *et al.* (2004) proves that those two indexes, even if calculated differently (refer to Chapter 4, part 4.3.3.3), are in fact describing the same variable. However, the first is considered to reflect the relative amount of B-type substituted carbonate while the second is considered to reflect the total relative amount of carbonate (*i.e.* A-type and B-type).

Four conclusions are thus possible: (1) in bone bioapatite, B-type substitution is largely predominant (Wright & Schwarcz, 1996), or there is even no A-type substituted carbonate in analyzed deer bones (Elliott, 2002; Wopenka & Pasteris, 2005), and in that case, several papers dealing with A-type carbonate in bones should be reconsidered; (2) the deer bones analyzed in this study are all diagenetically altered, and underwent chemical remodelling resulting in a total removal of A-type substituted carbonate: according to Sponheimer & Lee-Thorp (1999) this endogenous carbonate reorganization associated to A-type carbonate loss characterizes fossilization; (3) the TCC index is describing the B-type substituted carbonate only, and thus cannot be called "Total Carbonate Content"; (4) the BPI index is in fact describing the "real" total carbonate content.

Considering the uncertainties related to the presence of A-type carbonate in bone bioapatite, it is difficult to affirm if Pucéat *et al.* have named their index wrongly, or if Sponheimer & Lee-Thorp and Botha *et al.* did. It is also believed that the probability for all deer bones to be diagenetically altered is small, given that almost all of them passed the $\delta^{18}O_P$-$\delta^{18}O_C$ test (Chapter 5, figure 5-2).

In the end, it is interesting to notice that, due to the strong linear correlation between TCC and BPI, the peak heights of the two doublets from the ν_3-CO_3 and the ν_4-PO_4 domains are inter-dependent and are linked by the following relation (Chapter 5, figure 5-3):

$$\frac{Peak_{1420}}{Peak_{605}} = 0.890\frac{Peak_{1460} + Peak_{1420}}{Peak_{605} + Peak_{563}} + 0.053 \qquad (r^2=0.97, n=95)$$

where $Peak_{1420}$ and $Peak_{1460}$ are the peak heights of the ν_3-CO_3 domain doublet and $Peak_{563}$ and $Peak_{605}$ are those of the ν_4-PO_4 domain doublet (Chapter 4, figure 4-5).

(2) C/P *versus* TCC and BPI

To measure the carbonate content, Wright & Schwarcz (1996) used the C/P, the ratio between the absorbance of the CO_3 peak at ~1420 cm^{-1} in the ν_3-CO_3 domain and the main peak of the ν_3-PO_4 domain, at ~1035 cm^{-1} (Chapter 4, figure 4-5). The linear correlation between C/P and TCC/BPI is high ($r^2=0.82$ or 0.83), when 9 outliers showing "abnormally" high C/P values are removed from the dataset (Chapter 5, part 5.3.4). This tends to show that C/P and TCC/BPI are also describing the same variable.

The same authors have shown that C/P values are positively correlated with weight % CO_2 ($r^2=0.64$; n=31, least square fitted line passes near to the origin) checked by manometric measurement of the CO_2 volume liberated during the reaction between bone powder and orthophoshoric acid. Given the latter verification, it is considered that the C/P can be trusted to accurately describe the true total carbonate content.

(3) Carbonate content *versus* CI

As mentioned in Chapter 2 (part 2.4.4), it has been shown on artificially-produced apatites that type-B substitutions in the crystal lattice affect several aspects of the physical properties of hydroxylapatite, such as crystal size (decrease in the *a*-axial length and increase in the *c*-axial length, or in other words, a stretching of the crystals), and consequently the degree of crystallinity of the crystal lattice (*i.e.* a decrease of CI; Wopenka & Pasteris, 2005). The dependence of CI's on carbonate content has been noticed by several studies (e.g. DeMul *et al.*, 1986; Penel *et al.*, 1998; Baig *et al.*, 1999)

Our results agree with these studies: the correlation coefficient between CI and C/P is high (r^2=0.73, n=95), and high CI's are correlated with low C/P indexes (Chapter 5, figure 5-3). This strong linear correlation between CI and C/P index indicates that carbonate content in bones accounts for a substantial amount of the variability in crystallinity. This latter observation reinforce the idea that CI is not a reliable index for recrystallization, as an increase of crystallinity could be compensated by an increase of carbonate content, without changing the resulting CI.

When the 9 samples exhibiting relatively high C/P values are excluded from the dataset, the correlation coefficient between CI and C/P does not change significantly (from 0.73 to 0.68) and those between CI and BPI or TCC are slightly increased (from 0.33 to 0.47 and from 0.36 to 0.49, respectively; Chapter 5, part 5.3.4). This reinforce the idea that C/P index is more reliable than TCC/BPI indexes to measure carbonate content

(4) Carbonate content *versus* $\delta^{18}O_C$ and $\delta^{13}C_{Bone}$

Due to the strong linear relation between CI and carbonate content indexes, a relation between those indexes and $\delta^{18}O_C$ or $\delta^{13}C_{Bone}$ was suspected, and has been checked. The results show that there is absolutely no linear correlation between the measured isotopic compositions on deer bone carbonate groups and carbonate content (Chapter 5, figure 5-4). To minimize the variability between the samples, same tests for linear correlation were conducted on sub-groups, by site and by period, but the linear correlation coefficients were still close to 0.

The samples rejected by the $\delta^{18}O_P$-$\delta^{18}O_C$ test were also unidentifiable, but interestingly, the two samples containing calcite were clearly detected by high BPI (or TCC) indexes only, but none gave anomalous C/P or CI indexes. Given that (1) the C/P is calculated by dividing the height of the ~1420 cm^{-1} peak (one of the doublet of the ν_3-CO_3 domain) by the height of the ~1035 cm^{-1} peak (the peak of the ν_3-PO_4 domain) and (2) the BPI is calculated by calculated by dividing the height of the same ~1420 cm^{-1} peak by the height of the ~605 cm^{-1} peak (one of the doublet of the ν_4-PO_4 domain; refer to Chapter 4, part 4.3.3.2), and (3) the three heights are measured from a same baseline, it can be deduced that the presence of secondary re-crystallized calcite in the bioapatite crystal lattice affects only one of the two vibrational modes of phosphate group (PO_4), *i.e.* the mode being responsible for the doublet of the ν_4-PO_4 vibrational domain. Further interpretation as for the position of diagenetic calcite inside the crystal lattice relatively to phosphate groups (or its possible adsorption at the surface of bioapatite crystallite) would be dubious, given that only two samples contained calcite, in addition to the uncertainties described earlier.

6.2.1.3) Hydroxyl-apatite ?

Since the development of FTIR spectroscopy it has been shown that bone apatite spectra match those of synthetic and geologic hydroxylapatite, with the major exception that unlike mature enamel apatite, neither the O-H stretch band nor any other band accounting for vibrational mode of hydroxyl group (OH) has been observed, at any stage of bone maturation (Rey *et al.*, 1995; Elliott, 2002; Wopenka & Pasteris, 2005). The underlying crystallographic reasons explaining the absence of hydroxyl groups are still unclear and some reasons have been proposed, such as A-type carbonate substitutions, charge imbalance induced by B-type carbonate substitutions forcing vacancies, global degree of atomic distortion linked to the size of bone apatite crystallites, nucleation mechanisms...; see Wopenka & Pasteris, 2005). The current consensus considers bone apatite as a form of carbonated apatite with varying carbonate content, rather than hydroxylapatite (Elliott, 2002; Fratzl *et al.*, 2004; Wopenka & Pasteris, 2005).

This last example is mentioned to highlight that the use of FTIR spectroscopy is weakened by the problems related to spectra interpretation: despite more than 40 years of bone apatite spectroscopic studies, neither the exact nature of the carbonate substitution nor the state of hydroxylation of the lattice are well understood.

However FTIR spectroscopy provides insight into the molecular environment of asymmetrically vibrating bonds like no other technique, and it has exercised a major influence on the assessment of bone and tooth geochemical integrity. Given its ease and quickness, it could not have been ignored in this study. In the end, FTIR spectroscopy has made possible the detection of two bone samples containing calcite (Chapter 5, part 5.3.2).

6.2.2) $\delta^{18}O$ reliability

6.2.2.1) Comparison between $\delta^{18}O_P$ and $\delta^{18}O_C$

The co-genesis of carbonate and phosphate groups in the bioapatite lattice from the same oxygen source (*i.e.* the body water; Chapter 4, part 4.3.2), in addition to the constant body temperature at which osteogenesis mechanisms occur among mammals (Chapter 2, part 2.3), results in a linear relation between $\delta^{18}O_P$ and $\delta^{18}O_C$ (Chapter 4, figure 4-3): the comparison of coexisting $\delta^{18}O_P$-$\delta^{18}O_C$ values from the same sample can thus serve as a test of diagenesis (e.g. Kolodny & Luz, 1991; Iacumin *et al.*, 1996; Bryant *et al.*, 1996; Fricke *et al.*, 1998; Shahack-Gross *et al.*, 1999)

From a theoretical point of view, *post-mortem* isotope alteration may re-set the $\delta^{18}O_P$ and $\delta^{18}O_C$ in a new equilibrium condition, and their position would be shifted away from the equilibrium line (Iacumin *et al.*, 1996). The P-O chemical bond being stronger than the C-O bond, there is a large difference in activation energy between the two co-existing compounds (e.g. Longinelli, 1984; Longinelli, 1996; Kohn *et al.*, 1999), so chemical remodelling is thus likely to affect preferentially the oxygen of carbonate groups in bioapatite. However plotting $\delta^{18}O_P$-$\delta^{18}O_C$ pairs against the equilibrium line detects isotopic disequilibria, but cannot unambiguously determine which component has been altered. For example, recent laboratory experiments have demonstrated that, unlike inorganic exchanges processes, microbially-mediated diagenesis of bones may affect the $\delta^{18}O_P$ more than $\delta^{18}O_C$ (e.g. Ayliffe *et al.*, 1994; Blake *et al.*, 1997; Berna *et al.*, 2004; Zazzo *et al.*, 2004)

To quantify the minimum range of deviation from the expected $\delta^{18}O_P$-$\delta^{18}O_C$ equilibrium line that a bone sample has to exhibit to be considered as diagenetically altered, it has been decided to use the equation from Bryant *et al.* (1996; Chapter 4, equation [4.3]). This equation represents the 95% confidence interval of the linear regression through all of their data points, and is considered to take into account the uncertainties related to isotopic measurements (see part

6.1 above). This range has the assumed advantage of sparing the use of objective turn of phrases such as "clustering", "close" or "away" from the equilibrium line.

On figure 5-2 (Chapter 5), it can be seen that almost all the points are falling inside this range (93 out of 97), but $\delta^{18}O_P$-$\delta^{18}O_C$ pairs are concentrated in different portions of the graph when the three sites are considered separately. For example, bones from Lamanai are showing relatively low $\delta^{18}O_C$ values (average $\delta^{18}O_C$ ~27.7 ‰) compared to Motul de San José and Piedras Negras (where average $\delta^{18}O_C$ values are ~30.1 and ~30.0 ‰, respectively), while when $\delta^{18}O_P$ values are considered, MSJ differs from the two other sites (average $\delta^{18}O_P$ at MSJ is ~21.6 ‰, ~20.8 ‰ at LAM and ~20.5 ‰ at PN; refer also to figure 5-5 and table 5-7, Chapter 5). This discrepancy between the $\delta^{18}O_P$ and the $\delta^{18}O_C$ patterns indicate that the initial isotopic composition of the samples has been altered.

6.2.2.2) Extent of diagenetic alteration

As previously mentioned, oxygen atoms carried by carbonate groups are expected to be more sensitive to diagenetic remodelling, but inorganic diagenetic processes may have been strong enough to modify both $\delta^{18}O_P$ and $\delta^{18}O_C$ values. In the latter case, both isotopic ratios measured on bones from a same site would tend to converge towards specific $\delta^{18}O_P$ and $\delta^{18}O_C$ values, resulting from the *post-mortem* recrystallization of bioapatite crystallites, in equilibrium with soil solution. Although most of the samples passed the $\delta^{18}O_P$-$\delta^{18}O_C$ test, the $\delta^{18}O_P$ and $\delta^{18}O_C$ patterns at MSJ and PN are dissimilar, so there is unequivocal evidence of diagenetic replacement of oxygen atoms in the bioapatite lattice (figure 5-5; Chapter 5). However, three arguments are pleading in favour of weak diagenetic effects that would have affected the $\delta^{18}O_C$ values, without modifying the $\delta^{18}O_P$ values:

(1) *$\delta^{18}O_C$ homogenization.* At MSJ, the variability of the $\delta^{18}O_P$ values between the different periods distinguished is clearly visible: the average $\delta^{18}O_P$ values decrease from 23.4 ‰ (Late Classic) to 22.4 ‰ (Terminal Classic), with standard deviations (σ) of 1.2 and 1.0 ‰, respectively (table 5-6, Chapter 5). However, when the $\delta^{18}O_C$ dataset is considered, the distinction between the Late and Terminal Classic becomes almost insignificant (the difference is 0.1 ‰) and standard deviations are lower (σ ~0.9 and σ ~0.5 ‰, respectively), so the $\delta^{18}O_C$

measured on bones from MSJ tend to converge towards a single hypothetic equilibrium value. This indicates that carbonate-bound oxygen atoms at MSJ have probably been replaced, but phosphate-bound atoms were not, or at least, not enough to homogenise the $\delta^{18}O_P$ values like $\delta^{18}O_C$ values were. This trend is also perceptible at LAM, where standard deviations of the $\delta^{18}O_C$ dataset (average σ ~0.5 ‰) are slightly lower than those of the $\delta^{18}O_P$ dataset (average σ ~0.8 ‰). No such trend is observed on samples from PN, where average standard deviations are similar ($\delta^{18}O_P$: σ ~1.0 ‰; $\delta^{18}O_C$: σ ~0.9 ‰). The underlying reasons to explain such a difference between the extent of diagenesis at PN and at MSJ or LAM are difficult to assess without a precise knowledge of soil characteristics at each site. Depth of the water table, concentration of relevant solutes, pH, redox potential, seasonal variations in soil hydrology, or the presence of particular microbial flora are possible factors influencing the strength of diagenesis mechanisms (see Hedges, 2002). Nevertheless, it is interesting to notice that both MSJ and LAM are located close to stagnant watesr: LAM lies on the shore of the New River Lagoon and MSJ is a few kilometres north from Lake Petén-Itza, so the depth of water table at those two sites is probably higher than at PN, the latter being located on the banks of Usumacinta river.

(2) *Intra-bone variability.* The intra-bone variability of the 24 doubly-sampled bones (figure 5-1, Chapter 5) also argues in favour of a weak diagenetic alteration during burial time. Unfortunately, only 2 bones from MSJ were sampled twice (none from LAM), so it would be mistaken to draw conclusions on MSJ diagenetic context. However, on bones from PN, it can be seen that duplicated samples from a same bone exhibit different $\delta^{18}O_C$ and $\delta^{18}O_P$ values, without trend as for the variability of $\delta^{18}O_P$ relatively to $\delta^{18}O_C$ (Chapter 5, part 5.2). It can be concluded that either carbonate- and phosphate-bound oxygen atoms have been diagenetically replaced in a random fashion or none of them underwent diagenesis. The first solution appears to be unrealistic, given the low probability for diagenetic processes to affect phosphate groups and carbonate groups indistinctly. However, it cannot be admitted that oxygen isotopic composition of the 22 bones from PN is fully pristine, given that for six of them, one of the duplicate (or both in one case) is falling outside the accepted range of the $\delta^{18}O_P$-$\delta^{18}O_C$ test. This would mean that diagenetic processes may affect the bone in patches, some zones being more sensitive to them. The locations for duplicated samplings have been chosen to select bone parts with same

histological properties (*i.e.* only the thickest parts of dense cortical bone), so it is unclear here what may have caused this differential alteration.

(3) *The difference in $\delta^{18}O_P$ between MSJ and PN.* The last argument suggesting that $\delta^{18}O_P$ values are reliable is indirect. As stated in Chapter 1 (part 1.2.1), both MSJ and PN are fed with rain derived from seawater evaporated on the Caribbean basin. PN being located downwind relatively to MSJ (figure 1-2, Chapter 1), the combination of the *amount effect* and the *continental effect* causes the average $\delta^{18}O_{Rain}$ at PN to be ~1.5 ‰ lower than the $\delta^{18}O_{Rain}$ at MSJ (Chapter 3, part 3.1.3). If it is assumed that climatic and environmental variables are similar between MSJ and PN (relative humidity and temperature fluctuations, vegetation), this 1.5 ‰ difference is expected to be visible on deer bones from PN and MSJ. When the Late Classic $\delta^{18}O_P$ dataset from MSJ (AD 600-800, n=5) is compared to the $\delta^{18}O_P$ dataset from PN merging Balche, Yaxche and Chacalhaaz phases (*i.e.* AD 560-850, n=62), the average $\delta^{18}O_P$ at MSJ is ~1.4 ‰ higher than the one at PN (21.9 against 20.5 ‰), with similar standard deviations of the two datasets (1.2 against 1.0 ‰), as expected. Nevertheless, the strength of the argument is weakened by the difference in the numbers of bone samples included in each dataset (5 against 62).

In the end, because bone sampling has been conducted on dense cortical bone with no apparent histological evidence of biological attack (Bell *et al.*, 2001; Turner-Walker & Syversen, 2002), and for the reasons detailed above, phosphate-bound oxygen in archaeological deer bones is presumed pristine, so $\delta^{18}O_P$ values are considered to be reliable and can thus be trusted to reconstruct past climate variations in the Maya region.

6.2.3) $\delta^{13}C_{Bone}$ reliability

Due to the weaker nature of Ca-CO_3 than the Ca-PO_4 bonds (Elliott, 2002; Botha *et al.*, 2004), $\delta^{13}C_{Bone}$ signal is archaeological bone may be altered by exchange of CO_3 with soil solution after burial (Wright & Schwarcz, 1996).

Because of the high surface area and high cation exchange capacity (high sorption coefficient) of bone apatite crystallites, a significant proportion of carbonate groups are adsorbed onto crystal surface and may react with non-biogenic carbonate after interment (Wright & Schwarcz, 1996; Glimcher, 2006; Trueman *et al.*, 2008). This adsorbed carbonate is considered as labile and may have contributed to the wide range of C/P values at LAM, MSJ and PN (from 0.3 to 0.7; figure 5-3, Chapter 5), but this fraction of exogenous carbonate is considered to be removed by acetic acid treatment prior to isotopic analyses (see part 6.1 above).

The internal check for non-alteration of $\delta^{13}C_{Bone}$ is usually done by a comparison with $\delta^{13}C$ values measured on the organic component of bone (on collagen proteins) since $\delta^{13}C$ from both organic and mineral phase of archaeological bones of varying ages yielded consistent isotopic difference between the two phases, similarly to the $\delta^{18}O_P$-$\delta^{18}O_C$ test (e.g. Sullivan & Krueger, 1981). Unfortunately, due to the low amount of available powder, such analyses were not conducted.

Since this comparison was not feasible, a reverse reasoning can be considered: what if carbon atoms of the bioapatite lattice have been replaced by dissolved carbonated species of the soil solution? The carbon isotopic composition of soil has been measured at Piedras Negras by Fernández *et al.* (2005): although varying with depth, it is never reaching values higher than ~20 ‰ and is about -27 ‰ at the surface, resulting from oxidation of organic debris from the dominantly C3 plants in the region. Comparable ranges of soil $\delta^{13}C$ values has been observed at MSJ (Webb *et al.*, 2007), and are thus expected at LAM. Hence, in case of carbon exchange, a shift of $\delta^{13}C_{Bone}$ values towards highly ^{13}C-depleted values would have been expected, much lower than the minimum possible $\delta^{13}C_{Bone}$ expected (*i.e.* -13 ‰) from browser herbivores, feeding exclusively on C3 plants (figure 3-6, Chapter 3). No such low values have been measured on any of the deer bones analyzed in the present study (table 5-7, Chapter 5). Actually, $\delta^{13}C_{Bone}$ values obtained from LAM, MSJ and PN lie in the expected range for C3-dominant consumers.

In the end, although there is no unequivocal evidence for lack of alteration of $\delta^{13}C_{Bone}$, we are inclined to consider carbon isotopic values as biogenic, and thus reliable to reconstruct past environmental and climatic variations at LAM, MSJ and PN.

6.3) Temporal and spatial resolution

6.3.1) Bone dating

All deer bones were dated by stratigraphic analysis of the presence or absence of ceramic wares. Mayan ceramics have well-defined features (e.g. surface finish, colour, decorative motifs, vessel morphology) that changed rapidly with the history of each site, resulting from the interactions with surrounding cities, related to the degree of influence/importance of the site considered (*i.e.* power centre like PN or vassal city like MSJ). The context and content of the deposits from which the ceramics shreds were excavated, and the comparison with absolute dates derived from inscription or radiocarbon dates obtained from associated remains make possible the distinction of cultural phases with a high degree of precision (e.g. Foias, 2003; Muñoz, 2004).

Although stratigraphic analysis has its related uncertainties (a review of the concepts is available in Harris, 1979), we assume that the dating of deer remains provided by the archaeologists and ceramicists in charge of excavations at LAM, MSJ and PN is accurate (Chapter 2, part 2.1), although the precision of the dates is difficult to estimate due to the mixture of techniques used to obtain them

6.3.2) Bone temporal resolution

As mentioned in Chapter 2, little is known about deer bone turnover rate, but some studies have shown that this process is correlated with metabolic rate (Darr & Hewitt, 2008) and seems to be strongly bone-dependant (Hillman *et al.*, 1973; Baxter *et al.*, 1999). As a consequence of constant bone remodelling, the sampling of dense bone material consists of a complex mesh of osteons, whose age spans the life of the deer. It is thus considered that each analyzed bone sample is likely to represent a "time-average" of bio-mineralization processes that took place within the span of deer's life.

The life expectancy of white-tailed deer in the wild today is about 10 years (DelGiudice *et al.*, 2007), but during the Maya era, when hunting impact was high, it is likely that life span was lower. All $\delta^{18}O_P$, $\delta^{18}O_C$ and $\delta^{13}C_{Bone}$ values were obtained on archaeological deer bones identified as coming from separate adult individuals (part 2.1, Chapter 2), so it is assumed that each deer bone is averaging roughly 2.5 years of environmental records, corresponding to what is believed to be appropriate to "resource management", that is a sufficient amount of time for deer to reach their sexual maturity (~1.5 years) and to breed (Smith, 1991; Brunjes *et al.*, 2006).

Hence, the "dilution effect" of bone turnover possibly makes brief and/or moderate droughts (corresponding to droughts categories D0, D1 or D2; see table 1-1, Chapter 1) hardly detectable by isotopic analyses, but severe or extreme droughts (D4 and D5 droughts) could be detected with confidence.

6.3.3) Bone spatial resolution

A review of white-tailed deer ethology has been compiled in Smith (1991). showing that: (1) white-tailed deer occupy a well-defined home range year after year; (2) movements and home range are influenced by age, sex, density, social interactions, latitude, season, and habitat characteristics; (3) annual home range averages 59- 520 ha and areas of seasonal use rarely exceed 1.6 km in radius; (4) circular home ranges with uniform use characterize more homogeneous habitats and (5) size of home range is inversely correlated with the density of vegetative cover and habitat diversity.

From these observations, it is inferred that in the Maya Lowlands, deer home range is a few km^2. We also assume that deer consumed by the Maya has been hunted locally (*i.e.* in a radius corresponding to a single day walk), so it is considered that the isotopic signal held in deer bones excavated at a given site represents very local conditions (see Chapter 3, part 3.3).

6.3.4) Dataset representativeness

The major issue when reconstructing past environmental and climatic changes using archaeological material stems from its scarcity. The variable duration of archaeological ceramic phases may contribute to uncertainty in the climatic and environmental representativeness of the data, as well as in comparing records between sites. Each bone offers a "window" of 2.5 years of past conditions, and cultural phases distinguished by ceramic dating range from 50 years (e.g. Kumche at PN) to 650 years in length (e.g. Abal/Pom at PN). One must therefore be sure to analyze a sufficient number of individual deer bones, to provide a broad range of specimens from across the phase. In a single cultural phase, the amount of time covered by bones can range from 2.5 years (if all deer were born in the same year) to a theoretical maximum as high as 2.5 times the number of analyzed bones (if all deer were born at different times, with at least 2.5 years between each birth). Table 6-1 presents those minimum and maximum theoretical "time coverage" per cultural phase.

Table 6-1. Theroretical minimum and maximum relative amounts of time covered by each bone set by cultural phase at Lamanai, Motul de San José and Piedras Negras.

Cultural phase	Years (AD)	Bones used[a]	Minimum[b] coverage (in %)	Maximum[c] coverage (in %)	Average coverage (in %)
Lamanai					
Pre-Classic	<300	1	N/A	N/A	N/A
Post-Classic	1000-1519	6	0.5	2.9	1.7
Colonial	1519-1821	7	0.8	5.8	3.3
Motul de San José					
Late Classic	600-800	5	1.25	6.2	3.7
Terminal Classic	800-1000	4	1.25	5	3.1
Early Post-Classic	1000-1250	1	1	1	1
Piedras Negras					
Abal/Pom	300BC – 350	1	0.4	0.4	0.4
Naba	350-560	4	1.2	4.8	3
Balche	560-620	11	4.2	46	25.1
Yaxche	620-750	26	1.9	50	26
Chacalhaaz	750-850	22	2.5	55	28.6
Kumche	850-900	3	5	15	10

(a): number of bones considered as non-diagenetically altered (see table 5-7, Chapter 5);
(b): corresponding to 2.5 years per cultural phase; (c): corresponding to 2.5 years multiplied by the number of bone used per cultural phase; N/A: not applicable

One must keep in mind that the representativeness of each cultural phase can range from the minimum to the maximum value, with equal probability for each coverage percentage in between to be correct. Instead of considering the maximum time coverage per cultural phase, we estimate the arithmetical average to be closer to the "real" representativeness.

In this perspective, it is considered that there is a sufficient number of samples from Balche, Yaxche and Chacalhaaz phases at PN to be representative of past conditions, with ~25% of the duration of these three phases thought to have been recorded in the three bone sets. The next best representative bone set is from Kumche (PN), in which only 10 % of the time is likely to have been recorded. The density of sampling is significantly less for the other periods (Abal/Pom and Naba at PN, and all phases at LAM and MSJ), that are poorly represented (less than 4% of time is covered), thus making generalizations on past conditions during those periods highly speculative.

6.4) Reconstruction of past conditions

Now that it has been established that the $\delta^{18}O_P$ and $\delta^{13}C_{Bone}$ datasets obtained on deer bones are thought to be reliable (see part 6.1 and 6.2 above), and that the density of bone samples is considered as representative of climatic and environmental conditions for the Balche, Yaxche, Chacalhaaz phases at Piedras Negras (and in a lesser extent the Kumche phase; see part 6.3 above), our attention can be focused on those phases. Figure 6-1 below is similar to figure 5-5 (Chapter 5), but focuses on the phases cited above, and maxima and minima $\delta^{18}O_P$ and $\delta^{13}C_{Bone}$ for each phase are indicated.

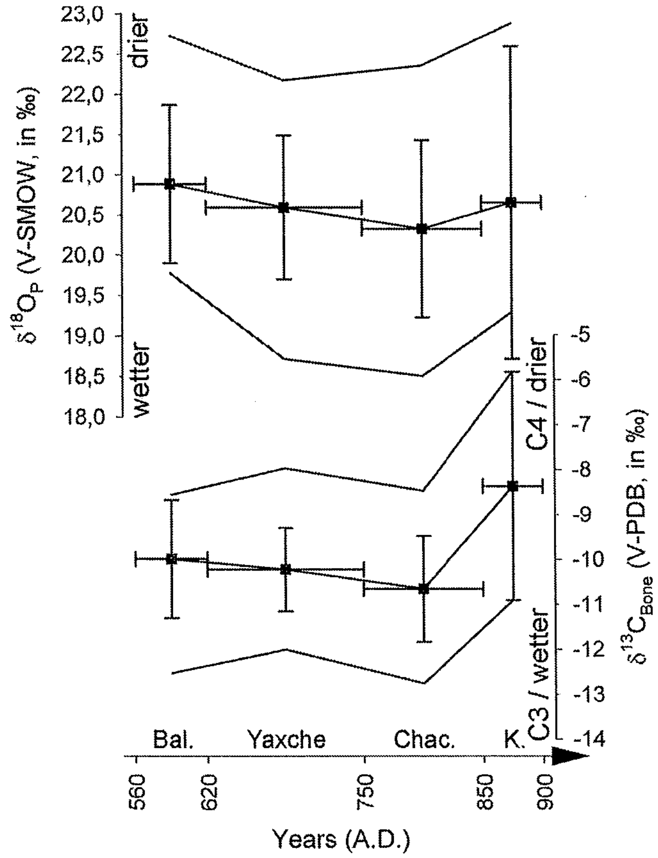

Figure 6. Summary plot of $\delta^{18}O_P$ (top) and $\delta^{13}C_{Bone}$ (bottom) values measured on archaeological deer bones from Piedras Negras. Time line indicates the boundaries of Balche (n=11), Yaxche (n=26), Chacalhaaz (n=22) and Kumche (n=3) cultural phases (horizontal whisker caps). Each phase is represented by its average value (■) plus or minus standard deviation (vertical whisker caps), maximum (upper line) and minimum (bottom line) values. Isotopic values are given relatively to V-SMOW ($\delta^{18}O_P$) or V-PDB ($\delta^{13}C_{Bone}$).

As indicated on figure 6-1, according to the model described in Chapter 3, high $\delta^{18}O_P$ values are considered as reflecting drier conditions, and high $\delta^{13}C_{Bone}$ values are indicating either drier conditions or a higher proportion of C4 plants in a deer's diet

6.4.1) Interpreting $\delta^{18}O_P$ variations

In Chapter 3, the two equations proposed by Luz *et al.* (1990; eq. [3.3] and [3.4], part 3.4.1) were used to calculate a rough estimate of expected $\delta^{18}O_P$ on deer bones that would have been living at Flores (~MSJ) during 2.5 years of relatively dry "modern" conditions (e.g. 1994 or 1998) or relatively "modern" wet conditions (e.g. 1997 or 2006). Because of the *amount effect*, the yearly average $\delta^{18}O_{Rain}$ at PN is ~1.5 ‰ lower than at MSJ (Chapter 3, part 3.1). If it is assumed that yearly average relative humidity at MSJ and PN are similar, the expected $\delta^{18}O_P$ values at PN can be estimated (see table 6-2 below).

Table 6-2. Estimated $\delta^{18}O_{Rain}$ and deer bone bioapatite $\delta^{18}O_P$ at PN in relation with average climatic conditions that have occurred at Flores during relatively dry (1994 and 1998) and wet years (1997 and 2006).

Year	Total precipitation (in mm)[a]	Yearly average relative humidity[a]	Estimated yearly average $\delta^{18}O_{Rain}$ at PN[b]	Expected deer bone $\delta^{18}O_P$ range at PN (in ‰)[c]	Expected deer bone $\delta^{18}O_P$ at PN (in ‰)[d]
1994	1,160	76	-3.4	19.2 – 25.2	19.4
1998	1,456	74	-3.1	19.8 – 25.3	20.0
1997	1,600	83	-3.8	17.6 – 24.3	18.0
2006[e]	2,395	77	-5.1	17.5 – 26.5	18.1

a: available in Flores climatic dataset (INSIVUMEH, 2009); b: see table 3-1, Chapter 3; c: using eq.[3.3], Chapter 3; d: using eq. [3.4], Chapter 3; e: November 2006 values missing and were not taken into account

6.4.1.1) Expected *versus* obtained values

The absolute values presented in table 6-2 are to be taken with caution for two reasons:

(1) *Inference from Veracruz.* The yearly averaged $\delta^{18}O_{Rain}$ at PN has been estimated based on the relation found between precipitation amount and measured $\delta^{18}O_{Rain}$ at Veracruz (equation [3.2], Chapter 3). Even if dominant winds are blowing from east to west (see Chapter 1), Veracruz is located on the coast of the Gulf of Mexico (figure 3-2b, Chapter 3), so the $\delta^{18}O_{Rain}$ measured

there may be influenced by water evaporated from the Gulf of Mexico, unlike PN. This influence of "foreign" water vapour could affect the accuracy of the estimated $\delta^{18}O_{Rain}$ values at PN.

(2) *Luz et al.'s equations.* Luz *et al.* (1990) are suggesting two equations linking deer bone $\delta^{18}O_P$ to $\delta^{18}O_{Rain}$ and relative humidity (corresponding to equations [3.3] and [3.4] in Chapter 3). Their $\delta^{18}O_P$ dataset has been obtained on deer bones coming from temperate regions (across the United States and southern Canada), where $\delta^{18}O_{Rain}$ is principally controlled by variations in air temperature. In those regions (especially the northernmost ones), they considered that bone growth tends to be more rapid in the spring and summer, when food supplies are more abundant. This is why two equations are given: the first one is based on yearly averages of $\delta^{18}O_{Rain}$ and relative humidity while the second is based on growing season averages only (*i.e.* when precipitation occurs above 0°C). However, both equations have a similar linear correlation coefficient, so it is not possible to judge which equation gives the more reliable estimates of $\delta^{18}O_P$. It can be added that equation [3.3] is less precise than equation [3.4] in estimating deer bone $\delta^{18}O_P$, because it gives a range of values, unlike equation [3.4].

Not surprisingly, the $\delta^{18}O_P$ values measured on deer bones from PN fall in the broad range expected from equation [3.3]. Nevertheless, they are systematically underestimated by equation [3.4]: minima range from ~18.5 to ~20 ‰ (corresponding to modern wet years in table 6-2; figure 6-1) and maxima range from ~22 to ~23 ‰ (*i.e.* 2 to 3 ‰ higher than what is expected for modern dry years). So even though equation [3.4] gives precise estimates, it is not accurate.

The underestimation of $\delta^{18}O_P$ values by equation [3.4] could be related to two specificities of the climatic context of the Maya region (relatively to northern America), that may contribute to explain why $\delta^{18}O_P$ values at PN are higher than predicted:

(1) *Constant high temperatures.* When daily maximum temperatures pass 30°C, as usual in the Maya region (especially at the end of the dry season; figure 1-6, Chapter 1), water intake becomes critical to thermo-regulation, because deer suffers major water loss by perspiration and/or panting (Lautier *et al.*, 1988). The $\delta^{18}O$ of water lost through skin is depleted relatively to body water (reported fractionations range from -8 to -21 ‰ among mammals, depending on the

species; see Kohn, 1996). So high perspiration rates would shift body water $\delta^{18}O$ and ultimately deer bone $\delta^{18}O_P$ towards higher values. As a side-effect of high rates of perspiration during the dry season, deer's water requirements may be not fully satisfied by leaf water only, forcing deer to search for available surface meteoric water (river, lake). Hence it is plausible that inputs of highly ^{18}O-enriched (*i.e.* evaporated) drinking water during dry periods would also contribute to shift bone $\delta^{18}O_P$ towards higher values.

(2) *High precipitation amounts.* As suggested by Luz *et al.* (1990), mechanisms of leaf water enrichment during evapo-transpiration (Chapter 3, part 3.2.1) modulate deer bone $\delta^{18}O_P$. In the Maya Lowlands, the high temperatures and high precipitation amounts permitted the development of a luxurious ever-growing rainforest. With these optimal conditions, high metabolic rates and productivity (organic matter synthesis) of tropical plants can be linked to nearly constant evapo-transpiration mechanisms, so the extent of leaf water enrichment can be considered to be maximal. In temperate regions, plants developed physiologies adapted to relative water scarcity and lower temperatures (e.g. seasonal growth): the extent of leaf water enrichment can thus be supposed to be on average lower in temperate regions than in the tropics.

The reason why the range of $\delta^{18}O_P$ at a given period is higher than expected (*i.e.* ~4 ‰ instead of ~2 ‰; figure 6-1, table 5-7 and table 6-2) could be explained by a different climatic pattern (*i.e.* more variable climate) during the Maya era compared to today. One must keep in mind that the "modern" climatic conditions at Flores were recorded between 1990 and 2006, so the range of climatic conditions during those 16 years is probably not representative of the climatic variability that occurs during longer periods (e.g. from 50 to 130 years, *i.e.* Kumche and Yaxche phases duration, respectively). In the end, the precision of Luz *et al.*'s equation is not questioned, but its accuracy could be greatly improved by re-calculating it using a set of bones coming from tropical regions.

6.4.1.2) Precipitation *versus* relative humidity

Both rain distribution and temperature variations through the year have an impact on resulting yearly average relative humidity and $\delta^{18}O_{Rain}$ (see also figure 1-7, Chapter 1). For example, at Flores, the yearly average humidity of 1994, the driest year between 1990 and 2006 (total precipitation of 1,160 mm), is almost equal to the yearly average relative humidity of the wettest year (2006, total precipitation of more than 2,395 mm; see table 6-2), but the yearly average $\delta^{18}O_{Rain}$ is significantly different (-3.4 *versus* -5.1 ‰). In this case, the amount effect can be considered as the main factor controlling yearly average $\delta^{18}O_{Rain}$. However, when 1997 and 1998 are compared, the total amounts of precipitation are close (only ~150 mm difference), but the difference in yearly average relative humidity is high (9 %), inducing a yearly average $\delta^{18}O_{Rain}$ difference of 0.7 ‰ between the two years.

Correlating those climatic patterns to their impacts on Maya populations would require an extensive study of their agricultural procedures, but it is realistic to consider that the occurrence of consecutive years with low precipitation amounts (like in 1994) and/or low relative humidity (1998), farming would be less successful than during strings of years with higher precipitation amounts (2006) and/or high relative humidity (1998). The number of consecutive "dry" years needed to impact durably the Maya people is uncertain, and depends on the strength, the duration and the spreading of dry episodes among a single year.

The advantage of using deer bone $\delta^{18}O_P$ to assess the impact of past climatic conditions on the Maya population comes from the distinction between climatic conditions that are believed to negatively impact the population (expected $\delta^{18}O_P$ of ~18 ‰), and those that are not (expected $\delta^{18}O_P$ of ~20 ‰), without distinguishing the contribution of low precipitation amounts from the contribution of low relative humidity (table 6-2). Deer bones are then considered to be useful aridity indicators in the context of the Maya collapse.

6.4.2) Interpreting $\delta^{13}C_{Bone}$ variations

Interpreting $\delta^{13}C_{Bone}$ variations is not easy, due to the possible mixed effects of C4 proportion in the diet, the density of forest coverage and the effect of water stress on $\delta^{13}C_{POM}$.

As stated in Chapter 3 (part 3.3.2), $\delta^{13}C_{Bone}$ is strictly dependant on the carbon isotopic composition of deer's diet. Deer subsists almost entirely on C3 plants, so in case of a diet only based on C3 plants, $\delta^{13}C_{Bone}$ of the analyzed deer bones would be ~ -13 ‰ (figure 3-6, Chapter 3). However, the proportion of C4 plants in its diet may increase in the case of starvation, likely to occur during more arid conditions, when C3 plants with sufficient humidity amounts would no longer be available (Chapter 3, part 3.3). As a consequence, high $\delta^{13}C_{Bone}$ (*i.e.* higher than -13 ‰) could be interpreted as reflecting drier conditions.

It has also been shown that during droughts, to prevent damageable water loss, the mechanisms of stomata closure among C3 plants reduces the discrimination against ^{13}C during CO_2 assimilation in the tissues, provoking a slight shift (~2 ‰) of $\delta^{13}C_{POM}$ towards higher values (improved water use efficiency; Chapter 3, part 3.3.2). So, as in the case of increased proportion of C4 plants in the diet, higher $\delta^{13}C_{Bone}$ values should be also interpreted as reflecting drier conditions.

However, Piedras Negras is in a zone of dense rainforest and was likely never deforested during its history (Beach *et al.*, 2006). Due to the *canopy effect* (Chapter 3, part 3.2.2), the plants ingested by the deer in the region surrounding Piedras Negras are expected to be relatively ^{13}C-depleted (low $\delta^{13}C_{POM}$).

In the end, it is likely that the effects of droughts on water use efficiency or C4 proportion in the diet were potentially overridden by the canopy effect. Yet, the relative broad range of $\delta^{13}C_{Bone}$ (from -13 to -8 ‰, except one value at -6 ‰: figure 6-2), indicates that (1) no *canopy effect* is apparent in our dataset, and (2) deer diets vary considerably among individuals.

In our dataset, no value is lower than -13 ‰, so there is no absolute evidence of *canopy effect*. The lack of *canopy effect* in our dataset is surprising, given that Piedras Negras remained continuously forested. A possible explanation might be the impact of prolonged dry conditions, possibly leading to a reduction of vegetation density in the rain forest that would have resulted in reduced *canopy effect*. This should be further investigated by analyses of modern deer bones from the same area, still densely forested today.

The factors influencing diet selection are numerous (season, reproductive stage, vegetation distribution, sex; Hervert & Krausman, 1986; Lautier *et al.*, 1988; Bello *et al.*, 2001). Relatively high $\delta^{13}C_{Bone}$ values have been attributed to maize (C4 plant) intake by semi-domesticated individuals feeding from agricultural fields at the forest edge, herds managed in the wild or enclosed captive being fed by humans (Emery *et al.*, 2000; White *et al.*, 2001). In the end, the vision of a stable C3 diet appears to be erroneous in the Maya context and raises questions about the use of $\delta^{13}C$ as a climate indicator.

The loss of climatic signal held by $\delta^{13}C_{Bone}$ dataset at PN is confirmed by figure 6-2, showing the absence of correlation between $\delta^{18}O_P$ and $\delta^{13}C_{Bone}$. Given that $\delta^{18}O_P$ values are considered to accurately reflect the yearly averages relative humidity and/or precipitation amounts, a linear correlation would have been expected with $\delta^{13}C_{Bone}$, if those values were reflecting the same variables.

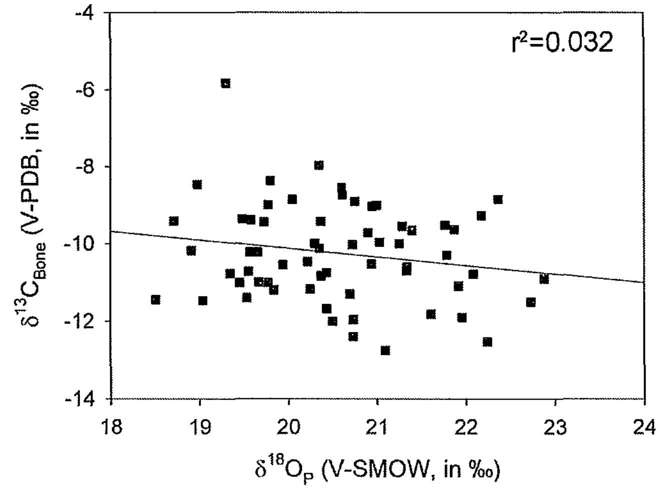

Figure 7. $\delta^{18}O_P$ against $\delta^{13}C_{Bone}$ among the dataset from Piedras Negras including Balche, Yaxche, Chacalhaaz and Kumche phases (n=62).

6.4.3) Climatic cause for the collapse at Piedras Negras ?

Archaeological evidence shows that Piedras Negras was a powerful and influent regional centre in the Maya Lowlands, continuously occupied from the Middle Pre-Classic (~500 BC) to the Terminal Classic (until ~AD 900; Muñoz, 2004). The end of the Chacalhaaz ceramic complex (AD 750 – 850) is defined by the introduction of foreign ceramic styles in the archaeological record, marking the end of the regional influence of Piedras Negras (Houston *et al.*, 2003). A recent population estimate of Piedras Negras based on household size and quantity highlighted a gradual abandonment of the site at around AD 850, leading to a dramatic decrease in population between the Chacalhaaz and Kumche ceramic phases (figure 6-3; Nelson, 2005). Further investigations have shown that the population started to decrease at around AD 810, at a time the ruler of the site has been captured, implying deep socio-political changes at Piedras Negras, but other sites located near PN remained inhabited for decades after the royal court imploded (Golden & Scherer, pers. com.).

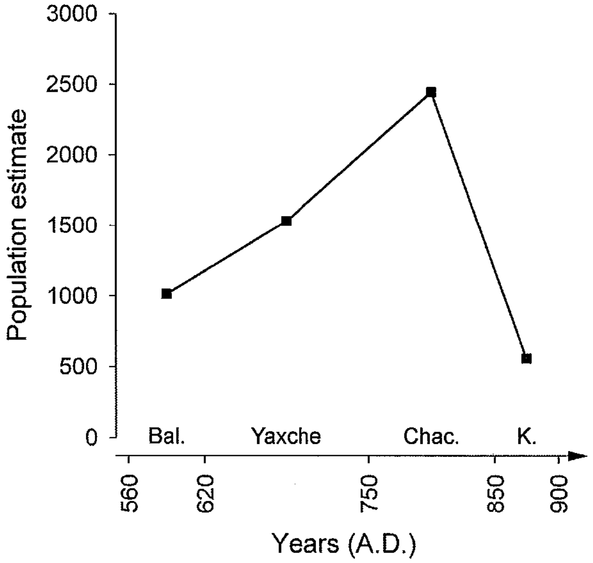

Figure 8. Population estimates at Piedras Negras (centre core) during Balche, Yaxche, Chacalhaaz and Kumche cultural periods (Nelson, 2005).

From $\delta^{18}O_P$ analyses (figure 6-1), it is believed that "average" climatic conditions were relatively drier during Balche phase (AD 560-620) compared to Yaxche and Chacalhaaz phases (AD 620-850). The minimum and maximum $\delta^{18}O_P$ values during this phase, representing the extreme climatic events, are both higher than during Yaxche and Chacalhaaz phases. In particular, wet periods during Balche were probably less intense (in terms of yearly averages precipitation amounts and/or relative humidity) than during the next two phases (minimum $\delta^{18}O_P$ during Balche is ~1 ‰ lower than the minimum $\delta^{18}O_P$ during Yaxche and Chacalhaaz phases). Dry periods seemed to have been slightly more intense (lower precipitation amounts and/or relative humidity) than during the next two phases (maximum $\delta^{18}O_P$ during Balche is ~0.5 ‰ higher than maximum $\delta^{18}O_P$ during Yaxche and Chacalhaaz phases).

No significant climate change seemed to have occurred between Yaxche and Chacalhaaz phases. The average $\delta^{18}O_P$ is slightly lower during Chacalhaaz phase, possibly indicating climatic conditions on average slightly wetter than during Yaxche phase. The broader range of $\delta^{18}O_P$ values during Chacalhaaz phase (~3.9 against 3.5 ‰) indicates that more "extreme" events (wet and dry) were likely to have occurred compared to during Yaxche phase. It is suggested that the relative stability of the climatic conditions between AD 620 and AD 850 could partly be responsible of the flourishing of Piedras Negras during that time.

Unfortunately, conclusion about climatic conditions during the Kumche phase are less well supported by the poor representativeness of the dataset (3 bones were analyzed only). However, the maximum $\delta^{18}O_P$ value during the Kumche phase is comparable to the maximum one during Balche. It is thus likely that during the 50 years of the Kumche phase, an episode of drought took place, long enough to be detectable by the poor temporal resolution of the dataset. So it is likely that the drought detected the Kumche phase was probably worsening factor that hastened the fall of a city already fading due to internal socio-political causes.

Surprisingly, the absence of significant droughts during the Yaxche and Chacalhaaz phases is in contradiction with other findings such as, for example, the first phase of Terminal Classic Drought (AD 770-870) detected by Hodell *et al.* (2005) based on core analysis from lake Chichancanab (Mexico), or the intense 9 years–long drought centered on ~810 AD, inferred from low titanium content in Cariaco basin sediments (Haug *et al.*, 2003; Chapter 1, part 1.5.2).

Studies based on sediments analyses have a low spatial resolution. This is especially the case for Haug *et al.* (2003) study, where inferences are made from the Cariaco basin, considered as meteorologically similar to Yucatán peninsula (Chapter 1). The sedentary lifestyle of deer makes it a very local recorder of past conditions, so it is suggested that the contradiction between our results and the findings of both Haug *et al.* (2003) and Hodell *et al.* (2005) could possibly be explained by the uniqueness of Yucatán's climatology (Chapter 1), as well as the restricted spatial resolution of our method (part 6.3.3 above).

The signal held by $\delta^{13}C_{Bone}$ is more difficult to decipher, but it can be observed that the range and average $\delta^{13}C_{Bone}$ remained quite stable between the Balche and Chacalhaaz phases, but a "jump" towards higher values is observed during the terminal phase. In particular, the maximum $\delta^{13}C_{Bone}$ during the Kumche phase (~-5.8 ‰) is significantly higher (by about 2 ‰) that the rest of the dataset. Given that this high value is probably due to an unusually large proportion of C4 plants in deer diet, it is thus suggested that the bone exhibiting this high $\delta^{13}C_{Bone}$ is coming from a deer feeding on a large proportion of maize. This could be considered as an evidence of deer pseudo-domestication at Piedras Negras during the Terminal Classic.

References

Ayliffe L.K., A.R. Chivas, M.G. Leakey (1994) - The retention of primary oxygen isotope compositions of fossil elephant skeletal phosphate. *Geochimica et Cosmochimica Acta* 58, 5291–5298.

Baig A.A., J.L. Fox, R.A. Young, Z. Wang, J. Hsu, W.I. Higuchi, A. Chhettry, H. Zhuang, M. Otsuka (1999) - Relationships among carbonated apatite solubility, crystallite size, and microstrain parameters. *Calcified Tissue International* 64, 437– 449.

Balasse M., S.H. Ambrose, A.B. Smith, T.D. Price (2002) - The seasonal mobility model for prehistoric herders in the south-western Cape of South Africa assessed by isotopic analysis of sheep tooth enamel. *Journal of Archaeological Science* 29, 917–932.

Bassett D., K.G. MacLeod, J.F. Miller, R.L. Ethington (2007) – Oxygen isotopic composition of biogenic phosphate and the temperature of early Ordovician seawater. *Palaios* 22,98-103.

Baxter B.J., R.N. Andrews, G.K. Barrell (1999) – Bone turnover associated with antler growth in red deer (Cervus elaphus). *The Anatomical Record* 256, 14-19.

Beach, T., N. Dunning, S. Luzzadder-Beach, D.E. Cook, J. Lohse (2006) - Impacts of the ancient Maya on soils and soil erosion in the central Maya Lowlands. *Catena* 65, (2):166-178.

Bell L.S., G. Cox, J. Sealy (2001) - Determining isotopic life history trajectories using bone density fractionation and stable isotope measurements: a new approach. *American Journal of Physical Anthropology* 116, 66–79.

Bello J., S. Gallina, M. Equihua (2001) - Characterization and Habitat Preferences by White-Tailed Deer in Mexico. *Journal of Range Management* 54, (5):537-545.

Berna F., A. Matthews, S. Weiner (2004) - Solubilities of bone mineral from archaeological sites: the recrystallization window. *Journal of Archaeological Science* 31, (7): 867-882.

Blake R.E., J.R. O'Neil, G.A. Garcia (1997) - Oxygen isotope systematics of biologically mediated reactions of phosphate: I. Microbial degradation of organophosphorus compounds. *Geochimica et Cosmochimica Acta 61*, 4411–4422.

Bocherens H., M. Fizet, A. Mariotti (1994) - Diet, physiology and ecology of fossil mammals as inferred from stable carbon and nitrogen isotope biogeochemistry: implications for Pleistocene bears. *Palaeogeography, Palaeoclimatology, Palaeoecology* 107, 213–225.

Botha J., J. Lee-Thorp, M. Sponheimer (2004) - An examination of Triassic cynodont tooth enamel chemistry using Fourier Transform Infrared spectroscopy. *Calcified Tissue International* 74, (2): 162-169.

Brand W.A., T.B. Coplen, A.T. Aerts-Bijma *et al.* (2009) – Comprehensive inter-laboratory calibration of reference materials for $\delta^{18}O$ versus VSMOW using various on-line high-temperature conversion techniques. *Rapid Communications in Mass Spectrometry* 23, 999–1019.

Brunjes K.J., W.B. Ballard, M.H. Humphrey, F. Harwell, N.E. McIntyre, P.R. Krausman, M.C. Wallace (2006) – Habitat use by sympatric mule and white-tailed deer in Texas. *The Journal of Wildlife Management* 70, (5): 1351-1359.

Bryant J.D., P. Koch, P.N. Froelich, W.J. Showers, B.J. Genna (1996) – Oxygen isotope partitioning between phosphate and carbonate in mammalian apatite. *Geochimica et Cosmochimica Acta* 60, 5145-5148.

Crowson R.A., W.J. Showers, E.K. Wright, T.C. Hoering (1991) – Preparation of phosphate samples for oxygen isotope analysis. *Analytical Chemistry* 63, 2397-2400.

Darr R.L. & D.G. Hewitt (2008) – Stable isotope trophic shifts in white-tailed deer. *The Journal of Wildlife Management* 72, (7):1525-1531.

Delgiudice G. D., M. S. Lenarz, M. C. Powell (2007) - Age-specific fertility and fecundity in northern free-ranging white-tailed deer: Evidence for reproductive senescence? *Journal of Mammalogy* 88, (2):427 435.

De Mul F.F.M., M.H.J. Hottenhuis, P. Bouter, J. Greve, J. Arends, J.J. Ten Bosch (1986) - Micro-Raman line broadening in synthetic carbonated hydroxyapatite. *Journal of Dental Research* 65, 437– 440.

DeNiro M.J. & S. Weiner (1988) - Organic matter within crystalline aggregates of hydroxyapatite: a new substrate for stable isotopic and possibly other biogeochemical analyses of bone. *Geochimica et Cosmochimica Acta* 52, 2415–2423.

Dettman D.L., M.J. Kohn, J. Quade, F.J. Ryerson, T.P. Ojha, S. Hamidullah (2001) - Seasonal stable isotope evidence for a strong Asian monsoon throughout the past 10.7 m.y. *Geology* 29, 31-34.

Elliott J. C. (2002) - Calcium posphate biominerals. Phosphates - Geochemical, Geobiological, And Materials Importance. M. J. Kohn, J. Rakovan and J. M. Hughes. Washington DC, Mineral Society of America. **48:** 427-453.

Emery K.F., L.E. Wright, H.P. Schwarcz (2000) – Isotopic analysis of ancient deer bone: biotic stability in collapse period Maya land-use. *Journal of Archaeological Science* 27, 537-550.

Epstein S., R. Buchsbaum, H.A. Lowenstam, H.C. Urey (1953) - Revised carbonate-water isotopic temperature scale.*Geological Society of America Bulletin* 64,1315-1326.

Fernández F.G., K .D. Johnson, R.E. Terry, S. Nelson, D. Webster (2005) - Soil Resources of the Ancient Maya at Piedras Negras, Guatemala. Soil Science Society of America Journal 69, 2020–2032.

Foias A.E. (2003) - Politics and Economics: Motul de San José, Petén. *Foundation for the Advancement of Mesoamerican Studies, Inc.* Accessed online <www.famsi.org>, June 2008.

Fratzl P., H. S. Gupta, E. P. Paschalis, P. Roschger (2004) - Structure and mechanical quality of the collagen-mineral nano-composite in bone. *Journal of Materials Chemistry* 14, (14): 2115-2123.

Fricke H.C., W.C. Clyde, J.R. O'Neil, P.D. Gingerich (1998) - Evidence for rapid climate change in North America during the latest Paleocene thermal maximum: oxygen isotope compositions of biogenic phosphate from the Bighorn Basin (Wyoming).*Earth and Planetary Science Letters* 160, 193–208.

Friedman I. & J.R. O'Neil (1977) - Compilation of stable isotope fractionation factors of geochemical interest. In

Data of Geochemistry (6th Edition). Fleischer, M. (Ed.), Government Printing Office, Washington, D.C.

Garvie-Lok S.J., T.L. Varney, M.A. Katzenberg (2004) - Preparation of bone carbonate for stable isotope analysis: the effects of treatment time and acid concentration. *Journal of Archaeological Science* 31, 763–776.

Glimcher M.J. (2006) - Bone: nature of the calcium phosphate crystals and cellular, structural, and physical chemical mechanisms in their formation. *Reviews in Mineralogy & Geochemistry* 64, 223-282.

Harris E.C. (1979) – Principles of Archaeological Stratigraphy. Academic press. London.

Haug G.H., D. Günther, L.C. Peterson, D.M. Sigman, K.A. Hughen, B. Aeschliman (2003) - Climate and the collapse of Maya civilization. *Science* 299, 1731-1735.

Hedges R.E.M. (2002) - Bone diagenesis: An overview of processes. *Archaeometry* 44, 319-328.

Hervert J.J. & P.R. Krausman (1986) - Desert Mule Deer Use of Water Developments in Arizona. *The Journal of Wildlife Management* 50, (4):670-676.

Hillman J.R., R.W. Davis, Y.Z. Abdelbaki (1973) – Cyclic bone remodelling in deer. *Calcified Tissue Research* 12, 323-330.

Hodell D.A., M. Brenner, J.H. Curtis (2007) - Climate and cultural history of the Northeastern Yucatán Peninsula, Quintana Roo, Mexico. *Climatic Change* 83, 215-240.

Houston S.D., H. Escobedo, M. Child, C.W. Golden, A.R. Muñoz (2001) - Moral community and settlement transformation among the Classic Maya: Evidence from Piedras Negras, Guatemala. In Social Construction of Ancient Cities, Smith M.L. (ed.). Smithsonian Institution Press, Washington, DC.

Iacumin P., H. Bocherens, A. Mariotti, A. Longinelli (1996) - Oxygen isotope analyses of co-existing carbonate and phosphate in biogenic apatite: a way to monitor diagenetic alteration of bone phosphate? *Earth and Planetary Science Letters* 142, 1-6.

INSIVUMEH (2009) – Instituto Nacional de Sismologia, Vulcanologia, Meteorolgia e Hidrologia (Guatemala). *Estadísticas Climáticas*. Accessed online <http://www.insivumeh.gob.gt>, August 2008.

Koch P.L., N. Tuross, M.L. Fogel (1997) - The effects of sample treatment and diagenesis on the isotopic integrity of carbonate in biogenic hydroxylapatite. *Journal of Archaeological Science* 24, 417–429.

Kohn M.J. (1996) – Predicting animal $\delta^{18}O$: accounting for diet and physiological adaptation. *Geochimica et Cosmochimica Acta 60*, 4811-4829.

Kohn M.J., M.J. Schoeninger, W.W. Barker (1999) – Altered states: Effects of diagenesis on fossil tooth chemistry. *Geochimica et Cosmochimica Acta* 63, (18):2737-2747.

Kolodny Y. & B. Luz (1991) - Oxygen isotopes in phosphates of fossil fish: Devonian to recent. In Stable Isotope Geochemistry: A Tribute to Samuel Epstein. H.P. Taylor, J.R. O'Neil, & I.R. Kaplan, (Eds.). Special Publication No. 3, The Geochemical Society.

Krueger H.W. (1991) - Exchange of carbon with biological apatite. *Journal of Archaeological Science* 18, 355–361.

Lautier J.K., T.V. Dailey, R.D. Brown (1988) - Effect of Water Restriction on Feed Intake of White-Tailed Deer. *The Journal of Wildlife Management* 52, (4):602-606.

Lee-Thorp J.A. (1989) - Stable carbon isotopes in deep time: diet of fossil fauna and hominids. PhD Thesis. University of Cape Town, Cape Town.

Lee-Thorp J.A. & N.J. van der Merwe (1991) - Aspects of the chemistry of modern and fossil biological apatites. *Journal of Archaeological Science* 18, 343–354.

Lee-Thorp J.A., L. Manning, M. Sponheimer (1997) - Problems of and prospects for carbon isotope analysis of very small samples of tooth enamel. *Bulletin de la Société Géologique de France* 168, 767–773.

Longinelli A. (1984) - Oxygen isotopes in mammal bone phosphate: a new tool for paleohydrological and paleoclimatological research? *Geochimica et Cosmochimica Acta* 48, 385-390.

Longinelli A. (1996) - Pre-Quaternary isotope palaeoclimatological and palaeoenvironmental studies: science or artifact? *Chemical Geology* 129, 163-166.

Luz B., A.B. Cormie, H.P. Schwarcz (1990) - Oxygen isotope variations in phosphate of deer bones. *Geochimica et Cosmochimica Acta* 54, 1723-1728.

Metcalfe J., F.J. Longstaffe, C.D. White (2009) - Method-dependent variations in stable isotope results for structural carbonate in bone bioapatite. *Journal of Archaeological Science* 36, 110–121

Muñoz A.R. (2004) – The Ceramic Sequence of Piedras Negras, Guatemala: type and varieties. *Foundation for the Advancement of Mesoamerican Studies, Inc.* Accessed online <www.famsi.org>, June 2008.

Munro L.E., F.J. Longstaffe, C.D. White (2007) - Burning and boiling of modern deer bone: Effects on crystallinity and oxygen isotope composition of bioapatite phosphate. *Palaeogeography, Palaeoclimatology, Palaeoecology* 249, 90-102.

Munro L.E., F.J. Longstaffe, C.D. White (2008) - Effects of heating on the carbon and oxygen-isotope compositions of structural carbonate in bioapatite from modern deer bone. *Palaeogeography, Palaeoclimatology, Palaeoecology* 266, 142-150.

Nelson Z.N. (2005) – Settlement and population at Piedras Negras, Guatemala. *PhD thesis.* Pennsylvania State University, Philadelphia.

Nielsen-Marsh C.M. & R.E.M. Hedges (1997) - Dissolution experiments on modern and diagenetically altered bone and the effect on the infrared splitting factor. *Bulletin de la Société Geologique de France* 168, 485–490.

Nielsen-Marsh C. M. & R.E.M. Hedges (2000a) - Patterns of diagenesis in bone, I: the effects of site environments. *Journal of Archaeological Science* 27, 1139–1150.

Nielsen-Marsh C.M. & R.E.M. Hedges (2000b) - Patterns of diagenesis in bone, II: Effects of acetic acid treatment and the removal of diagenetic CO_3^{2-}. *Journal of Archaeological Science* 27, 1151–1159.

O'Neil J.R., L.J. Joe, E. Reinhard, R.E. Blake (1994) – A rapid and precise method of oxygen isotope analysis of biogenic phosphate. *Israel Journal of Earth Sciences* 43, 203-212.

Penel G., G. Leroy, C. Rey, E. Bres (1998) - MicroRaman spectral study of the PO4 and CO3 vibrational modes in synthetic and biological apatites. *Calcified Tissue International* 63, 475–481.

Pucéat E., B. Reynard, C. Lécuyer (2004) - Can crystallinity be used to determine the degree of chemical alteration of biogenic apatites? *Chemical Geology* 205, 83- 97.

Rey, C., A. Hina, A. Tofighi and M. J. Glimcher (1995) - Maturation of poorly crystalline apatites: Chemical and structural aspects in vivo and in vitro. *Cells and Materials* 5, (4): 345-356.

Saliège J.-F., A. Person, F. Paris (1995) - Preservation of $^{13}C/^{12}C$ original ratio and ^{14}C dating of the mineral fraction of human bones from Saharan tombs, Niger. *Journal of Archaeological Science* 22, 301–302.

Shahack-Gross R., E. Tchernov, B. Luz (1999) - Oxygen Isotopic Composition of Mammalian Skeletal Phosphate from the Natufian Period, Hayonim Cave, Israel: Diagenesis and Paleoclimate. *Geoarchaeology: An International Journal* 14, (1): 1–13.

Shemesh A. (1990) - Crystallinity and diagenesis of sedimentary apatites. *Geochimica Et Cosmochimica Acta* 54, (9): 2433-2438.

Smith W.P. (1991) – Odocoileus virginianus. *Mammalian Species* 388, 1-13.

Sponheimer M. & J.A. Lee-Thorp (1999) - Alteration of enamel carbonate environments during fossilization. *Journal of Archaeological Science* 26, (2): 143-150.

Stephan E. (2000) - Oxygen isotope analysis of animal bone phosphate: method refinement, influence of consolidants, and reconstruction of palaeotemperatures for Holocene sites. *Journal of Archaeological Science* 27, 523-535.

Stuart-Williams H. Le Q., H.P. Schwarcz, C.D. White, M.W. Spence (1996) - The isotopic composition and diagenesis of human bone from Teotihuacan and Oaxaca, Mexico. *Palaeogeography, Palaeoclimatology, Paleoecology* 126, 1–14.

Sullivan C.H. & H.W. Krueger (1981) – Carbon isotope analysis of separate chemical phases in modern and fossil bone. *Nature* 292, 333-335.

Surovell T.A. & M.C. Stiner (2001) - Standardizing infra-red measures of bone mineral crystallinity: An experimental approach. *Journal of Archaeological Science* 28, (6): 633-642.

Trueman C.N., K. Privat, J. Field (2008) - Why do crystallinity values fail to predict the extent of diagenetic alteration of bone mineral? *Palaeogeography Palaeoclimatology Palaeoecology* 266, (3-4): 160-167.

Turner-Walker G. & U. Syversen (2002) - Quantifying histological changes in archaeological bones using BSE-SEM image analysis. *Archaeometry* 44, 461–468.

Vennemann T.W., H.C. Fricke, R.E. Blake, J.R. O'Neil, A. Colman (2002) - Oxygen isotope analysis of phosphates: a comparison of techniques for analysis of Ag_3PO_4. *Chemical Geology* 185, 321– 336.

Wang Y. & T.E. Cerling (1994) - A model of fossil tooth and bone diagenesis: implications for paleodiet reconstruction from stable isotopes. *Palaeogeography, Palaeoclimatology, Palaeoecology* 107, 281–289.

Webb E.A., H.P. Schwarcz, C.T. Jensen, R.E. Terry, M. Moriarty, K. Emery (2007) - Stable Carbon Isotope Signature of Ancient Maize Agriculture in the Soils of Motul de San José, Guatemala..*Geoarchaeology* 22, (3): 291–312.

Weiner S. & P. Price (1986) - Disaggregation of bone into crystals. *Calcified Tissue International* 39, 365–375.

Weiner S. & O. Bar-Yosef (1990) - States of preservation of bones from prehistoric sites in the Near East: a survey. *Journal of Archaeological Science* 17, 187-196.

White C.D., M.E.D. Pohl, H.P. Schwarcz, F.J. Longstaffe (2001) - Isotopic evidence for Maya patterns of deer and dog use at Preclassic Colha. *Journal of Archaeological Science* 28, 89–107.

Wiedemann-Bidlack F.B., A.S. Colman, M.L. Fogel (2008) - Phosphate oxygen isotope analysis on microsamples of bioapatite: removal of organic contamination and minimization of sample size. *Rapid Communication in Mass Spectrometry* 22, 1807–1816.

Wierzbowski H. (2007) - Effects of pre-treatments and organic matter on oxygen and carbon isotope analyses of skeletal and inorganic calcium carbonate. *International Journal of Mass Spectrometry* 268, 16–29.

Wopenka B. & J.D. Pasteris (2005) - A mineralogical perspective on the apatite in bone. *Materials Science & Engineering C-Biomimetic and Supramolecular Systems* 25, (2): 131-143.

Wright L.E. & H.P. Schwarcz (1996) - Infrared and isotopic evidence for diagenesis of bone apatite at Dos Pilas, Guatemala: palaeodietary implications. *Journal of Archaeological Science* 23, 933-944.

Wright L.E. & H.P. Schwarcz (1998) - Stable carbon and oxygen isotopes in human tooth enamel: identifying breastfeeding and weaning in prehistory. *American Journal of Physical Anthropology* 106, 1–18.

Zazzo A., C. Lécuyer, A. Mariotti (2004) - Experimentally-controlled carbon and oxygen isotope exchange between bioapatites and water under inorganic and microbiallymediated conditions. *Geochimica et Cosmochimica Acta* 68, 1–12.

Final conclusion

It has been shown that recurrent episodes of severe and prolonged droughts did occur in Central America at the time the Maya population started to drop dramatically, making the central role of climate change in the Terminal Classic Maya collapse becoming less and less questionable. However, due to the complexity of (1) the climatic context in the Maya region, ranging within a few hundreds of kilometres from the extremely wet dense rain forest of central Petén to the semi-arid plains of northern Yucatán, and (2) the wave-like pattern of the collapse, affecting some sites while others flourished, a proxy to track the evolution of climate at a very local scale to test the simultaneity of site abandonment and droughts was strongly needed.

The different results obtained during this study shown that deer bone is truly a good material to fulfil this role: geochemical analyses of deer bones actually give reliable results, in accordance with predicted values. Hence, it is believed that deer bone can be trusted as a valuable climatic recorder to track changes of precipitation amounts and relative humidity ($\delta^{18}O$) during the Maya era.

Still, care must be taken during sample processing. First, each chemical pre-treatment is likely to induce a slight modification of the isotopic composition of deer bone mineral, and it has been shown the critical step affecting the accuracy of isotopic measurements may be the removal of organic matter prior to analyses. Secondly, the detection of possible diaganetic alteration of bone is also crucial. During this study, it has been shown that the use of Fourier-Transform Infra Red spectroscopy is not as reliable as previously thought. Secondary re-crystallized minerals such as calcite are detected with confidence, but the exact nature of carbonate substitution in the bioapatite crystal lattice is still not well understood, preventing a meaningful interpretation of the spectra. In the end, it is considered that the best way to assess bone diagenetic alteration is the comparison between $\delta^{18}O_P$ and $\delta^{18}O_C$ because *in vivo*, those two values are in linear equilibrium. Lastly, the diagenetic context of the Maya region (high temperatures and variable soil hydrology) may also alter the isotopic composition of archaeological remains, inducing unexpected low precision of isotopic measurements.

However, the most important factor limiting the interpretation of the results is the time resolution of the material. Firstly, as it is considered that deer bone is averaging roughly 2 to 3 years of local climatic conditions, a duration corresponding to mineral remodelling processes occurring throughout deer's life, only long-term climatic fluctuations (*i.e.* pluri-annual) are detectable. The broad range of $\delta^{18}O_P$ values measured on deer bones from Piedras Negras during each cultural phase shows that strings of years with either wet or dry conditions did occur, and that the climatic conditions during them were more intense than during the wettest and especially the driest years observed in the region for the past 20 years. The climate over the region surrounding Piedras Negras was then probably more variable than today. Secondly, the number of bones available and most importantly the precision with which they are dated both affect the meaning of the results. Even if the exceptional archaeological context in the Maya region allows a good time resolution, the time covered by each cultural phase (from 50 to 130 years in the case of Piedras Negras), in addition to the high variability of Central American climate at a decadal scale, both make the signification of "average" climatic conditions during each cultural phase poorly meaningful. In the end, climatic extremes should be considered as more accurate to describe past climate fluctuations in the Maya region, if the number of bones analyzed is sufficient to have an acceptable "sampling density" among each cultural phase.

During this study, it has not been possible to highlight any particularly intense and/or prolonged period of dry climatic conditions at Piedras Negras before and during the time the city started to be abandoned. One must keep in mind that the site is located in one of the wettest zone of the Maya region, and that the beginning of the collapse process took place at a time of the city faced major socio-political changes. This highlights the need of a precise understanding of each site history to correlate the impacts of climate change to the decline of studied sites. Subsequently, it can be considered that droughts were probably not the cause of the decline at Piedras Negras. However, the dataset indicates the occurrence of a period of marked dry conditions during the final (post-collapse) cultural phase, so that it is likely that the consecutive water shortage would have been a worsening factor that hastened the fall of the city already into a collapse process.

As for future research, the strength of the interpretations could be greatly improved in several ways. Due the level of variance observed in the deer bone samples datasets, increasing the sample size would make statistical inference more reliable, leading to a more accurate understanding of the past climatic variability. Then, it would be interesting to build up a database of isotopic data measured on (1) modern wild deer bones with known date of death and (2) leaf water samples, both coming from the different climatic sub-zones of the Maya region, to correlate the obtained results to the climatic databases available, and to establish a precise expected range of variation of those values. Bone oxygen isotopic composition of modern yucatecan herbivores that satisfy their water need with meteoric water would also help to better assess the contribution of isotopically enriched leaf water to the oxygen isotopic ratios measured in deer bones.

In the end, more than bringing categorical answers on the effects of climate change on the decline of the Maya, this work should be considered as a handbook for future studies of oxygen and carbon isotopic compositions of deer bones in tropical environments with marked dry/wet seasonality.

List of abbreviations

API	A-type carbonate to Phosphate ratio Index
Asl	Above sea level
BAI	Relative amount of B- to A-type substitution Index
BPI	Relative amount of B-type carbonate to Phosphate Index
CAN	Comisión Nacional de Agua (Mexican water ressources commission)
CI	Crystallinity Index
DDI	Double De-Ionized
DIC	Dissolved Inorganic Carbon
$\delta^{13}C_{Bone}$	Carbon isotopic composition of deer bone bioapatite
$\delta^{13}C_{POM}$	Carbon isotopic composition of plant organic matter
$\delta^{18}O_{C}$	Oxygen isotopic composition deer bone bioapatite (carbonate)
$\delta^{18}O_{LW}$	Oxygen isotopic composition of leaf water
$\delta^{18}O_{P}$	Oxygen isotopic composition deer bone bioapatite (phosphate)
$\delta^{18}O_{Rain}$	Oxygen isotopic composition of precipitation
$\delta^{18}O_{SW}$	Oxygen isotopic composition of the soil water
ENSO	El-Niño Southern Oscillation
FTIR	Fourier-Transform Infra-Red
GC-IRMS	Gas Chromatograph-Isotope Ratio Mass Spectrometer
GNIP	Global Network of Isotopes in Precipitation
IAEA	International Atomic Energy Agency
INSIVUMEH	Instituto Nacional de Sismologia, Vulcanologia, Meteorolgia e Hidrologia (Guatemalan weather and environment bureau)
ITCZ	Inter-Tropical Convergence Zone
LAM	Lamanai
MSD	Mid-Summer Drought
MSJ	Motul de San José
PC	Percent Crystallinity
PDI	Palmer Drought Index
PN	Piedras Negras

r^2	Linear correlation coefficient
ρ_{SAT}	Saturation vapour pressure
SEM	Scanning Electron Microscopy
SF	Splitting Factor
SMOW	Standard Mean Ocean Water
SPI	Standardized Precipitation Index
SSS	Sea Surface Salinity
SST	Sea Surface Temperature
σ	Standard deviation
TC/EA	Temperature Conversion/Elemental Analyzer
TCC	Total Carbonate Content
TEM	Transmission Electron Microscopy
USGS	United States Geological Survey
V-PDB	Vienna-Pee Dee Belemnite
V-SMOW	Vienna-Standard Mean Ocean Water
WMO	World Meteorological Organization